

The Low Frequency Frontier: Cosmology with Future 21cm Experiments

Thesis by
Abhilash Mishra

In Partial Fulfillment of the Requirements for the
degree of
Doctor of Philosophy

The logo for the California Institute of Technology (Caltech), featuring the word "Caltech" in a bold, orange, sans-serif font.

CALIFORNIA INSTITUTE OF TECHNOLOGY
Pasadena, California

2018
Defended July 21, 2017

© 2018

Abhilash Mishra

ORCID: 0000-0002-4424-4096

All rights reserved

For Bapa, Ma, and Mamuni

"[The Emperor Kublai Khan] said: "It is all useless, if the last landing place can only be the infernal city, and it is there that, in ever-narrowing circles, the current is drawing us."

To which Marco Polo replied: "The inferno of the living is not something that will be; if there is one, it is what is already here, the inferno where we live every day, that we form by being together. There are two ways to escape suffering it. The first is easy for many: accept the inferno and become such a part of it that you can no longer see it. The second is risky and demands constant vigilance and apprehension; seek and learn to recognize who and what, in the midst of the inferno, are not inferno, then make them endure, give them space."

-Italo Calvino, Invisible Cities

"It might seem limited to impose our human perception to try to deduce the grandest cosmic code. But we are the product of the universe and I think it can be argued that the entire cosmic code is imprinted in us. Just as our genes carry the memory of our biological ancestors, our logic carries the memory of our cosmological ancestry. We are not just imposing human-centric notions on a cosmos independent of us. We are progeny of the cosmos and our ability to understand it is an inheritance."

-Janna Levin, How the Universe Got Its Spots

ACKNOWLEDGEMENTS

The opportunity to participate in the scientific enterprise is a great privilege and I would not have embarked on this journey without the early encouragement and support from my teachers and mentors. Rinku Sarangi got me hooked on science in high school; she remains the best teacher I've met. Swadhin Pattanayak introduced me to the joys of research; his love for science and commitment to social justice continues to inspire me. Raka Dabhade, Ajit Kembhavi, Rajaram Nityananda, T Padmanabhan, and Subir Sarkar converted me to astrophysics; I'm grateful to them for helping me get here.

This thesis would not have been possible without the support from my advisor Chris Hirata. Chris' brilliance is matched only by his humility and generosity. He gave me the space to make my own mistakes, nudged me towards working on important problems, and was incredibly patient with me. His ability to bring forth the essential physics of a problem and his attention to detail is awe inspiring. I'm immensely grateful to him for supporting me through these years. My co-advisor Olivier Doré was kind to adopt me into his group. He has fostered a lively and diverse group of young cosmologists at Caltech and JPL and I learned a lot of astrophysics through the weekly journal clubs and group meetings he organized. His insight, advice, and sense of humor has kept me going during tough times and I thank him for his support. I'd also like to thank other members of my thesis committee: Lynne Hillenbrand, Shri Kulkarni, and Gregg Hallinan for their time and advice.

My work during grad school would not have been possible without my collaborators Michael Eastwood, Roland de Putter, Barnaby Rowe, Eric Linder, and Vera Gluscevic. I thank them for their dedication and for sharing their time and expertise with me. The Cahill cosmology and theoretical astrophysics community played an important role in teaching me about interesting astrophysical problems during the formative years of grad school. I thank Samaya Nissanke, Francis-Yan Cyr-Racine, Duncan Hanson, Alvise Raccanelli, Phil Bull, Jérôme Gleyzes, Andrew Benson, and Heidi Wu for sharing their ideas and insights.

The time I've spent at Caltech has been perhaps the happiest in my life, thanks in a large part to the community that the institute fosters. I thank my second family in Pasadena: Shriharsh, Kartiki, and Swarnima for taking care of me and cheering me up during tough times. They truly made Pasadena feel like home and I will

always cherish the times we spent together. I thank Aaron Zimmerman for being an amazing friend and mentor. Aaron is a role model to me in many ways and I learned a lot about astrophysics and life over coffee at Red Door. My academic siblings, Antonija Oklopčić, Tejaswi Venumadhav, Elisabeth Krause, and Denise Schmitz always looked out for me and were generous with their time and support. Working on homework sets during the first two years of grad school was a lot of fun because of John Wendell and Kristen Boydston. I thank them for converting me to Python and educating me about American pop culture. Alicia Lanz and Allison Strom were thoughtful, inspiring leaders in the Caltech student community during a particularly difficult time for the Institute. I'm very lucky to call them friends. My fellow grad students in Cahill, Mislav Baloković, Trevor David, Ben Montet, Matt Orr, Gina Duggan, Donal O'Sullivan, Jacob Jencson, Melodie Kao, Sebastian Pineda, Sherwood Andrew Richers, Elena Murchikova, Jackie Villadsen, Marin Anderson, Becky Jensen-Clem, and Bhawna Motwani made Cahill a warm and welcoming place to work. "The Elders": Mansi Kasliwal, Varun Bhalerao, Gwen Rudie, Drew Newmann, Laura Perez, and Matthew Stevenson worked really hard to build a supportive, tight-knit grad student body in astrophysics, and shaped Cahill to be a warm, collegial place for doing astrophysics. Thanks also to Anu Mahabal, Patrick Shopbell, Joy Painter, JoAnn Boyd, Gita Patel, Shirley Hampton, and everyone at the Caltech Dean's office for their helpfulness and generosity.

Grad school can be rather isolating but I'm thankful for the friends around the world who cheered me on along the way. Many thanks to Chris Sheppard and Rakesh Sharma for reminding me that there is a life outside of work. Io Kleiser and Matt Gethers for the laughter and the countless expeditions to WeHo. Mike Bottom and Heather Duckworth for the sparkling conversations, the bad movie nights and cake. Judith and Steve Marosvolgyi for their kindness. Sara Hubbard, Lee Thiesen, George Olive, and Ziyaad Bhorat for their friendship and for introducing me to the many delights of Los Angeles. Krishna Shankar and Ashish Goel for being the best house-mates one could ask for.

During my Ph.D. I was lucky to work for Science for All, an organization with a mission to ensure that everyone has the opportunity to participate in the scientific enterprise. I thank Priya Kakkar, Payal Goghare, and Rahul Panda and the other team members at SfA for all they have done to keep the program running while I was writing this thesis. My work with Science for All kept me grounded and reminded me that everyone should have an opportunity to understand the way our universe

works, no matter where they live. I'm very excited to continue this work during the next stage of my career.

My friends Indra and Pinkesh, have taught me so much over the years. Their friendship means the world to me and nothing I write here can do justice to what I owe them.

One of the most difficult events over the past few years was the passing of my friend Ishita Maity. Her passing left a void that will never be filled. I miss her.

Thanks most of all, to my family: my parents and my sister. They have always supported and encouraged my somewhat esoteric pursuits. Without their unconditional love and sacrifice none of this would have been possible.

ABSTRACT

This thesis presents theoretical and observational investigations in two areas of cosmology: the detection of inflationary gravitational waves using the circular polarization of the redshifted 21cm line from neutral hydrogen during the Dark Ages, and the study of galactic foregrounds at low-frequencies using the Owens Valley Radio Observatory Long Wavelength Array (OVRO LWA).

In the theoretical part of this thesis, we propose a new method to measure the tensor-to-scalar ratio r using the circular polarization of the 21 cm radiation from the Dark Ages. In Chapter II we discuss the basic principles of inflationary physics, which is now accepted as a standard paradigm for the generation of perturbations in the early universe. Along with density (scalar) perturbations, inflation also produces gravitational wave (tensor) modes. In Chapter IV we outline a novel, albeit futuristic method to detect inflationary gravitational waves. Our method relies on the splitting of the $F = 1$ hyperfine level of neutral hydrogen due to the quadrupole moment of the CMB during the Dark Ages. We show that unlike the Zeeman effect, where $M_F = \pm 1$ have opposite energy shifts, the CMB quadrupole shifts $M_F = \pm 1$ together relative to $M_F = 0$. This splitting leads to a small circular polarization of the emitted 21cm photon, which is in principle observable. Further, we forecast the sensitivity of future radio experiments to measure the CMB quadrupole during the era of first cosmic light ($z \sim 20$). The tomographic measurement of 21 cm circular polarization allows us to construct a 3D remote quadrupole field. Measuring the B -mode component of this remote quadrupole field can be used to put bounds on the tensor-to-scalar ratio r . We make Fisher forecasts for a future Fast Fourier Transform Telescope (FFTT), consisting of an array of dipole antennas in a compact grid configuration, as a function of array size and observation time. The forecasts are dependent on the evolution of the Lyman- α flux in the pre-reionization era, that remains observationally unconstrained. Finally, we calculate the typical order of magnitudes for circular polarization foregrounds and comment on their mitigation strategies. We conclude that detection of primordial gravitational waves with 21 cm observations is in principle possible, so long as the primordial magnetic field amplitude is small, but would require a very futuristic experiment with corresponding advances in calibration and foreground suppression techniques.

In the observational part of this thesis, we investigate the cross-correlation between low-frequency radio maps from the Owens Valley Radio Observatory Long Wave-

length Array (OVRO LWA) and tracers of the ISM: dust, $H\alpha$, and HI. Our goal is to search for any anomalous radiative processes at low frequencies (20 – 80 MHz). In Chapter III we discuss the basic principles of 21cm cosmology and provide an overview of current and planned 21cm experiments. Broadband foreground sources pose the greatest challenge to 21cm tomography and need to be characterized carefully before the technique becomes a sensitive probe of the dark ages and the epoch of reionization. The foregrounds are expected to be predominantly galactic and approximately four orders of magnitude larger than the cosmological signal. In Chapter V, we investigate the nature of the diffuse Galactic radio emission in the 20 – 80MHz frequency range using data from the OVRO-LWA. We cross-correlate LWA maps with tracers of ISM (dust, $H\alpha$, HI) from a number of surveys, to investigate galactic foregrounds relevant to detection of 21cm signal from the Dark Ages. We describe a formalism to compute the cross-power spectra between LWA maps and ISM tracers. Our results are consistent with no correlation between tracers of the gas and dust in the ISM at high Galactic latitudes ($b > 55^\circ$) and low-frequency maps from the LWA, at scales $\ell \sim 10 - 600$ at a 99.9% confidence level.

PUBLISHED CONTENT AND CONTRIBUTIONS

Mishra, A., & Hirata, C. M., 2017, ArXiv e-prints, arXiv:1707.03514,
A.M. participated in the conception of the project, performed the analysis, and wrote the paper.

CONTENTS

Acknowledgements	v
Abstract	viii
Published Content and Contributions	x
Contents	xi
List of Figures	xiii
List of Tables	xviii
Chapter I: Introduction	1
1.1 Measuring the Universe	2
1.2 The Low Frequency Frontier: Mapping the Universe with the 21cm Line	3
1.3 Overview of this Thesis	5
1.4 Other Work	7
Chapter II: Overview of Inflationary Cosmology	9
2.1 The Physics of Inflation: Homogenous Evolution	10
Conformal Time and Causal Structure	11
Inflation: Kinematics	12
Inflation: Dynamics	13
2.2 The Physics of Inflation: Generation of Perturbations	14
Scalar Perturbations	14
Tensor Perturbations	20
2.3 Experimental Tests of Inflation	21
CMB Temperature Anisotropies	22
CMB Polarization Anisotropies	23
2.4 Conclusion	27
Chapter III: Overview of 21cm Cosmology	30
3.1 Physics of the 21cm Signal	31
3.2 Evolution of the 21cm Signal	35
3.3 Low Frequency Radio Interferometers: Basics	39
Definitions	39
Visibility Variance	40
Power spectra and noise	43
The UV coverage	45
3.4 Overview of Experimental Efforts	46
Current Efforts	46
Planned Experiments	47
Observational Challenges	48
Chapter IV: Detecting primordial gravitational waves with circular polariza- tion of the redshifted 21 cm line	50
4.1 Introduction and Motivation	51

4.2	Formalism	53
4.3	Outline of the Method	57
4.4	Measuring the Remote Quadrupole of the CMB	57
	Relation of the 21 cm power spectrum to the remote quadrupole of the CMB	58
	Local power spectrum and detectability	60
	Fast Fourier Transform Telescopes	60
	Results for reference experiments	61
4.5	Power spectrum of the remote CMB quadrupole and sensitivity to the tensor-to-scalar ratio	65
	<i>E</i> - and <i>B</i> -mode decomposition of remote CMB quadrupoles	66
	<i>B</i> -mode power spectrum of the remote CMB quadrupole	67
	Incorporation of the tensor transfer function	70
	Sensitivity to tensor-to-scalar ratio	71
4.6	Foregrounds	73
	Spectrally Smooth Circular Polarization from Synchrotron	75
	Circular Polarization Foregrounds from Faraday Rotation	76
	Extragalactic Point Sources	78
	Atmospheric Effects	81
4.7	Discussion	82
Chapter V: Characterizing Foregrounds for Redshifted 21cm Radiation Using the Long Wavelength Array: Cross-correlation with Tracers of ISM		88
5.1	Introduction	89
5.2	Motivation: Characterizing Low-Frequency Radio Foregrounds	91
5.3	The Long Wavelength Array	92
5.4	Observations and Data Processing	94
	<i>m</i> -Mode Analysis	96
5.5	External Data Sets	98
	IRAS + DIRBE/COBE Maps	98
	H α Maps	98
	HI Maps	99
5.6	Cross-Correlation Power Spectrum Analysis	99
	Sky Cuts	99
	Methodology	99
	Errors	102
	Priors	102
	<i>m</i> -Mode suppression	102
	Simulations and Tests	103
5.7	Results	103
5.8	Implications for 21cm Foregrounds	107
	Dust	107
	H α emission	110
5.9	Conclusion	110
5.10	Appendix A: Statistical Tests	112

LIST OF FIGURES

<i>Number</i>	<i>Page</i>
1.1 The cosmic microwave background map after removal of galactic and extragalactic foregrounds from the Planck mission gives us a snapshot of a nearly homogeneous universe around 380,000 years after the big bang.	3
1.2 Different cosmological probes and the length scales they probe adapted from Tegmark & Zaldarriaga 2002: The figure shows power spectrum of density fluctuations in the Universe as predicted by the Λ CDM model (red line) and the various probes used to measure the power spectrum at different length scales. This figure is based on data available in 2002 and cosmological LSS probes have advanced significantly since then. However, the essential mapping of probes to scales is the same.	4
2.1 Conformal diagram for standard FRW cosmology. In standard cosmology there are $\sim 10^5$ causally disconnected patches (figure adopted from Baumann 2009).	10
2.2 Inflation extends conformal time to negative values. The end of inflation is at $\tau = 0$. As we can see in the figure, causally disconnected patches at $\tau = 0$ were in causal contact before inflation (figure adopted from Baumann 2009).	11
2.3 Inflation postulates that the energy density of the universe is dominated by the vacuum energy associated with the displacement of a scalar field (the inflaton). The inflaton potential is unknown and needs to be constrained by observations. Here, shown for illustration are two toy models for the inflaton potential from ((figure adopted from Kamionkowski & Kovetz 2016)).	13
2.4 All scales that are relevant to cosmological observations today were larger than the Hubble radius until $a \sim 10^{-5}$. However, at sufficiently early times, these scales were smaller than the Hubble radius and therefore causally connected. Figure adopted from Baumann 2009.	20

2.5	Current constraints on the scalar spectral index n_s and tensor-to-scalar ratio r , for a variety of slow-roll inflationary models. Figure adopted from Planck Collaboration et al. 2016.	24
2.6	The top panel shows a polarization pattern composed only of E modes. The polarization pattern is tangential around hot spots and radial around cold spots. The bottom panel shows a polarization pattern composed only of B modes. The polarization pattern surrounding hot and cold spots of the B mode show a swirling pattern. Note that the E -mode is parity invariant while the B -mode is not. Figure adopted from Kamionkowski & Kovetz 2016.	25
2.7	Theoretical predictions for the temperature (black), E -mode (red), and tensor B -mode (blue) power spectra. Also shown are expected values lensing B -modes (green). Current measurements of the B -mode for BICEP2/Keck Array (yellow), POLARBEAR (orange), and SPTPol (dark orange). Figure adopted from Abazajian et al. 2016.	26
3.1	21 cm observations can potentially map the largest volumes of the observable universe, while the CMB can probe a 2D surface at $z \sim 1100$. and LSS surveys can map small volumes of the local universe. Note that more than half of the comoving volume of the universe lies at $z > 20$. Figure adopted from Tegmark & Zaldarriaga 2009.	31
3.2	The transitions relevant for the Wouthuysen-Field effect. Solid line transitions contribute to spin flips. Transitions denoted by dashed lines are allowed but do not contribute to spin flips. Figure adopted from Pritchard & Loeb 2012.	33
3.3	The evolution of the 21 cm global signal depends on different physical processes at different epochs. The evolution of the brightness temperature T_b leads to the 21cm signal appear either in absorption or in emission against the CMB. The top panel shows a slice through a simulation showing the evolution of T_b and the heating due to the first generation stars and galaxies. The bottom panel shows the sky-averaged global 21 cm signal, which largely traces the evolution of the spin temperature and neutral fraction of hydrogen. Figure adopted from Pritchard & Loeb 2012.	34

3.4	The evolution of the 21 cm power spectrum as a function of the ionized fraction is expected to reveal the astrophysical processes that drove reionization and the nature of the first stars and galaxies. The right side of the y-axis shows neutral fraction of the universe. As the universe goes from almost neutral (yellow) to ionized (gray), the overall amplitude of the power spectrum decreases. Moreover, as reionization proceeds the high- k power decreases since reionization bubbles start forming at small scales and then grow to larger scales.	36
3.5	The evolution of the universe from the CMB (extreme left) to the current day (extreme right). After the CMB the universe goes through the Dark Ages when it is largely neutral. As the first stars and galaxies light up, the universe gets reionized. Reionization is inhomogeneous and fills the the universe with merging bubbles of ionized hydrogen. Image credit: HERA/Avi Loeb/SciAm	38
3.6	Schematic of a two antenna interferometer.	41
4.1	Energy Level Splitting	54
4.2	Tomographic measurements by Fast Fourier Transform Telescopes (FFTTs) would allow us to measure the remote quadrupole of the CMB $a_{2m}(z)$ ($m = 1, 2$) in volume pixels ("voxels") of volume \mathcal{V}_c in narrow slice of redshift space. Creating a map of remote quadrupole moments across many voxels allows us to construct a spin-weight m field, which can be decomposed into E and B modes. Measurement of the B -modes of this field allows us to put bounds on the tensor-to-scalar ratio r	58
4.3	Inputs used for the sensitivity calculation, computed for standard cosmology using the 21CMFAST code. The plot shows the fiducial models for spin, kinetic, and CMB temperatures.	62
4.4	Inputs used for the sensitivity calculation, computed for standard cosmology using the 21CMFAST code. The plot shows the fiducial models for quantities that parametrize the rate of depolarization of the ground state by optical pumping and atomic collisions as discussed in the text and in Gluscevic et al. 2017	63
4.5	Temperature, circular polarization, and noise power spectra relevant to the Fisher calculation. We compute the power-spectra for observations corresponding to $z = 19.5$. Noise power-spectra for two different configurations of FFTTs are shown.	64

4.6	Elements of the Fisher matrix w_1 as a function of redshift z , computed for a model of reionization described in the text. For our fiducial model, both w_1 and w_2 peak at $z = 19.5$, i.e. the redshift where the Lyman-alpha coupling becomes efficient ($\tilde{x}_\alpha \sim 1$).	65
4.7	Elements of the Fisher matrix w_2 as a function of redshift z , computed for a model of reionization described in the text. For our fiducial model, both w_1 and w_2 peak at $z = 19.5$, i.e. the redshift where the Lyman-alpha coupling becomes efficient ($\tilde{x}_\alpha \sim 1$).	66
4.8	Forecasts for σ_r for different FFTT telescope configurations. The parameters used to make these forecasts are described in Fig. 4.4 & 4.3 and in Section 4.4. For the given Lyman- α flux model the values of weights w_1 and w_2 peak around $z \sim 19.5$ as shown in Fig. 4.7. For our forecasts we consider a shell with $z_{min} = 18$ and $z_{max} = 23$. Note that the live observation time quoted here will be shorter than the wall-clock time of the survey.	72
4.9	Order of magnitude of expected foregrounds for the circular polarization signal from Galactic synchrotron (purple line) and due to Faraday rotation through the ISM (orange line) compared against the noise power spectra expected for for three different configurations of FFTTs.	77
4.10	Order of magnitude of expected foregrounds for the circular polarization signal from unresolved point sources (blue, green, and purple line) and Faraday rotation due to the ionosphere (orange line) compared against the noise power spectra expected for three different configurations of FFTTs.	79
5.1	Map of the antenna layout for OVRO LWA. Black circles correspond to the 251 core antennas. The black triangles correspond to the 32 expansion antennas that extend the maximum baseline of the array. The 5 crosses are antennas equipped with noise-switched front ends for calibrated total power measurements. This figure was provided courtesy of Michael Eastwood and to be published in Eastwood et. al. (in prep)	93
5.2	3-color all-sky map generated with m-mode analysis imaging techniques. This figure was provided courtesy of Michael Eastwood and to be published in Eastwood et. al. (in prep)	95
5.3	Outline for powspec	101

5.4	Cross-spectra between LWA map and Dust map with power injected in the $l = 250 - 300$ band	103
5.5	Recovered auto-power spectrum of the dust map with power injected in the $l = 250 - 300$ band	104
5.6	Dust map correlations with the six LWA maps for the northern sky-cut. The correlations are normalized with the auto-spectra as described in the text	105
5.7	H α map correlations with the five LWA maps for the northern sky-cut. The correlations are normalized with the auto-spectra as described in the text	106
5.8	HI map correlations with the five LWA maps for the northern sky-cut. The correlations are normalized with the auto-spectra as described in the text	107
5.9	Upper limits on the dust emissivity at low-frequencies in terms of $\tau_{100\mu m}$, the optical depth at $100\mu m$	109
5.10	Upper limits on the electron temperature as a function of scale from cross-correlation of LWA maps with H α template, for a synchrotron temperature $T_{sync} = 1000K$	111

LIST OF TABLES

<i>Number</i>	<i>Page</i>
5.1	Summary of LWA maps used for cross-correlations 104
5.2	Summary statistics for t -tests on the LWA \times Dust cross-correlation to check for zero correlation. The t -statistic is calculated for each ℓ bin under a null hypothesis that there is zero cross-correlation in the given ℓ bin, with 7 d.o.f. (since there are 8 jackknife regions). First row for a given ℓ band reports the t -statistic and the corresponding p-value is given in the second row for a given ℓ band. 113
5.3	Summary statistics for t -tests on the LWA \times H α cross-correlation to check for zero correlation. The t -statistic is calculated for each ℓ bin under a null hypothesis that there is zero cross-correlation in the given ℓ bin, with 7 d.o.f. (since there are 8 jackknife regions). First row for a given ℓ band reports the t -statistic and the corresponding p-value is given in the second row for a given ℓ band. 114
5.4	Summary statistics for t -tests on the LWA \times HI cross-correlation to check for zero correlation. The t -statistic is calculated for each ℓ bin under a null hypothesis that there is zero cross-correlation in the given ℓ bin, with 7 d.o.f. (since there are 8 jackknife regions). First row for a given ℓ band reports the t -statistic and the corresponding p-value is given in the second row for a given ℓ band. 115

Chapter 1

INTRODUCTION

“For the Ancient Greeks, the future was something that came upon them from behind their backs, with the past receding away before their eyes. When you think about it, that’s a more accurate metaphor than our present one. Who really can face the future? All you can do is project from the past, even when the past shows that such projections are often wrong. And who really can forget the past? What else is there to know?”

-Robert M. Pirsig, *Zen and the Art of Motorcycle Maintenance*

One of the most remarkable consequences of the theory of relativity is that our ability to look further into space allows us to peer back into our past. Over the last century, breathtaking theoretical and technological innovations have allowed us to probe large volumes of the universe, allowing us to reconstruct our cosmic history, from the Big Bang to the present day. Cosmology today is no longer an esoteric philosophical exercise; instead it is a rigorous empirical science.

An avalanche of data from the cosmic microwave background (CMB), galaxy surveys, gravitational lensing, supernova studies, cluster counts and chemical abundance studies have led to the construction of a "concordance" model of modern cosmology, with tightly constrained parameters. The broad consensus about the history of the universe is as follows: the universe began through an exponentially expanding phase called inflation, which seeded the initial perturbations in density. These density perturbations then grew via gravitational collapse to form stars and galaxies and the complex cosmic web we see today.

However, the standard "concordance" model throws up as many mysteries as it aims to explain. According to the standard model, the universe today consists of only 5% baryonic matter, 27% dark matter that consists of particles that are not part of the standard model of particle physics, and perhaps most mysteriously and 68% dark energy, about which, we know very little about. The leading candidate for dark energy is the cosmological constant Λ , which leads to accelerated expansion during late stages of the universe’s evolution and whose energy density remains constant as the universe expands. Dark matter on the other hand is posited to be "cold" (i.e. particle velocities are non-relativistic) and collisionless (i.e the particles do not have

electromagnetic or strong interactions with baryonic matter, and likely don't have any self-interaction). Together these compose the standard Λ CDM model of the universe.

While parameters of the concordance model of the universe are accurately measured, the physical underpinnings of these parameters remain far from clear. The biggest questions that remain unanswered are: what is dark matter? What is the nature of dark energy? How did the universe evolve from a smooth initial state to the complex structures we see around us? And finally, what is the physics of the process that generates perturbations in the early universe? The work presented in this thesis presents some new avenues to approach these questions. The first part of this thesis presents a novel way to test inflation using circular polarization of the 21cm line emitted by neutral hydrogen at high redshifts. The second part of the thesis investigates some observational challenges in probing the universe using 21cm radiation.

The rest of the chapter is organized as follows: in Sec. 1.1 we provide a whirlwind overview of different observational probes of the universe, in Sec. 1.3 we provide an overview of this thesis.

1.1 Measuring the Universe

The standard cosmological model is essentially parameterized by two functions: the cosmic expansion history $a(t)$ and the cosmic clustering history, in terms of the power spectrum at different redshifts $P(k, z)$. The cosmic expansion history is determined by the zeroth order Friedmann equation and depends on the energy budget of the universe as well as the equation of state of dark energy. The power spectrum $P(k, z)$ can be factored as a product of the *primordial* power spectrum that depends on the physics of the early universe and a transfer function that characterizes the physics of late stage evolution.

There are several observational probes of $P(k, z)$ using the fluctuations inside our observable horizon. The most widely-known is the Cosmic Microwave Background (CMB), which is the relic radiation from when the universe was around 400,000 years old. The density fluctuations in the CMB have been measured with exquisite precision by a number of experiments, most recently by the Planck satellite. Fig. 1.1 shows the map of the CMB after removal of galactic and extragalactic foregrounds.

The other probes of cosmological fluctuations include the distribution of galaxies, the Lyman- α forest, weak lensing, and cluster abundances. These probes measure

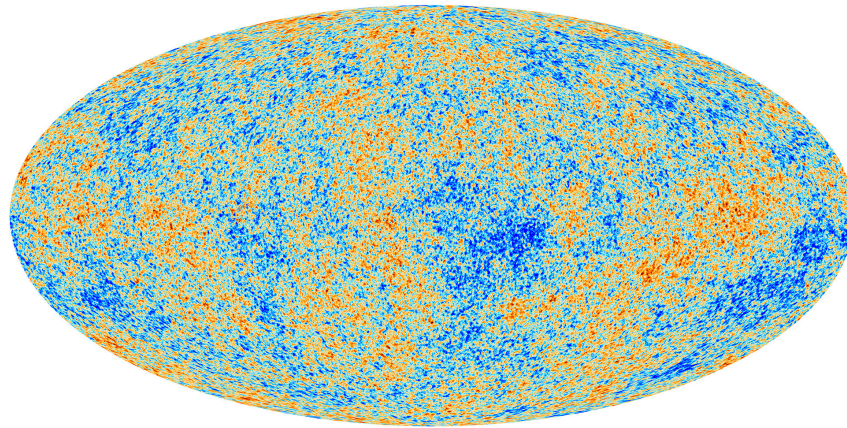


Figure 1.1: The cosmic microwave background map after removal of galactic and extragalactic foregrounds from the Planck mission gives us a snapshot of a nearly homogeneous universe around 380,000 years after the big bang.

fluctuations in the universe at much smaller scales and at later stages. As such their interpretation has to deal with complicated non-linear effects as well as more messy astrophysics during the late stages of the universe. Fig. 1.2 from Tegmark & Zaldarriaga 2002 shows the different probes that measure the matter power spectrum at various scales. As evident from the figure, the CMB probes the largest scale fluctuations while Large Scale Structure (LSS) probes smaller and intermediate length scales.

1.2 The Low Frequency Frontier: Mapping the Universe with the 21cm Line

Given the deluge of information about the content and evolution of the universe, one might wonder: what next? Beyond the three big questions discussed in the previous section, the details of the evolution of the universe since the epoch of recombination to the present day remains to be observationally constrained. Recent measurements have put stringent constraints on the nature of this evolution, but there are no direct measurements of the major phase changes in the universe since recombination. For about 800 million years after the big bang, the universe consisted primarily of neutral hydrogen. After the formation of the first luminous objects, the hydrogen atoms got "re-ionized" and eventually led to the formation of stars and galaxies that we see

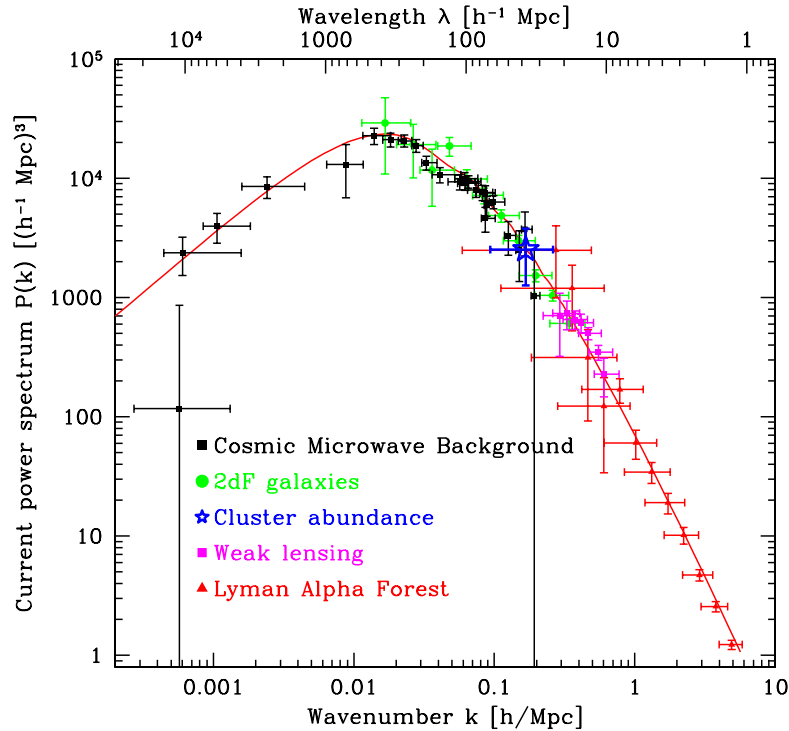


Figure 1.2: Different cosmological probes and the length scales they probe adapted from Tegmark & Zaldarriaga 2002: The figure shows power spectrum of density fluctuations in the Universe as predicted by the Λ CDM model (red line) and the various probes used to measure the power spectrum at different length scales. This figure is based on data available in 2002 and cosmological LSS probes have advanced significantly since then. However, the essential mapping of probes to scales is the same.

today.

This thesis deals with theoretical and observational aspects of one of the frontiers of modern observational cosmology: the use of 21cm radiation from the hyperfine splitting of neutral hydrogen to probe the universe during the first billion years, from the so called Dark Ages to the late stage reionized universe. Current and upcoming 21cm experiments are poised to revolutionize cosmology by enabling a detailed understanding of astrophysics: when did the first stars form? When did reionization begin? What reionized the universe? 21cm experiments will also revolutionize cosmology and fundamental physics by allowing for the measurement of the largest accessible volume inside the horizon.

One of the crucial periods of cosmic evolution that 21cm experiments aim to constrain is the Epoch of Reionization (EoR). The current evidence and constraints

on reionization come from the absorption of the Lyman- α line in the spectra of high-redshift quasars. The optical depth to neutral hydrogen for Lyman- α photons is extremely high, implying that even a small fraction of neutral hydrogen in the universe saturates the absorption signature. This leads to the Gunn-Peterson trough Gunn & Peterson 1965, which can help constrain the redshift when the universe is almost entirely ionized. Observations indicate that this redshift is around $z \sim 6$. Large scale fluctuations in the polarization of the CMB also helps constrain the stage when the reionization was partially complete. Recent Planck data Planck Collaboration et al. 2016 indicates that the average redshift at which reionization occurs is likely between $z = 7.8$ and 8.8 . The data also indicates that the Universe was ionized at less than the 10% level at redshifts above $z \sim 10$ ruling out models of early reionization. Other constraints on reionization come from Lyman- α damping wings of high redshift Gamma-Ray Bursts (Miralda-Escudé 1998; Barkana & Loeb 2004) and from the detection of high-redshift galaxies (Robertson et al. 2010).

While we have a broad-brush picture of the process of reionization, the details of the process are rather poorly understood. When did the first stars form and what was their composition? How did the first X-ray sources affect the evolution of the IGM? What was the role of blackholes, both supermassive as well as stellar mass? How did the Lyman- α background evolve just prior to reionization?

Astronomy, however, is still fundamentally a discovery driven science. As we shall see in subsequent chapters, the real promise of 21cm experiments lies in their ability to make 3D maps of the universe at scales that are unprecedented. This cosmic cartography will enable us to not just measure known cosmological parameters with great accuracy, it will very likely provide new surprises. The volumes that these experiments will open up will enable quite literally the largest physics laboratories in the universe. Beyond measuring cosmological parameters, this laboratory can potentially be used to answer fundamental physical questions such as constraining the strength of primordial magnetic fields, detect annihilating dark matter, or constraining models of early Dark Energy.

1.3 Overview of this Thesis

With cosmology poised to undergo a revolution with upcoming 21cm experiments, it is timely to investigate the scientific promises and the observational challenges associated with these efforts. This thesis provides two new contributions, one theoretical and one observational, to the field of 21cm cosmology.

The theoretical part of the thesis proposes a new way to detect inflationary gravitational waves using the circular polarization of the 21cm line. Unlike linear polarization, which gets scrambled up due to Faraday rotation, circular polarization of 21cm is expected to be a relatively clean signal. Given the scientific interest in testing inflation via the detection of gravitational waves from the early universe, this method provides a novel experimental strategy for the future. While the experiments that can use the circular polarization method are still rather futuristic at this stage, the technique highlights the rich array of physical processes that can be probed by future 21cm experiments. Given the long-term interest in testing inflationary physics, this method will hopefully help make the scientific case for the ultimate 21cm experiment. The material relevant to the theoretical part of the thesis are contained in Chapter II, which discusses the fundamentals of inflationary cosmology and Chapter IV, which outlines the new technique for detecting inflationary GWs using circular polarization.

The observational part of the thesis uses new data from Owens Valley Long Wavelength Array (OVRO LWA) and publicly available ISM tracer maps to investigate potential galactic foregrounds at low frequencies. 21cm experiments are limited by the dynamic range they can achieve against low-redshift sources of low-frequency radio emission. Multi-frequency maps produced by the LWA provide a powerful tool to characterize the low-frequency radio emission from our own Galaxy. We describe a technique to detect cross-correlations between LWA maps and known tracers of the ISM: dust, $H\alpha$, and HI. We conclude this part of the thesis by putting the first upper limits on the level of cross-correlation between low-frequency maps and tracers of the ISM. The major contribution of this part of the thesis is ruling out any anomalous ISM emission at low-frequencies. The material relevant to the observational part of the thesis are contained in Chapter III, which discusses the fundamentals of 21cm cosmology and Chapter V, which reports results of the cross-correlation analysis using LWA and ISM maps.

The work presented in this thesis was originally written in two papers, one of which has been submitted to the arxiv (<https://arxiv.org/abs/1707.03514>) and other will be submitted with the LWA data release. The papers are:

- "Detecting Primordial Gravitational Waves With Circular Polarization of the Redshifted 21cm Line- Forecasts" which was led by me. The formalism for the generation of circular polarization due to inflationary gravitational waves was led by my advisor (which led to "Paper-I" of the series) and

the forecasts for future experiments was led by me (“Paper-II”). I also led the estimation of circular polarization foregrounds that are important for the proposed technique.

- "Characterizing foregrounds for redshifted 21cm radiation using the Long Wavelength Array: cross-correlation with Tracers of the ISM" which was written in collaboration with Michael Eastwood. Michael produced the LWA maps (which will be published in a separate paper) and I led the cross-correlation analysis.

It is my hope that this thesis will communicate the scientific promise of 21cm cosmology, even though some of the ideas presented might be rather futuristic, while also providing a pragmatic view of the observational challenges that need to be overcome.

1.4 Other Work

During my thesis I also contributed to other papers that are not included as a part of this thesis. These include:

- "Detecting Primordial Gravitational Waves With Circular Polarization of the Redshifted 21cm Line- Formalism" led by my advisor Chris Hirata. This paper provides the formalism for the generation of 21cm circular polarization due to a remote quadrupole field. I was involved in the writing of the paper and the calculation connecting the circular polarization signal to observable power-spectra (which is included in a separate the forecasts paper). I provide a broad outline of the calculation reported in this paper in Chapter IV.
- "A new probe of magnetic fields in the pre-reionization epoch: II Detectability" led by Vera Gluscevic. This paper makes forecasts for detecting extremely small primordial magnetic fields using the local anisotropy of the 21cm temperature power spectrum. We show that depending on the reionization history, and subject to the control of systematics from foreground subtraction, an array of dipole antennas in a compact grid configuration with a collecting area slightly exceeding one square kilometer can achieve a 1σ detection of magnetic fields with strength 10^{-21} Gauss comoving (scaled to present day value) within three years of observation. I was involved in the calculation of the noise power spectra.

- "Inflationary Freedom and Cosmological Neutrino Constraints" led by Roland de Putter. In this paper we show that combining CMB and LSS datasets can help robustly constrain the sum of neutrino masses to $\sum m_\nu < 18\text{eV}$ at 95% confidence level using Planck+BOSS+H0 measurements *without making assumptions* about the shape or functional form of the primordial power spectrum. I was involved in the data analysis using Planck and BOSS data, including modifying CAMB to include a free-form primordial power spectrum, and generating parameter constraints for the free-form power spectrum. I was also involved in the interpretation of the results and writing of the paper.

References

- Barkana, R., & Loeb, A., 2004, ApJ, 601, 64
- Gunn, J. E., & Peterson, B. A., 1965, ApJ, 142, 1633
- Miralda-Escudé, J., 1998, ApJ, 501, 15
- Planck Collaboration, Adam, R., Aghanim, N., et al., 2016, A&A, 596, A108, A108
- Robertson, B. E., Ellis, R. S., Dunlop, J. S., McLure, R. J., & Stark, D. P., 2010, Nature, 468, 49
- Tegmark, M., & Zaldarriaga, M., 2002, PhRvD, 66.10, 103508, 103508

Chapter 2

OVERVIEW OF INFLATIONARY COSMOLOGY

Despite the breathtaking diversity in structure at planetary and galactic scales, the universe is remarkably homogeneous at the largest scales. The homogeneity of the observable universe is one of the key observational puzzles of modern cosmology. In the standard big-bang model, patches in the sky that are larger than 2 degrees across in angular size should be causally independent and hence cannot thermalize. However, observations of the Cosmic Microwave Background (CMB) by Penzias & Wilson (Penzias & Wilson 1965) showed that the CMB was remarkably smooth on large scales. In fact the CMB, which traces the matter distribution in the early universe, is homogeneous to better than one part in 10,000. This remarkable smoothness of the CMB at the largest scales is known as the *horizon problem*. Figure 2.1 illustrates the horizon problem schematically in the standard cosmological model.

A second puzzle in observational cosmology is that the total energy density of the universe is almost equal to the critical energy density. There is no natural physical explanation for this value in the standard big-bang model and it leads to what is known as the *flatness problem*. In a series of papers in the early 1980s (Guth 1981; Albrecht & Steinhardt 1982; Linde 1982), it was hypothesized that a period of exponential expansion in the earliest stages of the universe, known as *inflation* can solve both of these puzzles. The idea postulated that a new scalar field in the very early universe could drive this exponential expansion. Inflation would thus take a small, causally connected patch in the very early universe and expand it to the size of the observable universe.

A by-product of an exponentially expanding phase is the generation of perturbations in the metric (Guth & Pi 1982; Hawking 1982; Linde 1982; Rubakov et al. 1982), hence inflation not only solves the horizon and flatness problems but provides a natural explanation for the generation of structure in the universe: the scalar component of these perturbations lead to density perturbations we observe at the largest scales. Inflation also predicts the generation of *tensor* modes or gravitational waves; the detection of these gravitational waves will thus be a ‘smoking gun’ for inflation and provide a window into the earliest, most energetic epoch of the universe.

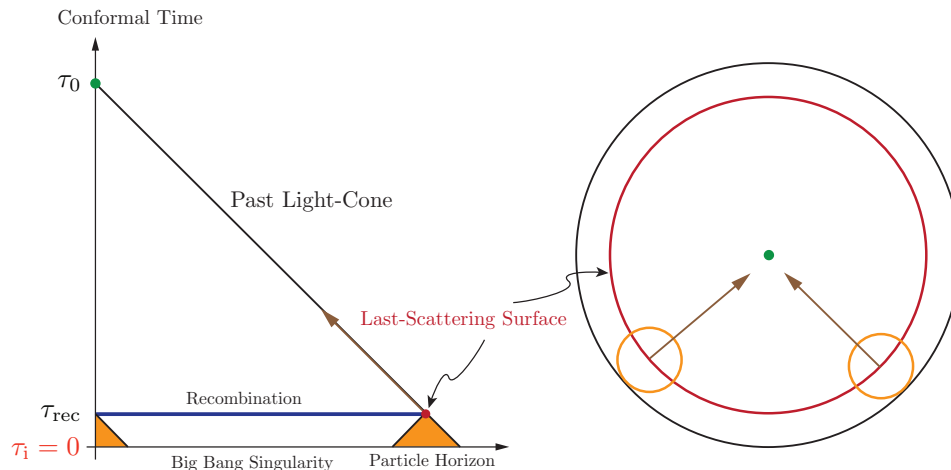


Figure 2.1: Conformal diagram for standard FRW cosmology. In standard cosmology there are $\sim 10^5$ causally disconnected patches (figure adopted from Baumann 2009).

In this chapter we aim to provide a brief review of inflationary physics starting with the homogeneous background evolution during inflation and the generation of perturbations. We also discuss the the proposed experimental tests of inflation using CMB polarization. The formalism outlined in this chapter will provide useful background for our discussion in Chapter IV. Details of the calculations outlined in this chapter can be found in standard textbooks (eg: Dodelson 2003) or review articles (see for eg Kamionkowski & Kovetz 2016).

2.1 The Physics of Inflation: Homogenous Evolution

An expanding homogeneous and isotropic Universe can be described by a Friedmann-Robertson-Walker (FRW) metric at the largest scales:

$$ds^2 = -dt^2 + a^2(t) \left(\frac{d\mathbf{r}^2}{1 - kr^2} + r^2 d\Omega^2 \right) \quad (2.1)$$

where $a(t)$ is the scale factor parametrizing the background expansion rate. The growth rate of the universe (Hubble parameter) is given by,

$$H \equiv \frac{\dot{a}}{a} \quad (2.2)$$

Assuming the evolution of the universe at the largest scales is governed by general relativity, the equation of motion for the scale factor is given by the Friedmann equations:

$$H^2 = \frac{\rho}{3M_{\text{pl}}^2} \quad H + \dot{H}^2 = -\frac{\rho + 3p}{6M_{\text{pl}}^2} \quad (2.3)$$

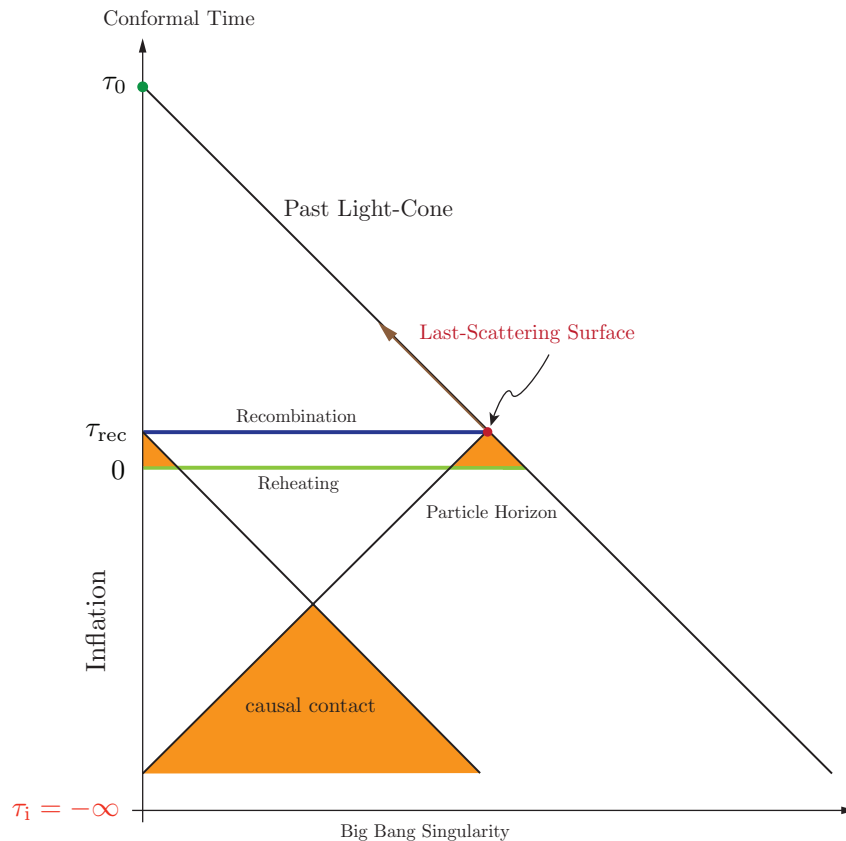


Figure 2.2: Inflation extends conformal time to negative values. The end of inflation is at $\tau = 0$. As we can see in the figure, causally disconnected patches at $\tau = 0$ were in causal contact before inflation (figure adopted from Baumann 2009).

where p and ρ are the density and pressure of the background stress-tensor, which is assumed to be a perfect fluid. This is a valid assumption for a universe which is dominated by dark matter. Here we assume $\hbar = c = 1$, Newton's constant $G = 1/(8\pi M_{\text{Pl}})^2$, and Planck mass, $M_{\text{Pl}} = 2.435 \times 10^{18}$ GeV.

Conformal Time and Causal Structure

We now turn to the kinematics of light-rays in the FRW metric- the kinematics of light- or null curves- determines the causal structure of the FRW spacetime. Null curves are defined by the condition $ds^2 = 0$. They are easier to describe in terms of the *conformal time* that is defined as¹,

$$\tau = \int \frac{dt}{a(t)} \quad (2.4)$$

¹note that conformal time is sometimes denoted by η (as we do in Chapter IV). However, η is used to denote one of the the slow-roll parameters in this chapter hence the use of τ for conformal time.

With this definition, and assuming spatial isotropy, we can write the FRW metric as,

$$ds^2 = a^2(\tau)[-d\tau^2 + d\chi^2] \quad (2.5)$$

which is the Minkowski metric scaled by a time-dependent conformal factor $a(\tau)$. In the metric defined by Eq. 2.5, light-rays travel in straight lines at $\pm 45^\circ$ in the $\tau - \chi$ plane, making it easy to understand the causal structure of an isotropic, curved spacetime like the FRW metric.

Another quantity of interest is the the maximal comoving distance that light can travel between two times τ_1 and τ_2 , known as the (*comoving*) *particle horizon*. The size of the particle horizon from a given spacetime point determines the causally connected region of spacetime,

$$\chi(\tau) = \tau - \tau_i = \int_{\tau_i}^{\tau} \frac{dt}{a(t)} \quad (2.6)$$

The particle horizon where t_i corresponds to the big-bang singularity (i.e. $a(t) = 0$) can be written as

$$\tau = \int_0^{\tau} \frac{dt}{a(t)} = \int (aH)^{-1} d \ln a \quad (2.7)$$

The conformal time is thus proportional to (though not equal to) the comoving Hubble radius $(aH)^{-1}$.

Inflation: Kinematics

The dynamics of the universe during the radiation and matter dominated stage is governed by,

$$\frac{d}{dt}(aH)^{-1} > 0 \quad (2.8)$$

which implies that an observer in an expanding background will see a growing horizon of size H^{-1} . In this case more information enters the horizon as time progresses.

For background evolution during inflation, this condition is reversed, i.e. $d/dt(aH)^{-1} < 0$, which leads to a *shrinking Hubble sphere* and an exponentially growing scale factor $a(t) \propto e^{Ht}$.

We define the equation of state parameter as,

$$w \equiv \frac{P}{\rho} \quad (2.9)$$

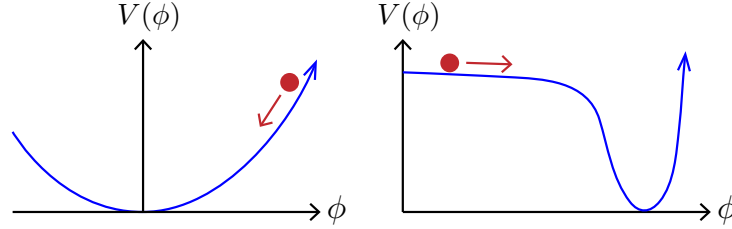


Figure 2.3: Inflation postulates that the energy density of the universe is dominated by the vacuum energy associated with the displacement of a scalar field (the inflaton). The inflaton potential is unknown and needs to be constrained by observations. Here, shown for illustration are two toy models for the inflaton potential from ((figure adopted from Kamionkowski & Kovetz 2016)).

Defining $\epsilon \equiv -\dot{H}/H^2$, Friedmann equations imply,

$$\epsilon = \frac{3}{2}(1 + w) \quad (2.10)$$

Inflation thus requires that $w < -1/3$.

Inflation: Dynamics

The equation of state necessary for inflation comes from the a hypothesized scalar field ϕ called the "inflaton" with an associated potential $V(\phi)$ (see Figure 2.3).

During inflation, the stress-energy tensor of universe is dominated by the scalar field and it sources the evolution of the FRW background. We now set out to determine the conditions under which the scalar field can lead to accelerated expansion. The pressure and energy density components of the stress-energy tensor are given by,

$$p = \frac{\dot{\phi}^2}{2} - V(\phi) ; \rho = \frac{\dot{\phi}^2}{2} + V(\phi) \quad (2.11)$$

The corresponding Friedmann equation governing time-evolution ϕ is given by,

$$\ddot{\phi} + 3H\dot{\phi} + \partial_{\phi}V(\phi) = 0 \quad (2.12)$$

Note that here the potential acts like a *driving force* $\partial_{\phi}V(\phi)$ while the expansion of the universe acts like a *friction* term $H\dot{\phi}$.

We now define two quantities (called the slow-roll parameters) as,

$$\epsilon \equiv -\frac{\dot{H}}{H^2} = \frac{\dot{\phi}^2}{2M_{\text{pl}}^2 H^2} \quad (2.13)$$

and

$$\eta = \frac{\dot{\epsilon}}{H\epsilon} \quad (2.14)$$

For inflation to occur both $\epsilon, \eta < 1$.

We now make two approximations to simplify the equation of motion (Eq. 2.12). First, we assume that $\epsilon \ll 1$ implying $\dot{\phi}^2/2 \ll V(\phi)$, leading to a simplification of the Friedmann equation to,

$$H^2 \approx \frac{V}{3M_{\text{pl}}^2} \quad (2.15)$$

This implies that the Hubble rate during inflation is determined entirely by the inflaton potential. The second assumption we impose is $\eta \ll 1$, which simplifies the equation of motion (Eq. 2.12) to,

$$3H\dot{\phi} \approx -\partial_{\phi}V(\phi) \quad (2.16)$$

We thus have reduced a second order equation of motion to a first order equation, needing us to specify only one initial condition.

Together these two conditions are known as the *slow roll approximation* which can be summarized as,

$$\epsilon \approx \frac{M_{\text{pl}}^2}{2} \left(\frac{\partial_{\phi}V}{V(\phi)} \right)^2 \ll 1 \quad (2.17)$$

and

$$\eta = -2\frac{\dot{H}}{H^2} - \frac{\dot{\epsilon}}{2H\epsilon} \ll 1 \quad (2.18)$$

2.2 The Physics of Inflation: Generation of Perturbations

In this section we provide a brief discussion of the generation of primordial density and tensor perturbations from quantum fluctuations during inflation. The discussion does not delve into the technical details of the calculation (for details see Baumann 2009). Instead we provide a heuristic outline for the calculation.

Scalar Perturbations

Consider a scalar field ϕ that varies in space and time. Since the energy density is dominated by ϕ , spatial fluctuations in ϕ will lead to spatial fluctuations in the energy density which will induce fluctuations in the spacetime metric.

The perturbations for the scalar field and the metric during inflation are given by,

$$\phi(t, \mathbf{x}) = \bar{\phi}(t) + \delta\phi(t, \mathbf{x}), \quad g_{\mu\nu}(t, \mathbf{x}) = \bar{g}_{\mu\nu}(t) + \delta g_{\mu\nu}(t, \mathbf{x}), \quad (2.19)$$

where

$$\begin{aligned} ds^2 &= g_{\mu\nu} dx^\mu dx^\nu \\ &= -(1 + 2\Phi)dt^2 + 2aB_i dx^i dt + a^2[(1 - 2\Psi)\delta_{ij} + E_{ij}]dx^i dx^j \end{aligned} \quad (2.20)$$

The metric perturbations can be decomposed into Scalars, Vectors, and Tensors (the SVT decomposition), given by,

$$B_i \equiv \partial_i B - S_i, \quad (2.21)$$

where

$$\partial^i S_i = 0, \quad (2.22)$$

and

$$E_{ij} \equiv 2\partial_{ij} E + 2\partial_{(i} F_{j)} + h_{ij}, \quad (2.23)$$

where

$$\partial^i F_i = 0, \quad h^i_i = \partial^i h_{ij} = 0. \quad (2.24)$$

We ignore the vector perturbations, S_i and F_i since they decay with the expansion of the universe. Instead we focus on the scalar and tensor modes.

An important characteristic of perturbations in GR are that they are not unique, but depend on the choice of coordinates or *gauge*. Note that tensor fluctuations are gauge-invariant, but scalar fluctuations depend on the choice of gauge. We choose a gauge defined by vanishing momentum density i.e. $\delta T_{0i} = 0$ which corresponds to $\delta\phi = 0$. This is known as the *comoving gauge*. The scalar metric (to linear order in perturbation theory) can be written as,

$$g_{0\nu} = 0 ; g_{ij} = a^2(t) \exp[2\zeta(\vec{x}, t)]\delta_{ij} \quad (2.25)$$

where $\zeta(\vec{x}, t)$ is the *curvature perturbation*. The $\phi = 0$ comoving spatial surfaces have a three-curvature of $R_{(3)} = 4/a^2 \nabla^2 \zeta$ and hence ζ is referred to as the *comoving curvature perturbation*. It can be shown that ζ is conserved on super-horizon scales for adiabatic fluctuations irrespective of the equation of state of the matter. This provides an essential link between the fluctuations created during inflation and observables in the late universe.

The non-dynamical metric perturbations δg_{00} and δg_{0i} are further related to ζ through the Einstein equations; this removes another extra metric degree of freedom. We provide a quick overview of the ADM formalism that relates δg_{00} , δg_{0i} , and ζ

through constraint equations and how it can be used to compute the second-order action for the comoving curvature perturbation in quadratic order in ζ .

For the slow-roll model described earlier, the action is given by,

$$S = \frac{1}{2} \int d^4x \sqrt{-g} [R - (\nabla\phi)^2 - 2V(\phi)] , \quad (2.26)$$

Our goal is to compute the perturbations of this action due to fluctuations in the scalar field and the metric in the ADM formalism. In the ADM formalism the spacetime is sliced into three-dimensional hypersurfaces given by

$$ds^2 = -N^2 dt^2 + g_{ij}(dx^i + N^i dt)(dx^j + N^j dt) . \quad (2.27)$$

where g_{ij} is the three-dimensional spatial metric on constant t -slices. The lapse function $N(\mathbf{x})$ and the shift function $N_i(\mathbf{x})$ contain the same information as the metric perturbations Φ and B . They correspond to non-dynamical Lagrange multipliers in the action. In the ADM formalism, the action can be written as,

$$S = \frac{1}{2} \int d^4x \sqrt{-g} \left[NR^{(3)} - 2NV + N^{-1}(E_{ij}E^{ij} - E^2) + N^{-1}(\dot{\phi} - N^i \partial_i \phi)^2 - Ng^{ij} \partial_i \phi \partial_j \phi - 2V \right] , \quad (2.28)$$

where

$$E_{ij} \equiv \frac{1}{2}(\dot{g}_{ij} - \nabla_i N_j - \nabla_j N_i), \quad E = E^i_i . \quad (2.29)$$

E_{ij} is related to the extrinsic curvature of the three-dimensional spatial slices $K_{ij} = N^{-1}E_{ij}$.

The ADM action given in Eqn.(2.28) leads to the constraint equations for the Lagrange multipliers N and N^i ,

$$\nabla_i [N^{-1}(E^i_j - \delta^i_j E)] = 0, \quad (2.30)$$

$$R^{(3)} - 2V - N^{-2}(E_{ij}E^{ij} - E^2) - N^{-2}\dot{\phi}^2 = 0 . \quad (2.31)$$

To solve the constraints, we split the shift vector N_i into scalar and vector components

$$N_i \equiv \psi_i + \tilde{N}_i, \quad \text{where} \quad \tilde{N}_{i,i} = 0, \quad (2.32)$$

and define the lapse perturbation as

$$N \equiv 1 + \alpha . \quad (2.33)$$

The quantities α , ψ and \tilde{N}_i then admit expansions in powers of ζ ,

$$\begin{aligned}\alpha &= \alpha_1 + \alpha_2 + \dots, \\ \psi &= \psi_1 + \psi_2 + \dots, \\ \tilde{N}_i &= \tilde{N}_i^{(1)} + \tilde{N}_i^{(2)} + \dots,\end{aligned}\tag{2.34}$$

With an appropriate choice of boundary conditions one may set $\tilde{N}_i^{(1)} \equiv 0$. At first order (2.31) implies

$$\alpha_1 = \frac{\dot{\zeta}}{H}, \quad \partial^2 \tilde{N}_i^{(1)} = 0.\tag{2.35}$$

Similarly at first order Eqn. (2.30) implies,

$$\psi_1 = -\frac{\zeta}{H} + \frac{a^2}{H}\epsilon \partial^{-2}\dot{\zeta},\tag{2.36}$$

Solving these constraints and plugging the first-order solutions for N and N_i into the ADM action, we get the second-order action in ζ

$$S_\zeta = \frac{1}{2} \int d^4x a^3 \frac{\dot{\phi}^2}{H^2} [\dot{\zeta}^2 - a^{-2}(\partial_i \zeta)^2].\tag{2.37}$$

This can be written as,

$$S_\zeta = \int d\tau \int d^3\vec{x} a^3 \left(\frac{\dot{v}^2}{2} - \frac{(\nabla_x v)^2}{2a^2} \right)\tag{2.38}$$

where \vec{x} is a comoving coordinate and $v = \sqrt{2M_{Pl}^2 \epsilon \zeta^2}$ is the *Mukhanov variable*. Here ϵ is the slow-roll parameter. ϵ appears in the definition of v because of the $\dot{\phi}$ term in Eqn.2.37 and through Eqn.2.13. Note that if ϕ is constant (i.e. $\epsilon = 0$), then even large perturbations in ζ would have no effect on the action; the definition of the canonically normalized variables thus needs to contain ϵ for the generation of perturbations. As we shall see later, the magnitude of ϵ determines the relative enhancement of scalars with respect to tensors.

Fourier transforming the spatial part of v we have,

$$S_\zeta = \sum_k \int d\tau a^3 \left(\frac{|\dot{v}_k|^2}{2} - \left(\frac{k}{a}\right)^2 \frac{|v_k|^2}{2} \right)\tag{2.39}$$

which is similar to the action for a collection of uncoupled oscillators. The equation of motion for each Fourier mode is the same as the equation of motion for a simple harmonic oscillator with a time-dependent frequency and a friction term,

$$\ddot{v}_k + 3H\dot{v}_k + (k/a)^2 v_k = 0\tag{2.40}$$

This is the *Mukhanov-Sasaki* equation. So far our discussion has been completely classical. Inflation however takes *quantum fluctuations* and transforms them into classical perturbations. We shall briefly describe how this quantization works and how it relates to classical observables.

We begin by quantizing the field v in analogy with the a quantum harmonic oscillator. The quantum operators corresponding to v and it's conjugate momentum v' are defined as,

$$v \rightarrow \hat{v} = \int \frac{d\mathbf{k}^3}{(2\pi)^3} \left[v_k(\tau) \hat{a}_{\mathbf{k}} e^{i\mathbf{k}\cdot\mathbf{x}} + v_k^*(\tau) \hat{a}_{\mathbf{k}}^\dagger e^{-i\mathbf{k}\cdot\mathbf{x}} \right]. \quad (2.41)$$

The Fourier modes $v_{\mathbf{k}}$ can be written as,

$$v_{\mathbf{k}} \rightarrow \hat{v}_{\mathbf{k}} = v_k(\tau) \hat{a}_{\mathbf{k}} + v_{-k}^*(\tau) \hat{a}_{-\mathbf{k}}^\dagger, \quad (2.42)$$

where $\hat{a}_{-\mathbf{k}}^\dagger$ and $\hat{a}_{\mathbf{k}}$ are the creation and annihilation operators. They satisfy the canonical commutation relation

$$[\hat{a}_{\mathbf{k}}, \hat{a}_{\mathbf{k}'}^\dagger] = (2\pi)^3 \delta(\mathbf{k} - \mathbf{k}'), \quad (2.43)$$

if the mode functions are normalized as follows

$$\langle v_k, v_k \rangle \equiv \frac{i}{\hbar} (v_k^* v_k' - v_k'^* v_k) = 1. \quad (2.44)$$

This normalization provides one of the boundary conditions on the solutions of Eqn. (2.40). The second boundary condition comes from a choice of vacuum. The vacuum state for the fluctuations is defined by,

$$\hat{a}_{\mathbf{k}} |0\rangle = 0, \quad (2.45)$$

In the de-Sitter limit, the vacuum state is given by the Bunch-Davies mode functions

$$v_k = \frac{e^{-ik\tau}}{\sqrt{2k}} \left(1 - \frac{i}{k\tau} \right). \quad (2.46)$$

The two boundary conditions (2.44) and (2.46) are sufficient to fix the mode functions.

We define a field,

$$\hat{\psi}_{\mathbf{k}} \equiv a^{-1} \hat{v}_{\mathbf{k}} \quad (2.47)$$

and compute the corresponding power spectrum of the field

$$\langle \hat{\psi}_{\mathbf{k}}(\tau) \hat{\psi}_{\mathbf{k}'}(\tau) \rangle = (2\pi)^3 \delta(\mathbf{k} + \mathbf{k}') \frac{H^2}{2k^3} (1 + k^2 \tau^2). \quad (2.48)$$

On superhorizon scales, $|k\tau| \ll 1$ we get,

$$\langle \hat{\psi}_{\mathbf{k}}(\tau) \hat{\psi}_{\mathbf{k}'}(\tau) \rangle \rightarrow (2\pi)^3 \delta(\mathbf{k} + \mathbf{k}') \frac{H^2}{2k^3}. \quad (2.49)$$

Using Eqn. (2.49), we can compute the power spectrum of $\zeta = \frac{H}{\dot{\phi}}\psi$ at horizon crossing,

$$a(t_\star)H(t_\star) = k, \quad (2.50)$$

The power spectrum of the curvature perturbations can be defined by,

$$\langle \zeta_{\mathbf{k}}(t) \zeta_{\mathbf{k}'}(t) \rangle = (2\pi)^3 \delta(\mathbf{k} + \mathbf{k}') \frac{1}{2k^3} \frac{H_\star^4}{\dot{\phi}_\star^2}. \quad (2.51)$$

where \star indicates that a quantity is calculated at horizon crossing. Defining the dimensionless power spectrum $\Delta_\zeta^2(k)$ by,

$$\langle \zeta_{\mathbf{k}} \zeta_{\mathbf{k}'} \rangle = (2\pi)^3 \delta(\mathbf{k} + \mathbf{k}') P_\zeta(k), \quad \Delta_\zeta^2(k) \equiv \frac{k^3}{2\pi^2} P_\zeta(k), \quad (2.52)$$

we get

$$\Delta_\zeta^2(k) = \frac{1}{(2\pi)^2} \frac{H_\star^4}{\dot{\phi}_\star^2}. \quad (2.53)$$

Since ζ is constant on super-horizon scales the spectrum at horizon exit determines the power spectrum until a given fluctuation mode re-enters the horizon.

Evaluating the power spectrum at the specific instant of horizon exit extends the result for pure de Sitter background to the slow-roll, quasi-de Sitter space. In that case different modes exit the horizon at slightly different times since $a_\star H_\star$ has a different value. This procedure leads to the appropriate result for the power spectrum during slow-roll inflation. Note that during slow-roll expansion the time-evolution is given by,

$$aH = -\frac{1}{\tau}(1 + \epsilon) \quad (2.54)$$

while for pure de Sitter expansion the scale factor is Hubble rate H is related to t via $a(t) \propto e^{Ht}$ or $a = -(H\tau)^{-1}$.

Thus inflation converts subhorizon quantum fluctuations to classical superhorizon perturbations. After inflation ends, the superhorizon fluctuations *re-enter* the horizon (see Figure 2.4) and become the density fluctuations we see in the CMB and LSS.

The primordial curvature perturbation is a realization of a random field in which each Fourier amplitude ζ_k drawn from a Gaussian distribution with variance $\langle |\zeta_k|^2 \rangle =$

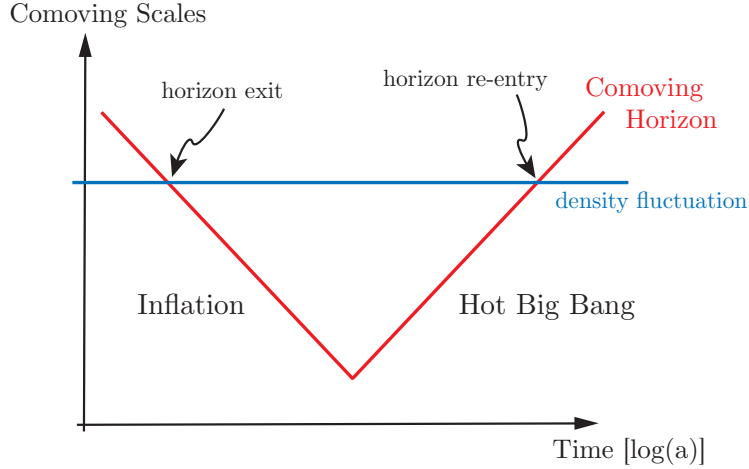


Figure 2.4: All scales that are relevant to cosmological observations today were larger than the Hubble radius until $a \sim 10^{-5}$. However, at sufficiently early times, these scales were smaller than the Hubble radius and therefore causally connected. Figure adopted from Baumann 2009.

$H^2/(4M_{Pl}^2\epsilon k^3)$. The curvature power spectrum can be written in terms of the Planck mass M_{Pl} as,

$$\Delta_\zeta^2(k) = \frac{H^2}{8\pi^2 M_{Pl}^2 \epsilon} \quad (2.55)$$

Planck measurements constrain $\Delta_\zeta^2(k) \approx 2.2 \times 10^{-9}$.

Tensor Perturbations

Gravitational waves are solutions of the sourceless Einstein's equations. Consider an FRW universe with a metric,

$$g_{ij} = a^2(t)(\delta_{ij} + 2h_{ij}) \quad (2.56)$$

The Einstein-Hilbert action for this metric expanded to quadratic order in h_{ij} ,

$$S_h = \frac{1}{4} \int dt \int d^3\vec{x} a^3 M_{Pl}^2 \left(\dot{h}_{ij}^2 - \frac{\partial_k h_{ij}^2}{2a^2} \right) \quad (2.57)$$

Fourier transforming and summing over two GW polarizations gives,

$$S_h = \sum_{p=+, \times} \sum_k \int dt a^3 \left(\frac{|\dot{v}_{p,k}|^2}{2} - \left(\frac{k}{a}\right)^2 \frac{|v_{p,k}|^2}{2} \right) \quad (2.58)$$

where $v_p = (h_p M_{Pl})/2$. As in the case of scalars, each Fourier mode and each polarization behaves like a simple harmonic oscillator. Using arguments similar to

the one used for scalars we can show that the gravitational wave power spectrum, after summing over the two polarizations is given by,

$$\Delta_h^2(k) \equiv 2 \frac{k^3}{2\pi^2} \langle |h_{p,k}|^2 \rangle = \frac{2H^2}{\pi^2 M_{pl}^2} \quad (2.59)$$

Since $H^2 \propto V$ during inflation, the tensor amplitude is determined by the energy density of the Universe during inflation. The tensor amplitude is described using the tensor-to-scalar ratio r ,

$$r \equiv \frac{\Delta_h^2}{\Delta_\zeta^2} = 16\epsilon \approx 0.1 \left(\frac{1}{(2 \times 10^{16} \text{GeV})^4} \right) \quad (2.60)$$

The strongest bounds on r come from the joint analysis of Planck, which puts upper limits on $r < 0.07$ (BICEP2 Collaboration et al. 2016).

2.3 Experimental Tests of Inflation

In the previous section we discussed the generation of power spectra associated with the curvature ζ and tensor h fluctuations generated during inflation. We showed that the power spectra depend on the physics of inflation- specifically the inflaton potential. In this section we provide a short overview of how the power spectra $P_\zeta(k)$ and $P_h(k)$ are associated with observables related to the CMB. The CMB polarization is one of the most promising probes of inflation and this section outlines the kind of calculation that goes into translating inflationary physics to observables. We shall not discuss other proposed techniques to detect inflationary gravitational waves using large scale structure (for instance, see Smith et al. 2006 for a discussion on direct detection of GWs from inflation). Later in this thesis, we provide a novel way to detect inflationary gravitational waves using the circular polarization of the 21cm line.

Inflation can be thought of as a *shrinking Hubble horizon*, which implies that during inflation fluctuations exit the horizon. At late stages, and at lower-energies, these fluctuations re-enter the horizon and we can probe them using observables like the CMB anisotropy. This is possible because perturbations that exit the horizon during inflation remain "frozen" and hence encapsulate information about $P_\zeta(k)$ and $P_h(k)$. Figure 2.4 adapted from Baumann shows how a given comoving wavenumber exits the horizon and then re-enters right before recombination. Once the curvature perturbations ζ re-enter the horizon, they lead to density fluctuations in the matter distribution. These density fluctuations eventually get imprinted on the CMB which we can detect using experiments like Planck.

CMB Temperature Anisotropies

We now discuss the evolution of perturbations *after* the modes re-enter the horizon and eventually become the anisotropies we observe in the CMB. In this section we outline the essential machinery needed to translate the primordial fluctuations to the observed CMB spectrum.

After entering the horizon, the curvature perturbations lead to density fluctuations in the primordial plasma. As the universe cools, the formation of neutral hydrogen leads to the photons decoupling. These photons get redshifted and are observed today as CMB photons. The CMB anisotropies thus contains information about the primordial density perturbations.

The measured CMB temperature fluctuation map on the sky can be expanded in terms of spherical harmonics,

$$\Theta(\hat{n}) \equiv \frac{\delta T(\hat{n})}{T} = \sum_{\ell m} a_{\ell m} Y_{\ell m}(\hat{n}), \quad (2.61)$$

where,

$$a_{\ell m} = \int d\Omega Y_{\ell m}^*(\hat{n}) \Theta(\hat{n}). \quad (2.62)$$

Here, $Y_{\ell m}(\hat{n})$ are the standard spherical harmonics on a 2-sphere. The *statistical isotropy* of the universe allows us to define the angular power spectrum of the CMB in terms of the the multipole moments $a_{\ell m}$ as,

$$C_{\ell}^{TT} = \frac{1}{2\ell + 1} \sum_m \langle a_{\ell m}^* a_{\ell m} \rangle \quad ; \quad \langle a_{\ell m}^* a_{\ell' m'} \rangle = C_{\ell}^{TT} \delta_{\ell\ell'} \delta_{mm'}, \quad (2.63)$$

CMB temperature fluctuations are dominated by the *scalar* modes ζ . The linear evolution which relates ζ and temperature anisotropies is determined by the transfer function $\Delta_{T\ell}(k)$ through the k -space integral

$$a_{\ell m} = 4\pi(-i)^{\ell} \int \frac{d^3k}{(2\pi)^3} \Delta_{T\ell}(k) \zeta_{\mathbf{k}} Y_{\ell m}(\hat{\mathbf{k}}) \quad (2.64)$$

Moreover, we can write down the power spectrum of the curvature fluctuations as,

$$\langle \zeta_{\mathbf{k}} \zeta_{\mathbf{k}'} \rangle = (2\pi)^3 P_{\zeta}(k) \delta(\mathbf{k} + \mathbf{k}'). \quad (2.65)$$

If the primordial fluctuations are Gaussian then $P_{\zeta}(k)$ contains all the information about the primordial fluctuations. In fact, single-field slow-roll inflation predicts that ζ should be Gaussian to a very high degree.

Substituting Eqn.(2.64) & (2.65) into Eqn.(2.63) and using the identity

$$\sum_{m=-\ell}^{\ell} Y_{\ell m}(\hat{\mathbf{k}})Y_{\ell m}(\hat{\mathbf{k}}') = \frac{2\ell + 1}{4\pi} P_{\ell}(\hat{\mathbf{k}} \cdot \hat{\mathbf{k}}'), \quad (2.66)$$

we get

$$C_{\ell}^{TT} = \frac{2}{\pi} \int k^2 dk \underbrace{P_{\zeta}(k)}_{\text{Inflation Transfer Function}} \underbrace{\Delta_{T\ell}^2(k)}_{\text{Inflation Transfer Function}}. \quad (2.67)$$

The transfer function $\Delta_{T\ell}(k)$ depends on the background cosmology parameters and can be computed numerically using Boltzmann-codes such as CAMB. The primordial spectrum $P_{\zeta}(k)$ can be measured by deconvolving C_{ℓ}^{TT} , using a given transfer function, which depends on the background cosmology.

We can observe the fluctuations that were outside the horizon even at recombination by measuring the largest-scale features in C_{ℓ}^{TT} . This is known as the Sachs-Wolfe regime, where the transfer function is simply a geometric projection from recombination to $z = 0$ and is given by a Bessel function,

$$\Delta_{T\ell}(k) = \frac{1}{3} j_{\ell}(k[\tau_0 - \tau_{rec}]). \quad (2.68)$$

We can show that this implies that C_{ℓ}^{TT} at large scales is,

$$\ell(\ell + 1)C_{\ell}^{TT} \propto \ell^{n_s - 1}. \quad (2.69)$$

Thus the measurement of the temperature angular power spectrum of the CMB at the largest scales can be used to constrain n_s , the scalar spectral index. Planck data indicates that $n_s = 0.968 \pm 0.006$ (Planck Collaboration et al. 2016).²

CMB Polarization Anisotropies

Thomson scattering between electrons and photons leads to a polarization of the CMB and this polarization can be used to probe primordial fluctuations, particularly tensor modes. Measurement of the CMB polarization is the primary scientific motivation behind the next generation of CMB experiments (Kamionkowski & Kovetz 2016). In this section we briefly review the physics of CMB polarization and how it relates to tensor modes. Details about the calculation of CMB polarization anisotropies can be found in Dodelson 2003.

²Note that the measurement of n_s by Planck relies on a fit to the whole CMB spectrum- the Sachs-Wolfe plateau at the largest angular scales are included but have large cosmic variance errors. Instead, the constraint comes from the acoustic peaks and the damping tail regions.

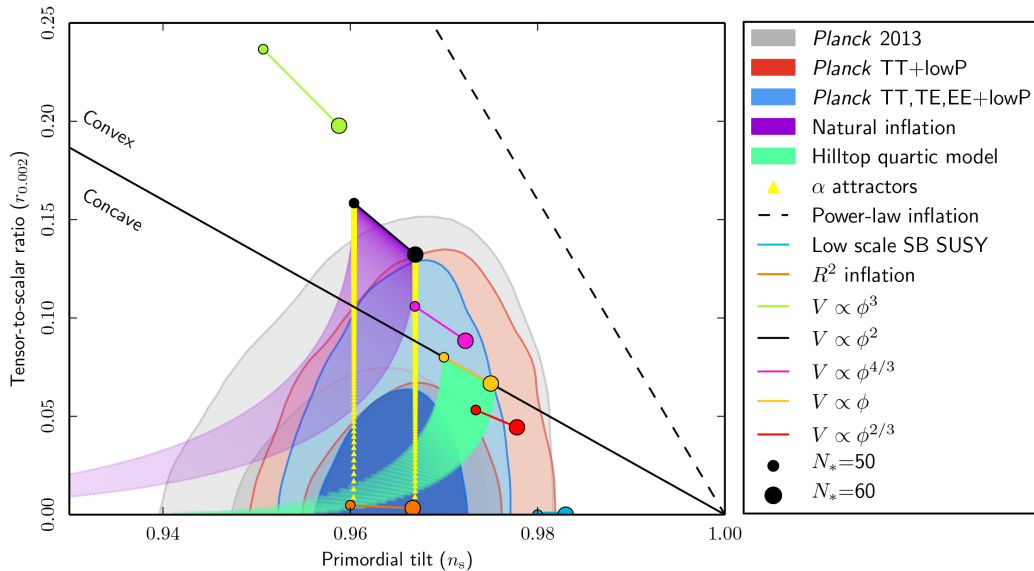


Figure 2.5: Current constraints on the scalar spectral index n_s and tensor-to-scalar ratio r , for a variety of slow-roll inflationary models. Figure adopted from Planck Collaboration et al. 2016.

The CMB is polarized because free electrons during recombination see an anisotropic radiation field sourced by primordial density fluctuations. The linear polarization arises due to the quadrupole of the radiation field incident on an electron (in its rest frame). The CMB polarization thus encodes information about the primordial density (or scalar) fluctuations.

Since polarization is not a scalar field, the standard decomposition in terms of spherical harmonics as discussed in the previous section is no longer applicable. Linear polarization is then described by the Stokes parameters $Q = \frac{1}{4}(I_{11} - I_{22})$ and $U = \frac{1}{2}I_{12}$, where $I_{ij}(\hat{n})$ is the 2×2 intensity tensor. Here \hat{n} denotes the direction on the sky. The components of I_{ij} are defined relative to two orthogonal basis vectors $\hat{\mathbf{e}}_1$ and $\hat{\mathbf{e}}_2$ perpendicular to \hat{n} . The polarization magnitude and angle are $P = \sqrt{Q^2 + U^2}$ and $\alpha = \frac{1}{2} \tan^{-1}(U/Q)$. The temperature anisotropy is given by $T = \frac{1}{4}(I_{11} + I_{22})$ and is invariant under a rotation in the plane perpendicular to \hat{n} . Therefore the temperature field can be expanded in terms of scalar (spin-0) spherical harmonics.

The quantities Q and U , transform under rotation by an angle ψ as a spin-2 field $(Q \pm iU)(\hat{n}) \rightarrow e^{\mp 2i\psi}(Q \pm iU)(\hat{n})$. The harmonic analysis of $Q \pm iU$ therefore requires expansion on the sphere in terms of tensor (spin-2) spherical harmonics

$$(Q \pm iU)(\hat{n}) = \sum_{\ell, m} a_{\pm 2, \ell m \pm 2} Y_{\ell m}(\hat{n}). \quad (2.70)$$

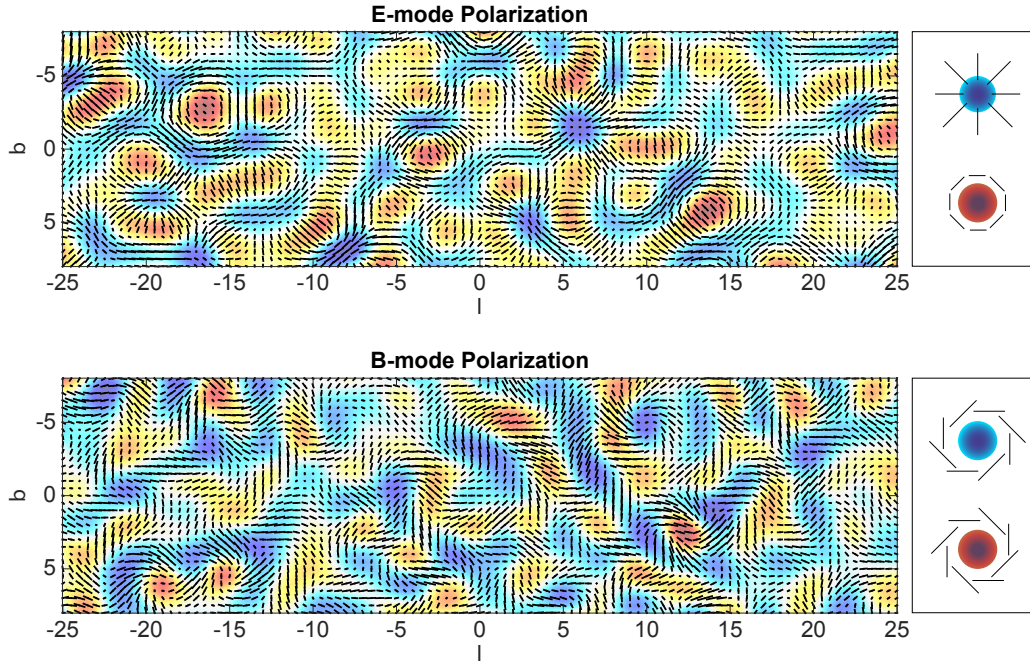


Figure 2.6: The top panel shows a polarization pattern composed only of E modes. The polarization pattern is tangential around hot spots and radial around cold spots. The bottom panel shows a polarization pattern composed only of B modes. The polarization pattern surrounding hot and cold spots of the B mode show a swirling pattern. Note that the E -mode is parity invariant while the B -mode is not. Figure adopted from Kamionkowski & Kovetz 2016.

We now introduce linear combinations of the moments $a_{\pm 2, \ell m}$,

$$a_{E, \ell m} \equiv -\frac{1}{2} (a_{2, \ell m} + a_{-2, \ell m}), \quad a_{B, \ell m} \equiv -\frac{1}{2i} (a_{2, \ell m} - a_{-2, \ell m}). \quad (2.71)$$

This allows us to define two spin-0 fields instead of the spin-2 quantities Q and U

$$E(\hat{n}) = \sum_{\ell, m} a_{E, \ell m} Y_{\ell m}(\hat{n}), \quad B(\hat{n}) = \sum_{\ell, m} a_{B, \ell m} Y_{\ell m}(\hat{n}). \quad (2.72)$$

The scalar quantities E and B completely describe a linear polarization field. E -mode polarization is *curl-free* with polarization vectors pointing radially around cold spots and tangentially around hot spots. B -mode polarization is *divergence-free* but has a *curl*: the polarization vectors have a net vorticity around any given point on the sky (see Fig. 2.6).

The symmetries of temperature and polarization anisotropies allow four types of correlations: C_ℓ^{TT} , C_ℓ^{TE} , C_ℓ^{EE} , and C_ℓ^{BB} . C_ℓ^{TB} and C_ℓ^{EB} are zero due to symmetry

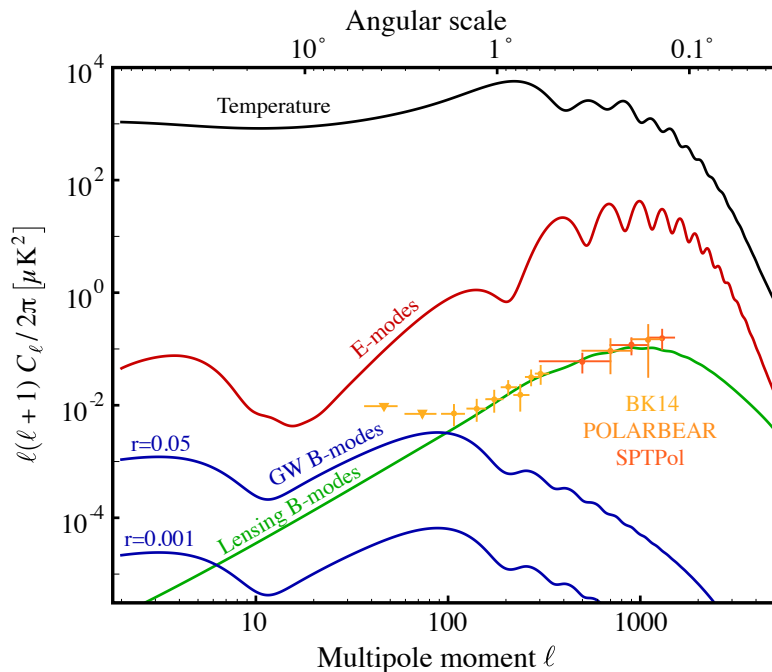


Figure 2.7: Theoretical predictions for the temperature (black), E -mode (red), and tensor B -mode (blue) power spectra. Also shown are expected values lensing B -modes (green). Current measurements of the B -mode for BICEP2/Keck Array (yellow), POLARBEAR (orange), and SPTPol (dark orange). Figure adopted from Abazajian et al. 2016.

arguments. The angular power spectra are defined as,

$$C_\ell^{XY} \equiv \frac{1}{2\ell + 1} \sum_m \langle a_{X,\ell m}^* a_{Y,\ell m} \rangle, \quad X, Y = T, E, B. \quad (2.73)$$

It was pointed out by Seljak & Zaldarriaga 1997 & Kamionkowski et al. 1997 that density perturbations create E -modes but no B -modes. Tensor perturbations, however, create both E -modes and B -modes. Since scalar density perturbations do not produce B -modes while tensor perturbations do, detection of these B -modes will be a smoking-gun evidence for inflation. The theoretical predictions for the B -modes due to tensors and the current observational limits are shown in Figure 2.7.

While density perturbations do not induce a curl in the polarization in *linear theory*, B -modes can be generated at higher order in perturbation theory. The largest non-linear effect that leads to the generation of B -modes in the CMB is gravitational lensing of the high redshift CMB by intervening density perturbations. The B -mode signal due to gravitational lensing was first detected by the SPTPol telescope (Hanson et al. 2013).

2.4 Conclusion

Measurement of the B -modes of the CMB is the most promising strategy to detect inflationary gravitational waves in the immediate term. One of the caveats for the detectability of inflationary gravitational waves is that their strength (determined by r) depends on the (hitherto unknown) model of inflation. Models of single-field slow-roll (SFSR) inflation predict a range of values of r , from order unity to very low values. While models that predict r of order unity are already ruled out by observations, power-law inflationary potentials that predict r of the order of $1 - n_s$ are the most interesting to immediate term CMB experiments. On the other hand, Higgs-like potentials can lead to $r \sim 0.001$ which can be probed by the next generation of CMB experiments. SFSR models with very flat potentials, where inflation ends when the inflation falls off a cliff (for example, the second panel in Fig.2.3), can lead to very low values of r and these are not likely to be detected even with the next generation CMB experiments.

While there is no broad consensus on “natural” models of inflation, given the measurements of the scalar spectral index n_s , SFSR models with power-law potentials that predict values of $r \sim 0.01$ can potentially be detected by ground-based CMB experiments over the next decade. Note that the measurement of r will enable us to directly measure the energy scale of inflation $V_{inf}^{1/4} \sim 10^{-3}(r/0.01)^{1/4}M_{Pl}$, where M_{Pl} is the Planck mass.

The current upper bounds on r from the combination of the CMB B -mode and other observables are $r < 0.07$ (95% CL) (BICEP2 Collaboration et al. 2016). The measurement of the scalar spectral index n_s by Planck rules out very low values of r ($r < 10^{-4}$) for many of the simplest models, although model dependency implies one could get lower values of r in special cases (see Kamionkowski & Kovetz 2016 for a discussion on inflationary models that predict low values of r). Measuring B -modes at the $r > 0.002$ level is the goal of future CMB “Stage-IV” experiments (Abazajian et al. 2016). However, for low values of r CMB B -mode experiments need to confront challenging Galactic foregrounds and the contaminating lensing signal. In the event of a detection it will be crucial to verify the result using techniques that have independent systematics.

There have been other techniques proposed to measure r using large-scale structure observables (Dodelson et al. 2003; Alizadeh & Hirata 2012; Schmidt & Jeong 2012; Schmidt et al. 2014; Chisari et al. 2014), although the surveys required even to detect $r \sim 0.07$ are rather futuristic. Direct detection of the gravitational waves

at high-frequencies with a network of space-based laser interferometers has also been proposed (Corbin & Cornish 2006; Kawamura et al. 2011). In Chapter 4 we propose a new technique to detect inflationary gravitational waves using the circular polarization of the 21 cm line. This technique, while futuristic, has the potential to probe $r \sim 10^{-5}$ using an array of closely packed dipole antennas with a side length of 1000 km. In the event that near-term CMB B -mode experiments measure a value of r , our technique could potentially be used to verify the detection. In the case that the value of $r < 10^{-3}$, our technique would be a viable way to probe inflationary gravitational waves at low r .

References

- Abazajian, K. N., Adshead, P., Ahmed, Z., et al., 2016, ArXiv e-prints
- Albrecht, A., & Steinhardt, P. J., 1982, Physical Review Letters, 48, 1220
- Alizadeh, E., & Hirata, C. M., 2012, PhRvD, 85.12, 123540, 123540
- Baumann, D., 2009, ArXiv e-prints
- BICEP2 Collaboration, Keck Array Collaboration, Ade, P. A. R., et al., 2016, Physical Review Letters, 116.3, 031302, 031302
- Chisari, N. E., Dvorkin, C., & Schmidt, F., 2014, PhRvD, 90.4, 043527, 043527
- Corbin, V., & Cornish, N. J., 2006, Classical and Quantum Gravity, 23, 2435
- Dodelson, S. 2003, Modern cosmology
- Dodelson, S., Rozo, E., & Stebbins, A., 2003, Physical Review Letters, 91.2, 021301, 021301
- Guth, A. H., 1981, PhRvD, 23, 347
- Guth, A. H., & Pi, S.-Y., 1982, Physical Review Letters, 49, 1110
- Hanson, D., Hoover, S., Crites, A., et al., 2013, Physical Review Letters, 111.14, 141301, 141301
- Hawking, S. W., 1982, Physics Letters B, 115, 295
- Kamionkowski, M., Kosowsky, A., & Stebbins, A., 1997, Physical Review Letters, 78, 2058
- Kamionkowski, M., & Kovetz, E. D., 2016, ARA&A, 54, 227
- Kawamura, S., Ando, M., Seto, N., et al., 2011, Classical and Quantum Gravity, 28.9, 094011, 094011
- Linde, A. D., 1982, Physics Letters B, 108, 389
- Penzias, A. A., & Wilson, R. W., 1965, ApJ, 142, 419

Planck Collaboration, Ade, P. A. R., Aghanim, N., et al., 2016, *A&A*, 594, A20, A20

Rubakov, V. A., Sazhin, M. V., & Veryaskin, A. V., 1982, *Physics Letters B*, 115, 189

Schmidt, F., & Jeong, D., 2012, *PhRvD*, 86.8, 083513, 083513

Schmidt, F., Pajer, E., & Zaldarriaga, M., 2014, *PhRvD*, 89.8, 083507, 083507

Seljak, U., & Zaldarriaga, M., 1997, *Physical Review Letters*, 78, 2054

Smith, T. L., Kamionkowski, M., & Cooray, A., 2006, *PhRvD*, 73.2, 023504, 023504

Chapter 3

OVERVIEW OF 21CM COSMOLOGY

The distribution of matter approximately 400,000 years after the Big Bang has been exquisitely measured using the statistics of the CMB. The first stars and galaxies formed within the first billion years of the universe and led to the formation of the complex cosmic web that has been probed by galaxy surveys over the past two decade. However, both the CMB and galaxy surveys map out a small fraction of the universe's comoving volume. As seen in Figure. 3.1, a large volume of the universe remains unexplored by current cosmological probes.

The epoch of the universe after recombination and before the first galaxies formed is often referred to as the Cosmic Dark Ages, since the universe was mostly neutral and gravity was the dominant force governing the evolution. Probing the Dark Ages will provide access to a large number of modes in the matter distribution of the universe, allowing us to put stringent constraints on cosmological parameters. It will also allow us to understand the phase transition of the universe from an almost neutral state to a completely ionized state, due to the first stars and galaxies.

The efforts to probe the dark ages rely on the observation of low-frequency radio emission from the hyperfine transition of neutral hydrogen. The interaction between the proton and electron spins in neutral hydrogen leads to a splitting of the ground state of neutral hydrogen. Transition between these hyperfine states leads to the emission of a photon with a wavelength of about 21cm. The emitted 21cm photon is then redshifted due to the expansion of the universe. For a given model of the expansion of the universe we can thus observe different redshifts or distances by tuning the frequency. Using multi-frequency radio experiments, we can thus construct 3D, tomographic maps of the universe during the dark ages.

In this chapter I review the basic physics of the 21cm signal and the statistical tools useful for measuring the signal. I also discuss the essentials of low-frequency interferometers, which are used to detect the 21cm signal. Details about 21cm cosmology and observations can be found in reviews by Furlanetto et al. 2006 and Pritchard & Loeb 2012.

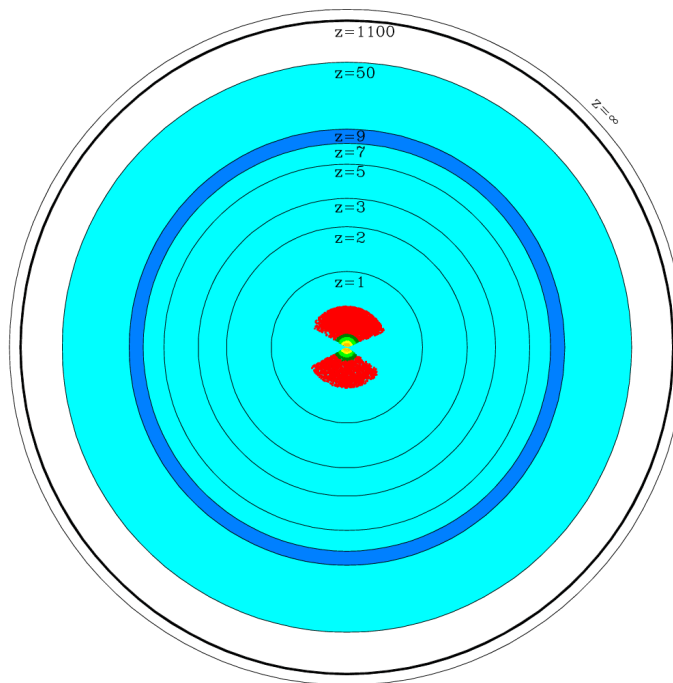


Figure 3.1: 21 cm observations can potentially map the largest volumes of the observable universe, while the CMB can probe a 2D surface at $z \sim 1100$. and LSS surveys can map small volumes of the local universe. Note that more than half of the comoving volume of the universe lies at $z > 20$. Figure adopted from Tegmark & Zaldarriaga 2009.

3.1 Physics of the 21cm Signal

21cm cosmology is made possible due to a simple radiative process in the early universe: the CMB acts as a backlight for neutral hydrogen atoms in the high-redshift IGM leading to absorption or emission of the 21 cm line. To describe the 21cm signal, we typically use the specific intensity I_ν at a given frequency ν . For low-frequencies we can use the Rayleigh-Jeans limit of the blackbody spectrum to relate I_ν to the brightness temperature T_b via,

$$I_\nu \equiv \frac{2k_b T_b \nu^2}{c^2}. \quad (3.1)$$

The radiative transfer equation for hydrogen atoms at redshift z backlit by the CMB with temperature $T_\gamma(z)$ can then be written as,

$$T_b(\nu) = T_s(1 - \exp[-\tau_\nu]) + T_\gamma(z) \exp[-\tau_\nu]. \quad (3.2)$$

Here τ_ν is the the optical depth of the cloud due to the hyperfine transition and T_s is the spin temperature defined by,

$$\frac{n(F = 1)}{n(F = 0)} = \frac{g_1}{g_0} \exp\left[-\frac{T_*}{T_s}\right] \quad (3.3)$$

, where $F = 0$ denotes the spin-antiparallel hyperfine level, $F = 1$ denotes the spin-parallel level, $g_1 = 3$ and $g_0 = 1$ are the statistical weights and $T_* = \hbar\omega_{hf}/k_B = 68\text{mK}$ is the hyperfine splitting in temperature units. We observe 21cm *emission* if $T_s > T_\gamma$ and absorption if $T_s < T_\gamma$.

The optical depth along a line of sight of a hydrogen cloud is given by,

$$\tau_\nu = \int dl [(1 - \exp(-E_{10}/k_B T_s)] \sigma_0 \phi(\nu) n_0 \quad (3.4)$$

, where $n_0 = n_H/4$, n_H being the hydrogen density and the 21cm cross-section is given by $\sigma(\nu) = \sigma_0 \phi(\nu)$, with $\sigma_0 \equiv 3c^2 A_{10}/8\pi\nu^2$, where A_{10} is the spontaneous decay rate of the spin-flip transition, and the line profile is normalized by,

$$\int \phi(\nu) d\nu = 1 \quad (3.5)$$

To evaluate the optical depth we need to determine the path length as a function of frequency $l(\nu)$ which determines the range of frequencies $d\nu$ over the path dl that corresponds to a given observed frequency ν_{obs} . This is done using the Sobolev approximation that assumes a linear velocity profile locally $\nu = (d\nu/dl)l$ and then using the Doppler shifted frequency $\nu_{\text{obs}} = \nu_{\text{em}}(1 - \nu/c)$.

The spin temperature depends on three processes:

- Absorption or stimulated emission of CMB photons near the 21cm transition. This leads to a coupling between T_s and T_γ
- Collisional excitation and de-excitation of hydrogen atoms. These include hydrogen-hydrogen collisions, hydrogen-electron collisions, and hydrogen-proton collisions. This leads to a coupling between T_s and the kinetic gas temperature T_k
- Resonant scattering of Lyman- α photons from the first stars, which can change the spin state via the Wouthuysen-Field effect This leads to a coupling between T_s and $T_{\text{Ly}\alpha}$.

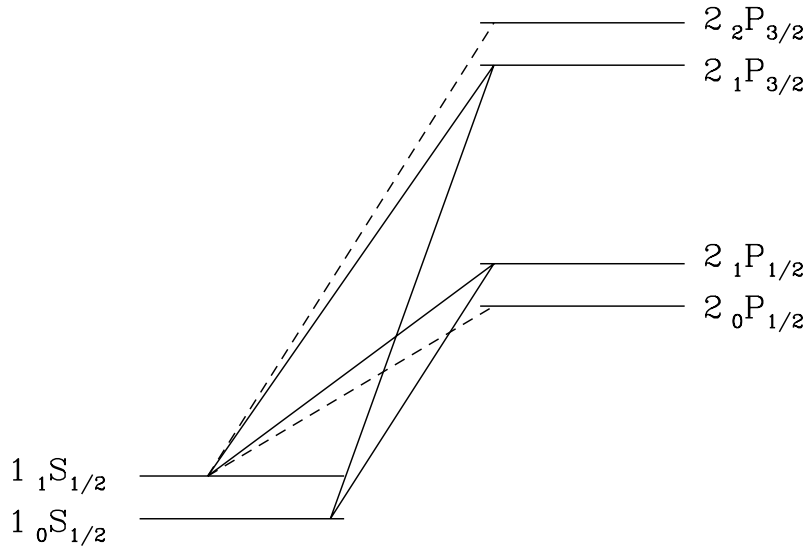


Figure 3.2: The transitions relevant for the Wouthuysen-Field effect. Solid line transitions contribute to spin flips. Transitions denoted by dashed lines are allowed but do not contribute to spin flips. Figure adopted from Pritchard & Loeb 2012.

The Wouthuysen-Field effect is illustrated in Figure 3.2. The figure shows the hyperfine $1S$ and $2P$ levels of hydrogen. If the hydrogen is initially in the hyperfine singlet state, the absorption of a $\text{Ly}\alpha$ photon will excite it to either of the central $2P$ hyperfine states. The other two hyperfine states are inaccessible due to selection rules. The subsequent emission of a $\text{Ly}\alpha$ photon can bring the atom back to either of the two ground state hyperfine levels. In the case when the atom transitions to the triplet state, a spin-flip takes place. Thus resonant scattering of $\text{Ly}\alpha$ photons can lead to a spin flip.

The Wouthuysen-Field effect couples the spin temperature T_s to the color temperature $T_{\text{Ly}\alpha}$ of the radiation field. $T_{\text{Ly}\alpha}$ is a measure of the shape of the radiation field as a function of frequency around the $\text{Ly}\alpha$ line and is defined as $h/k_B T_{\text{Ly}\alpha} = -d \log n_\nu / d\nu$, where n_ν is the photon occupation number. In the cases we are interested in the optical depth to $\text{Ly}\alpha$ scattering is very large and leads to a large number of scatterings of $\text{Ly}\alpha$ photons that bring the radiation field and the gas

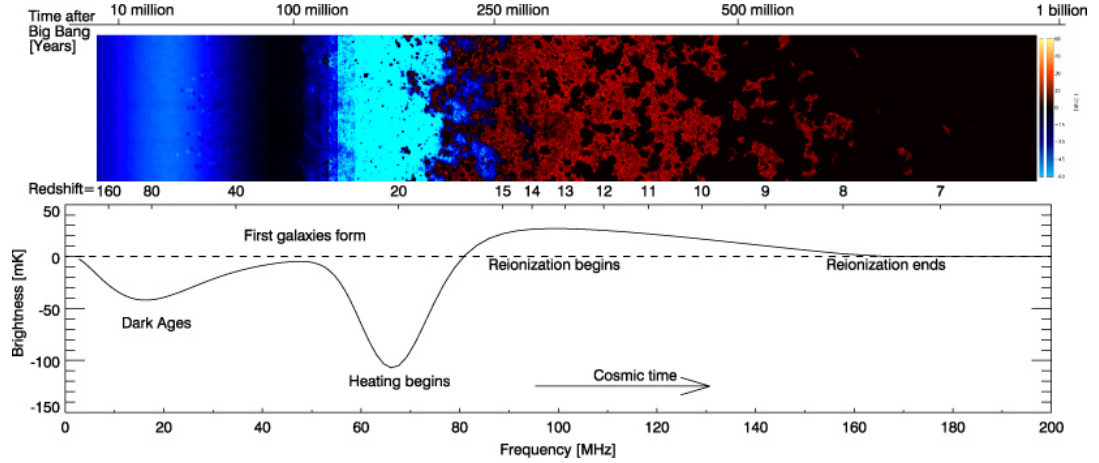


Figure 3.3: The evolution of the 21 cm global signal depends on different physical processes at different epochs. The evolution of the brightness temperature T_b leads to the 21cm signal appear either in absorption or in emission against the CMB. The top panel shows a slice through a simulation showing the evolution of T_b and the heating due to the first generation stars and galaxies. The bottom panel shows the sky-averaged global 21 cm signal, which largely traces the evolution of the spin temperature and neutral fraction of hydrogen. Figure adopted from Pritchard & Loeb 2012.

into local equilibrium, for frequencies near the line center. This leads to $T_{\text{Ly}\alpha} \approx T_k$.

In equilibrium, the spin temperature is given by,

$$T_s^{-1} = \frac{T_\gamma^{-1} + x_c T_K^{-1} + x_\alpha T_\alpha^{-1}}{1 + x_c + x_\alpha}, \quad (3.6)$$

where x_c is the collisional coupling coefficient and x_α is the Lyman- α coupling coefficient. Note that these are not fundamental parameters but instead depend on cross-sections as well as macro-physics parameters like gas density and Ly α intensity

Observationally, we are interested in the brightness temperature of the 21cm line. Quantum mechanically, the 21 cm transition is a forbidden transition, with a lifetime for spontaneous emission of $\sim 3 \times 10^7$ years. Therefore τ_ν is small and we can work in the optically thin regime. The brightness temperature fluctuation relative to the CMB at redshift z in the optically thin limit is given by

$$\delta T_b(\hat{r}, \nu) \approx 27 x_H \left(\frac{T_s - T_\gamma}{T_s} \right) \left(\frac{1+z}{10} \right)^{1/2} (1 + \delta_b)(1 + \delta_x) \frac{(1+z)H(z)}{\partial_{||} v_{||}} \text{mK}, \quad (3.7)$$

where \hat{r} is unit direction vector, x_H is the mean neutral hydrogen fraction, $v_{||}$ is the velocity along the line-of-sight direction, δ_b is the fractional baryon overdensity, and δ_x is the neutral fraction overdensity. The variation of these parameters across space and along redshift leads to a rich 3D field of the 21cm brightness temperature. The statistics of this brightness temperature field encapsulate both fundamental cosmological parameters as well as astrophysics during the Dark Ages.

3.2 Evolution of the 21cm Signal

The evolution of the brightness temperature T_b across frequency, and hence across redshift, depends on both cosmological parameters (eg: the matter power spectrum), as well as more complex astrophysical qualities (e.g., the Lyman- α flux), as evident from Eqn 3.7. The evolution of the spatially averaged, "global" 21cm signal is shown in Figure 3.3 (adapted from Pritchard & Loeb 2012). Future 21cm experiments will thus need to construct high-resolution maps of T_b across multiple redshifts.

Meaningful cosmological information from the maps can only be extracted statistically. The quantity of interest is the power spectrum of the brightness temperature field, defined as,

$$\langle \hat{T}_b^*(\mathbf{k}) \hat{T}_b(\mathbf{k}') \rangle = (2\pi)^3 \delta(\mathbf{k} - \mathbf{k}') P_T(k), \quad (3.8)$$

where \hat{T}_b is the 3D spatial Fourier transform of the T_b field. The angle brackets denote an ensemble average and $\delta(\mathbf{k} - \mathbf{k}')$ is the Dirac delta function. For a statistically isotropic 21cm signal, $P(\mathbf{k})$ is the same as $P(k)$. We also define,

$$\Delta_{21}^2(k) = \frac{k^3}{2\pi^2} P(k), \quad (3.9)$$

which measures the contribution to the root-mean-square fluctuations in T_b per logarithmic bin in k . We plot different theoretical models of $\Delta_{21}^2(k)$ corresponding to different ionization fractions of the IGM in Figure. 3.4.

The power spectrum of the brightness temperature is a redshift dependent quantity. Here we summarize the different regimes and the key physical processes at play:

- **High Redshifts ($40 < z < 200$):** Compton scattering of the residual free electrons after recombination leads to thermal coupling of the gas to the CMB at $z > 200$, and this leads to a tight coupling between T_γ , T_k and T_s and they are effectively the same. This leads to no net absorption or emission of 21cm photons and the brightness temperature is zero. It is only around $z \sim 200$, when this coupling is broken that 21cm cosmology becomes possible.

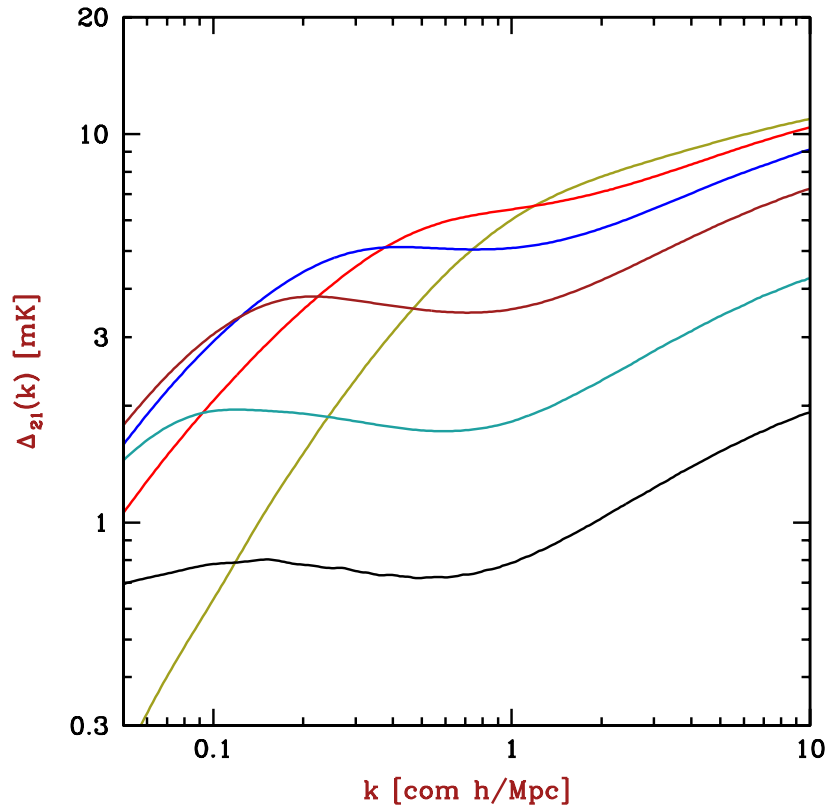


Figure 3.4: The evolution of the 21 cm power spectrum as a function of the ionized fraction is expected to reveal the astrophysical processes that drove reionization and the nature of the first stars and galaxies. The right side of the y-axis shows neutral fraction of the universe. As the universe goes from almost neutral (yellow) to ionized (gray), the overall amplitude of the power spectrum decreases. Moreover, as reionization proceeds the high- k power decreases since reionization bubbles start forming at small scales and then grow to larger scales.

After $z \sim 200$, the gas begins to cool adiabatically: $T_k \propto (1+z)^2$ while the CMB temperature $T_\gamma \propto (1+z)$. This sets $T_\gamma > T_s$ and the signal appears in absorption until $z \sim 40$ when collisional coupling stops becoming effective. During this period the 21cm fluctuations are sourced purely by the dark matter distribution and measurement of the 21cm power spectrum during this epoch can enable us to probe the matter power spectrum with exquisite precision.

- **Intermediate Redshifts ($6 < z < 40$):** At intermediate redshifts the first luminous objects in the universe form and the IGM transitions from being mostly neutral to mostly ionized. The UV photons interact with the IGM in two ways: photons with $E > 13.6$ eV are ionizing and lead to coupling of the T_k with

the ionizing sources. These UV photons have a very short mean free path in the neutral medium and lead to ionized HII regions with a sharp boundary. Photons with $10.2 < E < 13.6$ eV redshift until they enter a Lyman series resonance and subsequently generate Ly α photons via atomic cascades. The Ly α photons couple to T_s via the Wouthuysen-Field effect.

Since the neutral fraction in the universe is still high, T_α is almost equal to T_k , leading to a second dip in the global signal and the 21 cm signal becoming visible in absorption. The heating of the IGM due to the first x-ray sources leads to T_k becoming more than T_γ , which leads to 21cm emission from certain parts of the IGM. The spatial structure of the 21cm field is thus far more complex during this epoch and depends on the Lyman- α field, the distribution of x-ray sources and the background evolution of dark matter. Note that the scattering of Ly α photons off hydrogen atoms is rather inefficient in heating the gas- the spectral distortion of the Ly α photons during scattering greatly reduces the heating rate. Hence Ly α heating requires very large Ly α fluxes and is likely to be more efficient at later times. On the other hand X-ray heating of the gas is likely to be very efficient during this epoch. X-ray photons have a very long mean free path, and hence are able to heat the gas at greater distances from the source,. Moreover, X-rays can be produced in large quantities once the first compact objects are formed. X-rays heat the gas primarily through photo-ionization. Heating happens via energetic photo-electrons generated due to photo-ionization that dissipate their energy through heating the gas.

Around $z \sim 10$ ultraviolet photons from the first generation of high-mass stars start "re-ionizing" the universe. This leads to growing "bubbles" of ionized material, centered on the most luminous objects, that eventually grow in size and coalesce. During reionization the power shifts from high-k scales to low-k scales since the ionized fraction is low at large scales, leading to a higher 21cm signal (there is no 21cm signal from the ionized bubbles). Studying the power spectrum as a function of redshift can thus allow us to constrain the process of reionization and understand the first luminous sources

- **Low Redshifts ($z < 6$):** While the universe is almost completely ionized at low redshifts, there are pockets of neutral hydrogen trapped in galaxies due to self-shielding. Aggregated over a number of galaxies this can lead to a 21cm signal at low-redshifts. The unresolved 21cm signal from the galaxies

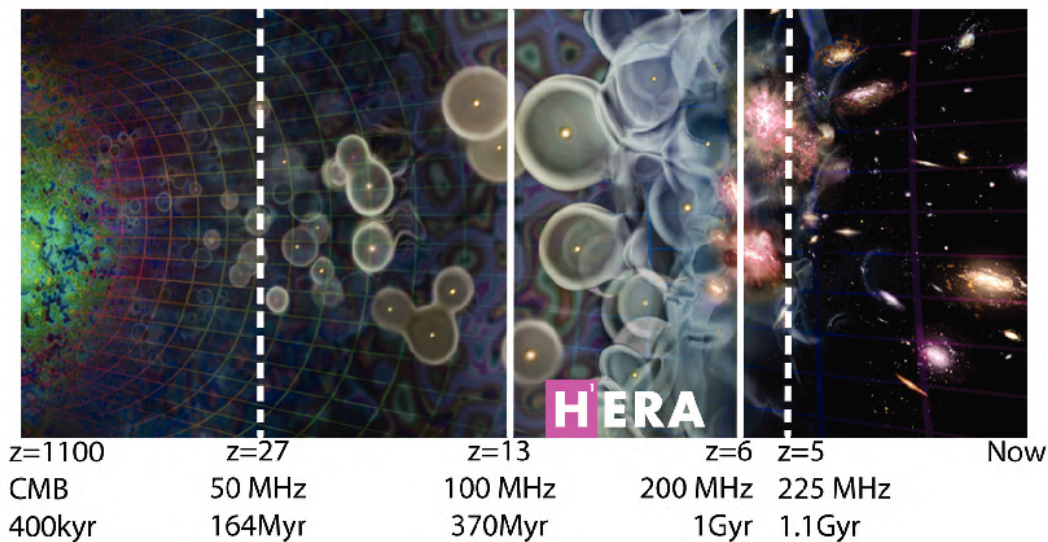


Figure 3.5: The evolution of the universe from the CMB (extreme left) to the current day (extreme right). After the CMB the universe goes through the Dark Ages when it is largely neutral. As the first stars and galaxies light up, the universe gets reionized. Reionization is inhomogeneous and fills the the universe with merging bubbles of ionized hydrogen. Image credit: HERA/Avi Loeb/SciAm

is thus similar to a low-resolution galaxy survey and can be used as a low- z cosmological probe via the measurement Baryon Acoustic Oscillations (BAO). As with galaxy surveys, these measurements need careful modeling of the bias. The intensity mapping of the 21cm line however, has many advantages over traditional galaxy surveys. The large instantaneous field of view enables faster survey speeds, the telescopes are comparatively cheap and the redshift resolution can be very high since it is determined digitally. The key challenge for 21 cm intensity mapping experiments are astrophysical foregrounds which are many orders of magnitude larger than the cosmological signal. However, the dominant foregrounds (galactic and extragalactic synchrotron and free-free emission) are spectrally smooth and can in principle be removed using their spectral information. Chromatic instrument response can introduce foreground component that is not spectrally smooth; however, this spectrally

un-smooth component is confined to a “foreground wedge” at low k_{\parallel} and k_{\perp} . Seo & Hirata 2016 showed that this wedge effect can be very detrimental to determination of the angular diameter distance at $z \sim 1 - 2$. Calibration techniques that remove the foreground wedge will thus be critical for using the BAO feature in 21cm intensity mapping surveys as a cosmological probe.

3.3 Low Frequency Radio Interferometers: Basics

While the detection and characterization of the 21cm signal holds great scientific promise, the measurements are exceedingly challenging. There are a number of low-frequency radio interferometers that are currently online or are under-construction whose primary scientific goal is to measure the 21cm power spectrum from the Epoch of Reionization (EoR) and the Dark Ages. In this section we review the basics of low-frequency radio interferometers. We set up our notation and review definitions of quantities describing sensitivity of interferometric radio arrays; we then focus on the derivation of the noise power spectrum that will be relevant to our calculations in Chapter IV. The discussion in this section is based on Gluscevic et al. 2017, in which I contributed to the calculation of the noise power spectrum.

Definitions

The redshifted 21–cm signal can be represented with specific intensity at a location in physical space $I(\vec{r})$ or in Fourier space $\tilde{I}(\vec{k})$. If θ_x and θ_y are the angular offset from a reference point in the field of observation, and θ_v is an offset in the frequency (radial) direction from a chosen reference frequency, these functions become $\mathcal{I}(\theta_x, \theta_y, \theta_v)$ and $\tilde{\mathcal{I}}(u, v, \eta)$, respectively. Here, vector \vec{k} (in the units of comoving Mpc^{-1}) is a Fourier dual of \vec{r} (comoving Mpc), and likewise, θ_x (rad), θ_y (rad), and θ_v (Hz) are duals of the coordinates u (rad^{-1}), v (rad^{-1}), and η (seconds), respectively. Notice that θ_x and θ_y represent the angular extent of the patch in the sky, while θ_v represents its extent in frequency space. The two sets of coordinates are related through linear transformations in the following way

$$\begin{aligned} \theta_x &= \frac{r_x}{\chi(z)}, & u &= \frac{k_x \chi(z)}{2\pi}, \\ \theta_y &= \frac{r_y}{\chi(z)}, & v &= \frac{k_y \chi(z)}{2\pi}, \\ \theta_v &= \frac{H(z)v_{21}}{c(1+z)^2} r_z, & \eta &= \frac{c(1+z)^2}{2\pi H(z)v_{21}} k_z, \end{aligned} \quad (3.10)$$

where $v_{21} = 1420.4$ MHz is the frequency corresponding to the 21–cm line in the rest frame of the emitting atoms; $H(z)$ is the Hubble parameter; and $\chi(z)$ is the

comoving distance to redshift z which marks the middle of the observed data cube where r_z and θ_ν intervals are evaluated. Note that $2\pi\theta_i u = r_i k_i$, for $i \in \{x, y\}$. The convention we use for the Fourier transform is

$$\begin{aligned} I(\vec{r}) &= \frac{1}{(2\pi)^3} \int \tilde{I}(\vec{k}) e^{i\vec{k}\cdot\vec{r}} d\vec{k}, \\ \tilde{I}(\vec{k}) &= \int I(\vec{r}) e^{-i\vec{k}\cdot\vec{r}} d\vec{r}, \end{aligned} \quad (3.11)$$

where Fourier-space functions are denoted with tilde. Similarly,

$$\begin{aligned} I(\theta_x, \theta_y, \theta_\nu) &= \int \tilde{I}(u, v, \eta) e^{2\pi i(u\theta_x + v\theta_y + \eta\theta_\nu)} du dv d\eta, \\ \tilde{I}(u, v, \eta) &= \int I(\theta_x, \theta_y, \theta_\nu) e^{-2\pi i(u\theta_x + v\theta_y + \eta\theta_\nu)} d\theta_x d\theta_y d\theta_\nu. \end{aligned} \quad (3.12)$$

From Eqs. (3.10)–(3.12), the following relation is satisfied

$$\tilde{I}(\vec{k}) = \frac{c(1+z)^2 \chi(z)^2}{H(z) v_{21}} \tilde{I}(u, v, \eta), \quad (3.13)$$

where the proportionality factor contains the transformation Jacobian $\frac{dr_x dr_y dr_z}{d\theta_x d\theta_y d\theta_\nu}$. Finally, the relationship between the specific intensity in the uv -plane and the visibility function $\mathcal{V}(u, v, \theta_\nu)$ is given by the Fourier transform of the frequency coordinate,

$$\begin{aligned} \mathcal{V}(u, v, \theta_\nu) &= \int \tilde{I}(u, v, \eta) e^{2\pi i\theta_\nu \eta} d\eta, \\ \tilde{I}(u, v, \eta) &= \int \mathcal{V}(u, v, \theta_\nu) e^{-2\pi i\theta_\nu \eta} d\theta_\nu. \end{aligned} \quad (3.14)$$

Here, $\theta_{\nu, \max} - \theta_{\nu, \min} = \Delta\nu$ is the bandwidth of the observed data cube, centered on z . The visibility is typically has units of milliKelvins or Janskys depending on the units in which intensity is measured.

Visibility Variance

Here we derive the variance of the visibility for an interferometric array of two antennas separated by a baseline $\vec{b} = (b_x, b_y)$, each with an effective collecting area A_e , observing a single element in the uv plane for time duration t_1 , with total bandwidth $\Delta\nu = \nu_{\max} - \nu_{\min}$. We choose notation that is consistent with the rest of this section, and adapted to the purpose of discussing measurement of a cosmological signal (as opposed to the traditional context of radio imaging). However, similar derivation can be found in the radio astronomy literature (see, e.g., Refs. Thompson et al. 2001; Perley et al. 1986), and in the literature discussing forecasts for 21-cm

In the following, for clarity, we omit the dependence on ν . The real (or imaginary) part of ρ has the following variance

$$\text{var}(\text{Re}[\rho_{ij}]) \frac{1}{2N_\nu} = \frac{1}{2t_1\Delta\nu}. \quad (3.18)$$

Before continuing, let us take a brief digression to show that the above formula implicitly assumes that the electric fields in the two antennas have a very weak correlation, $\rho \ll 1$. Consider two random Gaussian variables, x and y , both with zero mean values, where $\text{var}(x) \equiv \langle (x - \langle x \rangle)^2 \rangle = \langle x^2 \rangle - \langle x \rangle^2 = \langle x^2 \rangle$, and similarly for y . Their correlation coefficient is $\rho \equiv \frac{\langle xy \rangle}{\sqrt{\langle x^2 \rangle \langle y^2 \rangle}}$. In this case, the following is true

$$\begin{aligned} \text{var}(xy) &= \langle x^2 y^2 \rangle - \langle xy \rangle^2 = \langle x^2 \rangle \langle y^2 \rangle + \langle xy \rangle^2 \\ &= \langle x^2 \rangle \langle y^2 \rangle + \rho^2 \langle x^2 \rangle \langle y^2 \rangle = \text{var}(x)\text{var}(y)(1 + \rho^2), \end{aligned} \quad (3.19)$$

so that when ρ is small, $\text{var}(xy) = \text{var}(x)\text{var}(y)$, which was assumed in the first equality of Eq. (3.18).

Resuming the derivation, if different frequencies are uncorrelated, the result of Eq. (3.18) implies

$$\langle |\rho_{ij}(\nu)|^2 \rangle = \frac{1}{t_1\Delta\nu}. \quad (3.20)$$

The final step requires a relation between intensity on the sky $\mathcal{I}(\theta_x, \theta_y, \nu)$ (within the beam solid angle Ω_{beam} , centered on the direction $\hat{\mathbf{n}} = (\theta_x, \theta_y)$) and the electric fields measured in the two antennas,

$$\begin{aligned} \langle \tilde{E}_i^*(\nu) \tilde{E}_j(\nu) \rangle &\propto \int_{\Omega_{\text{beam}}} d\theta_x d\theta_y \mathcal{I}(\theta_x, \theta_y, \theta_\nu) \\ &\times e^{i\frac{2\pi\nu}{c}(b_x\theta_x + b_y\theta_y)} R(\theta_x, \theta_y), \end{aligned} \quad (3.21)$$

where $R(\theta_x, \theta_y)$ is the antenna response function (the shape of the beam in the sky), which we will assume to be unity. Furthermore, $\frac{2\pi\nu}{c}(b_x\theta_x + b_y\theta_y) \equiv 2\pi(u\theta_x + v\theta_y)$ is the phase delay between the two antennas (position in the uv plane measures the phase lag between the two dishes in wavelengths). The coefficient of proportionality in the above Equation is set by various instrumental parameters and is not relevant for our purposes. From Eq. (3.16), it follows that

$$\rho_{ij}(\nu) = \frac{\int_{\Omega_{\text{beam}}} d\theta_x d\theta_y \mathcal{I}(\theta_x, \theta_y, \theta_\nu) e^{2\pi i(u\theta_x + v\theta_y)}}{\int_{\Omega_{\text{beam}}} d\theta_x d\theta_y \mathcal{I}(\theta_x, \theta_y, \theta_\nu)}, \quad (3.22)$$

where the denominator in the above formula approximately integrates to (for a small beam)

$$\int_{\Omega_{\text{beam}}} d\theta_x d\theta_y \mathcal{I}(\theta_x, \theta_y, \theta_\nu) \approx \Omega_{\text{beam}} \mathcal{I}(\theta_x, \theta_y, \theta_\nu). \quad (3.23)$$

We can now use the approximate expression for the resolution of a single dish,

$$\Omega_{\text{beam}} = \frac{\lambda^2}{A_e}, \quad (3.24)$$

the Rayleigh–Jeans law (or the definition of the brightness temperature),

$$\mathcal{I}(\theta_x, \theta_y, \theta_v) = \frac{2k_B T_{\text{sky}}}{\lambda^2}, \quad (3.25)$$

and note that the numerator in Eq. (3.22) matches the definition of visibility from Eq. (3.14), to get

$$\rho_{ij}(v) = \frac{A_e}{2k_B T_{\text{sky}}} \mathcal{V}(u, v, \theta_v). \quad (3.26)$$

Combining Eq. (3.26) and Eq. (3.20), we get the final result of this derivation,

$$\begin{aligned} \langle |\mathcal{V}(u, v, \theta_v)|^2 \rangle &= \frac{1}{\Omega_{\text{beam}}} \left(\frac{2k_B T_{\text{sky}}}{A_e \sqrt{t_1 \Delta v}} \right)^2 \\ &\times \delta_D(u - u') \delta_D(v - v') \delta_{\theta_v, \theta_{v'}}, \end{aligned} \quad (3.27)$$

where the visibility \mathcal{V} is a complex Gaussian variable, centered at zero, and uncorrelated for different values of its arguments, and the factor of Ω_{beam} came from converting from Kronecker delta to a Dirac delta function. Note finally that we considered the contribution to the visibility from the noise only (the system temperature + the foreground sky temperature, in the absence of a signal); in the presence of a signal, T_{sky} should be the sum of the signal and the noise temperatures.

Power spectra and noise

In this Section, we derive the noise power spectrum for the brightness–temperature fluctuation measurement. We start by defining a brightness–temperature power spectrum as

$$\langle \tilde{I}(\vec{k}) \tilde{I}^*(\vec{k}') \rangle \equiv (2\pi)^3 P_{\mathcal{T}} \delta_D(\vec{k} - \vec{k}'), \quad (3.28)$$

where δ_D is Dirac delta function. The observable quantity of the interferometric arrays is the visibility function—a complex Gaussian variable with a zero mean and the following variance

$$\begin{aligned} &\langle \mathcal{V}(u, v, \theta_v) \mathcal{V}(u', v', \theta_{v'})^* \rangle \\ &= \frac{1}{\Omega_{\text{beam}}} \left(\frac{2k_B T_{\text{sky}}}{A_e \sqrt{\Delta v t_1}} \right)^2 \delta_D(u - u') \delta_D(v - v') \delta_{\theta_v, \theta_{v'}}, \end{aligned} \quad (3.29)$$

where T_{sky} is the sky temperature (which, in principle, includes both the foreground signal from the Galaxy, and the instrument noise, where we assume the latter to be

subdominant in the following); t_1 is the total time a single baseline observes element (u, v) in the uv plane; A_e is the effective collecting area of an antenna; k_B is the Boltzmann constant; $\Delta\nu$ is the bandwidth of a single observation centered on z ; and the last δ in this expression denotes the Kronecker delta.

Combining Eqs. (3.14) and (3.29), and taking the ensemble average,

$$\begin{aligned} & \langle \tilde{\mathcal{I}}(u, v, \eta) \tilde{\mathcal{I}}^*(u', v', \eta') \rangle \\ &= \frac{1}{t_1 \Omega_{\text{beam}}} \left(\frac{2k_B T_{\text{sky}}}{A_e} \right)^2 \delta_D(u - u') \delta_D(v - v') \delta_D(\eta - \eta'), \end{aligned} \quad (3.30)$$

where we used the standard definition

$$\int e^{2\pi i \theta_v (\eta - \eta')} d\theta_v = \delta_D(\eta - \eta'). \quad (3.31)$$

Taking into account the relation of Eq. (3.13), using Eq. (3.28), and keeping in mind the scaling property of the delta function, we arrive at

$$P_1^N(\vec{k}) = \frac{c(1+z)^2 \chi^2(z)}{\Omega_{\text{beam}} t_1 H(z) \nu_{21}} \left(\frac{2k_B T_{\text{sky}}}{A_e} \right)^2, \quad (3.32)$$

for the noise power per \vec{k} mode, per baseline.

In the last step, we wish to get from Eq. (3.32) to the expression for the noise power spectrum that corresponds to observation with all available baselines. To do that, we need to incorporate information about the array configuration and its coverage of the uv plane. In other words, we need to divide the expression in Eq. (3.32) by the number density of baselines $n_{\text{base}}(\vec{k})$ that observe a given mode \vec{k} at a given time (for a discussion of the uv coverage, see the following Section). The final result for the noise power spectrum per mode \vec{k} in intensity units is

$$P^N(\vec{k}) = \frac{c(1+z)^2 \chi^2(z)}{\Omega_{\text{beam}} t_1 H(z) \nu_{21}} \frac{(2k_B T_{\text{sky}})^2}{A_e^2 n_{\text{base}}(\vec{k})}, \quad (3.33)$$

and in temperature units

$$P^N(\vec{k}) = \frac{\lambda^4 c(1+z)^2 \chi^2(z)}{\Omega_{\text{beam}} t_1 H(z) \nu_{21}} \frac{T_{\text{sky}}^2}{A_e^2 n_{\text{base}}(\vec{k})}, \quad (3.34)$$

where $\lambda = c/\nu_{21}(1+z)$.

The UV coverage

The total number density $n_{\text{base}}(\vec{k})$ of baselines that can observe mode \vec{k} is related to the (unitless) number density $n(u, v)$ of baselines per $dudv$ element as

$$n_{\text{base}}(\vec{k}) = \frac{n(u, v)}{\Omega_{\text{beam}}}, \quad (3.35)$$

where $\frac{1}{\Omega_{\text{beam}}}$ represents an element in the uv plane. The number density integrates to the total number of baselines N_{base} ,

$$N_{\text{base}} = \frac{1}{2}N_{\text{ant}}(N_{\text{ant}} + 1) = \int_{\text{half}} n(u, v)dudv, \quad (3.36)$$

where N_{ant} is the number of antennas in the array, and the integration is done on one half of the uv plane¹. We assume that the array consists of many antennas and that time average of $n(u, v)$ should be computed to account for Earth's rotation.

In this work we focus on a specific array configuration that is of particular interest to cosmology—a compact grid of dipole antennas², with a total collecting area of $(\Delta L)^2$, and a maximum baseline length³ of ΔL . In this setup, the beam solid angle is 1 sr, the effective area of a single dipole is $A_e = \lambda^2$, and the effective number of antennas is $N_{\text{ant}} = \frac{(\Delta L)^2}{\lambda^2}$. For such a configuration, the number density of baselines entering the calculation of the noise power spectrum reads

$$n(u, v) = \left(\frac{\Delta L}{\lambda} - u\right)\left(\frac{\Delta L}{\lambda} - v\right). \quad (3.37)$$

The relation between $\vec{k} = (k, \theta_k, \phi_k)$ and (u, v) is

$$\begin{aligned} u_{\perp} &\equiv \frac{\chi(z)}{2\pi} k \sin \theta_k, \\ u &= u_{\perp} \cos \phi_k, \\ v &= u_{\perp} \sin \phi_k, \end{aligned} \quad (3.38)$$

where the subscript \perp denotes components perpendicular to the line-of-sight direction $\hat{\mathbf{n}}$, which, in this case, is along the z axis. From this, the corresponding number

¹This is because the visibility has the following property $V(u, v, \theta_v) = V^*(-u, -v, \theta_v)$, and only a half of the plane contains independent samples.

²Note that a densely filled array allows for higher surface brightness sensitivity to extended structures, which is essential for 21cm cosmology. While our calculation is geared towards a compact grid of dipoles as in the case of an Fast Fourier Transform Telescope (FFTT), Eq. 3.35 is more generally valid. Note that the Long Wavelength Array (LWA) discussed in Chapter V is *not* a FFTT.

³Note that for a square with area $(\Delta L)^2$ tiled in dipoles, there is a very small number of baselines longer than ΔL , but we neglect this for simplicity.

of baselines observing a given \vec{k} is

$$n_{\text{base}}(\vec{k}) = \left(\frac{\Delta L}{\lambda} - \frac{\chi(z)}{2\pi} k \sin \theta_k \cos \phi_k \right) \times \left(\frac{\Delta L}{\lambda} - \frac{\chi(z)}{2\pi} k \sin \theta_k \sin \phi_k \right). \quad (3.39)$$

As a last note, when computing numerical results, we substitute the ϕ_k -averaged version of the above quantity (averaged between 0 and $\pi/2$ only, due to the four-fold symmetry of the experimental setup of a square of dipoles) when computing the noise power, in order to account for the rotation of the baselines with respect to the modes in the sky. This average number density reads

$$\langle n_{\text{base}}(\vec{k}) \rangle_{\phi_k} = \left(\frac{\Delta L}{\lambda} \right)^2 - \frac{4}{\pi} \frac{\Delta L}{\lambda} \frac{\chi(z)}{2\pi} k \sin \theta_k + \frac{1}{\pi} \left(\frac{\chi(z)}{2\pi} k \sin \theta_k \right)^2, \quad (3.40)$$

assuming a given mode k is observable by the array, such that its value is between $2\pi L_{\text{min}}/(\lambda(z)\chi(z)\sin\theta_k)$ and $2\pi L_{\text{max}}/(\lambda(z)\chi(z)\sin\theta_k)$, where L_{min} and L_{max} are the maximum and minimum baseline lengths, respectively. If this condition is not satisfied, $\langle n_{\text{base}}(\vec{k}) \rangle_{\phi_k} = 0$.

3.4 Overview of Experimental Efforts

There are several ongoing and planned efforts to detect the 21cm signal from the dark ages as well as the epoch of reionization. While no experiment has made a detection of the 21cm power spectrum, many experiments have set interesting upper limits and have created exquisite maps that can be used to characterize foregrounds for upcoming experiments. I provide a brief overview of the experiments here.

Current Efforts

- **Long Wavelength Array (LWA):** The Owens Valley Long Wavelength Array (OVRO LWA) is a 288-antenna interferometer located at the Owens Valley Radio Observatory (OVRO). The LWA is a low-frequency instrument with instantaneous bandwidth covering 24 – 82 MHz. The OVRO LWA hosts the 512-input LEDA correlator, which allows the OVRO LWA to capture the entire visible hemisphere in a single snapshot image. We discuss the LWA configuration in detail in Chapter V.
- **The Murchison Widefield Array:** The MWA is a multi-purpose interferometer in Western Australia. It consists of 128 tiles, each made of 16 dual-

polarization dipole antennas. The MWA can form a discrete set of primary beams on the sky, each with a FWHM of 30 degrees. For EoR observations, this allows observers to adapt a “drift and shift” observation strategy, where the primary beam can shift once every 30 mins.

- **The Low Frequency Array (LOFAR):** LOFAR consists of two interferometers, of which the High Band Array, is geared towards 21cm observations. The LOFAR-HBA is similar to MWA in that each element of the interferometer is a analog phased array of 16 dipoles. While the collecting area for LOFAR is much larger than MWA, it cannot carry out correlations across every tile. The high level of RFI in the Netherlands also means LOFAR needs very fine frequency resolution, making correlations costlier.
- **The Precision Array for Probing the Epoch of Reionization (PAPER):** PAPER is an experiment exclusively dedicated to 21cm EoR observations located in the Karoo Desert of South Africa. It has 128 dipoles that sit on top of ground screens that are arranged in a highly redundant configuration. The redundant configuration allows for maximum sensitivity for a small number of baselines, ideal for EoR experiments.
- **The Canadian Hydrogen Intensity Mapping Experiment (CHIME):** CHIME is a cylindrical telescope with several feeds placed along the focal axis of each cylinder. The cylinders cannot be physically steered nor can the telescope electronically form and steer a beam. Instead, CHIME uses a zenith-pointing, drift-scan strategy like the LWA. The experiment is optimized for 21 cm intensity mapping at redshifts $z \sim 0.8 - 2.5$ where neutral hydrogen tomography will allow for a measurement of the Baryon Acoustic Oscillations (BAO) across the redshift range.

Planned Experiments

- **The Hydrogen Epoch of Reionization Array (HERA):** HERA is a 21cm experiments under construction in the South African Karoo Radio Astronomy Reserve. When complete, it will comprise of 350 14-m parabolic dishes observing from 50 to 250 MHz. HERA sacrifices pointing and sky coverage to substantially increase collecting area giving it an an order of magnitude more sensitivity than ongoing 21cm experiments.

- **The Square Kilometre Array (SKA):** The SKA is the most ambitious 21cm experiment planned to begin observations by late 2020s. In the first phase it will actually consist of two interferometers, the SKA1-LOW in Australia and the SKA1-MID in South Africa. 21cm cosmology will be the focus for SKA1-LOW, and will consist of 130,000 dipoles spread between 500 stations for a total collecting area of about 0.4km^2 . Each dipole in the array will be individually digitized and dipoles in a station will be added together to form 30 simultaneous beams of around 1 square degree.

Observational Challenges

While 21 cm tomography holds immense scientific promise, there remain a number of technical challenges that need to be addressed before the technique can be used for extracting cosmological information. The next generation of radio experiments will push the limits of digital signal processing: for instance, the SKA is expected to generate data at rates of 10^{15} bits/second which is ten times the current global internet traffic.

Astrophysical foregrounds pose the most serious challenge to the detection of the cosmological 21 cm signal. Much alike the CMB signal, the 21 cm signal is buried under much stronger, spectrally smooth foregrounds. In the case of the CMB, the intrinsic blackbody nature of the signal at different frequencies was exploited to distinguish it from foregrounds that have a non-thermal frequency dependence. For the 21 cm signal, measurement at different frequencies corresponds to signals from spatially distinct regions (since frequency corresponds to redshift). Hence the cosmological 21 cm signal is expected to have structure in frequency space, while the foregrounds are expected to be spectrally smooth. This property can in principle be exploited to remove the foregrounds.

At low frequencies, synchrotron emission from our Galaxy and other radio galaxies are the dominant foregrounds. Additionally there is a small contribution from free-free emission. Unresolved extragalactic radio galaxies also contribute to the foreground and the emission from these radio sources is dominated by synchrotron emission. Both synchrotron and free-free emission are spectrally smooth and this feature can be exploited to remove them by using maps at multiple frequencies that 21 cm tomography experiments will produce.

Spectrally un-smooth foregrounds include radio frequency interference (RFI) from terrestrial sources that can dominate over galactic and extragalactic foregrounds.

Most 21 cm experiments are thus situated/planned in radio-quiet regions. The chromatic nature of an interferometer also introduces spectral features in astrophysical foregrounds and these features depend on the instrument. As discussed in Sec. 3.2, this un-smooth component is confined to a “wedge” at low k_{\parallel} (corresponding to wavenumbers along the line of sight) and low k_{\perp} (corresponding to wavenumbers on the plane of the sky). This chromaticity of interferometers also means that they need to be very carefully calibrated across different frequencies before the spectrally smooth foregrounds can be removed.

Finally, the ionosphere leads to a time-dependent variation in the signal since it acts like a turbulent plasma screen. The careful characterization of the ionosphere at high cadence, and across a wide field-of-view will thus be critical to extract the cosmological signal.

These technical challenges have not deterred intrepid efforts to detect the cosmological 21 cm signal. While we only have (weak) upper limits on the power spectrum at low-frequencies today, improved instrumentation and better analysis techniques are likely to enable the first measurement of the cosmological 21 cm power spectrum in the next decade.

References

- Furlanetto, S. R., Oh, S. P., & Briggs, F. H., 2006, *PhR*, 433, 181
- Furlanetto, S. R., Lidz, A., Loeb, A., et al., 2009, in *ArXiv Astrophysics e-prints*, astro2010: The Astronomy and Astrophysics Decadal Survey, Vol. 2010
- Gluscevic, V., Venumadhav, T., Fang, X., et al., 2017, *PhRvD*, 95.8, 083011, 083011
- Mao, Y., Tegmark, M., McQuinn, M., Zaldarriaga, M., & Zahn, O., 2008, *PhRvD*, 78.2, 023529, 023529
- Perley, R. A., Schwab, F. R., Bridle, A. H., & Ekers, R. D. 1986, *Synthesis imaging. Course notes from an NRAO summer school, held at Socorro, New Mexico, USA, 5 - 9 August 1985.*
- Pober, J. C., Liu, A., Dillon, J. S., et al., 2014, *ApJ*, 782, 66, 66
- Pritchard, J. R., & Loeb, A., 2012, *Reports on Progress in Physics*, 75.8, 086901, 086901
- Seo, H.-J., & Hirata, C. M., 2016, *MNRAS*, 456, 3142
- Tegmark, M., & Zaldarriaga, M., 2009, *PhRvD*, 79.8, 083530, 083530
- Thompson, A. R., Moran, J. M., & Swenson Jr., G. W. 2001, *Interferometry and Synthesis in Radio Astronomy*, 2nd Edition

Chapter 4

DETECTING PRIMORDIAL GRAVITATIONAL WAVES WITH
CIRCULAR POLARIZATION OF THE REDSHIFTED 21 CM
LINE

ABSTRACT

We propose a new method to measure the tensor-to-scalar ratio r using the circular polarization of the 21 cm radiation from the Dark Ages. Our method relies on the splitting of the $F = 1$ hyperfine level of neutral hydrogen due to the quadrupole moment of the CMB during the Dark Ages. We show that unlike the Zeeman effect, where $M_F = \pm 1$ have opposite energy shifts, the CMB quadrupole shifts $M_F = \pm 1$ together relative to $M_F = 0$. This splitting leads to a small circular polarization of the emitted 21 cm photon, which is in principle observable. Further, we forecast the sensitivity of future radio experiments to measure the CMB quadrupole during the era of first cosmic light ($z \sim 20$). The tomographic measurement of 21 cm circular polarization allows us to construct a 3D remote quadrupole field. Measuring the B -mode component of this remote quadrupole field can be used to put bounds on the tensor-to-scalar ratio r . We make Fisher forecasts for a future Fast Fourier Transform Telescope (FFTT), consisting of an array of dipole antennas in a compact grid configuration, as a function of array size and observation time. We find that a FFTT with a side length of 100 km can achieve $\sigma(r) \sim 4 \times 10^{-3}$ after ten years of observation and with a sky coverage $f_{\text{sky}} \sim 0.7$. The forecasts are dependent on the evolution of the Lyman- α flux in the pre-reionization era, that remains observationally unconstrained. Finally, we calculate the typical order of magnitudes for circular polarization foregrounds and comment on their mitigation strategies. We conclude that detection of primordial gravitational waves with 21 cm observations is in principle possible, so long as the primordial magnetic field amplitude is small, but would require a very futuristic experiment with corresponding advances in calibration and foreground suppression techniques.

4.1 Introduction and Motivation

The idea that the early universe underwent a period of inflationary expansion, is one of the cornerstones of modern cosmology. Inflation was originally invoked as a solution to the flatness and horizon problems Guth 1981 but proved to be a powerful explanation for the generation of initial perturbations in the early universe, that eventually evolved to the large scale structure we see today Guth & Pi 1982; Bardeen et al. 1983; Hawking 1982; Linde 1982; Mukhanov & Chibisov 1981. Increasingly precise cosmological tests have verified the predictions of the simplest single-field-slow-roll inflationary models; that the primordial density perturbations are adiabatic, nearly Gaussian, and nearly (but not exactly) scale-invariant Planck Collaboration et al. 2016a; Planck Collaboration et al. 2016b; Martin 2016.

Beyond the predictions for primordial density (scalar) perturbations, inflation also predicts the existence of a stochastic gravitational wave background, with a nearly scale-invariant power spectrum Abbott & Wise 1984; Rubakov et al. 1982; Fabbri & Pollock 1983; Starobinskiĭ 1979. Detection of these inflationary gravitational waves would be a smoking gun for inflation, and their detection would open up a completely new window into both the physics of the very early universe and physics at otherwise inaccessible energy scales, $V_{inf}^{1/4} \sim 10^{-3}(r/0.01)^{1/4}M_{Pl}$, where r is the tensor-to-scalar ratio and M_{Pl} is the Planck mass.

The principal near-term strategy to detect inflationary gravitational waves relies on the fact that waves with wavelengths comparable to the horizon size would induce a gradient free “B-mode” pattern in the polarization of the CMB via Thomson scattering Kamionkowski et al. 1997a; Kamionkowski et al. 1997b; Seljak 1997; Seljak & Zaldarriaga 1997; Zaldarriaga & Seljak 1997. There are several experimental efforts underway to detect the B-mode pattern in the CMB polarization, including ABS (Atacama B-mode Search) Essinger-Hileman et al. 2010, ACTPol Naess et al. 2014, BICEP2/Keck Array BICEP2 Collaboration et al. 2014; BICEP2 and Keck Array Collaborations et al. 2015 and POLARBEAR/Simons Array Arnold et al. 2014. The search for inflationary gravitational waves remains the top scientific priorities for future CMB experiments (see the CMB S4 Science Book Abazajian et al. 2016).

As discussed in Chapter 2, the strength of the inflationary gravitational waves is encoded in the tensor-to-scalar ratio r , which is related to the Hubble rate during inflation and in turn depends on the energy scale at which inflation takes place. It is

defined as $r = \Delta_h^2/\Delta_\zeta^2$ where,

$$\Delta_\zeta^2(k) \equiv \frac{k^3}{2\pi^2} \langle |\zeta|^2 \rangle \quad (4.1)$$

is the power spectrum of the curvature perturbations and

$$\Delta_h^2(k) \equiv 2 \frac{k^3}{2\pi^2} \langle |h_k|^2 \rangle = \frac{2}{\pi^2} \frac{H^2}{M_{\text{pl}}^2} \quad (4.2)$$

is the gravitational-wave power spectrum (summed over two polarizations), where H is the Hubble rate during inflation. The value of r depends on the model of inflation considered. Current constraints on r from the combination of the CMB B -mode and other (more model-dependent) observables are $r < 0.07$ (95% CL) BICEP2 Collaboration et al. 2016.

Galactic foregrounds, primarily due to dust emission, make the detection of tensor modes using the CMB particularly challenging. Gravitational lensing due to scalar perturbations also produce a B -mode pattern and might fundamentally limit the values of r that can be probed using the CMB. In the event that future CMB experiments do detect B -modes due to inflationary GWs, it is important to devise methods, with different systematic errors, that will conclusively prove that the GW signal is indeed primordial. Furthermore, in the event that the value of $r \lesssim 0.001$, planned CMB experiments are unlikely to be able to detect B -modes. It is thus appropriate to investigate alternative methods to detect inflationary gravitational waves.

Hirata et al. 2017 calculated the effect of the CMB quadrupole during the Dark Ages of the universe on the splitting of the $F = 1$ hyperfine excited level of neutral hydrogen at high redshifts. We showed that unlike the Zeeman effect, where $M_F = \pm 1$ have opposite energy shifts, the remote CMB quadrupole shifts $M_F = \pm 1$ together relative to $M_F = 0$. This leads to a small circular polarization of the emitted 21cm photon, which is in principle observable.

Measurement of the circular polarization of the 21cm signal using future radio interferometers can allow us to construct a 3D remote CMB quadrupole field (i.e. the quadrupole component of the CMB skies observed by hydrogen atoms at high redshifts) during the cosmic Dark Ages. Just like the CMB polarization field, this field can be decomposed into E and B modes. The measurement of B modes of this new remote quadrupole field, can then be used to put bounds on r .

In this chapter we forecast the ability of future radio experiments to measure the remote quadrupole of the CMB using the circular polarization of the 21 cm line. We show that a very large Fast Fourier Transform Telescope (FFTT) Tegmark & Zaldarriaga 2009 can in principle construct a remote quadrupole field at high redshifts ($z \sim 20$), and we make forecasts for the measurement of r as a function of array size and survey duration.

This chapter is organized as follows: we provide a broad outline of the formalism presented in Hirata et. al. (2017) in Sec. 4.2 and provide an outline for our method in Sec. 4.3. In Sec. 4.4 we make forecasts for the measurement of the remote quadrupole of the CMB using Fast Fourier Transform Telescopes. In Sec. 4.5 we compute the power spectrum of the remote CMB quadrupole and sensitivity to r . In Sec. 4.6 we discuss various foregrounds that are relevant to our measurement, and in Sec. 4.7 we summarize and discuss the implications of our results.

4.2 Formalism

Scattering processes between photons and neutral hydrogen atoms in the early universe can affect 21cm observables, and lead to novel probes of physics at high redshifts. An extensive review of the physics of the 21 cm transition can be found in Furlanetto et al. 2006. Recently, Venumadhav et al. 2014 and Gluscevic et al. 2017 considered the effect of magnetic fields in the early universe on the splitting of the $F = 1$ hyperfine excited level of hydrogen. At high redshifts, a neutral hydrogen atom is bathed in an anisotropic 21 cm radiation bath due to density fluctuations in the gas. Such an anisotropic radiation field leads to spin polarization of the neutral hydrogen atoms in the $F = 1$ state, and hydrogen atoms in the excited $F = 1$ state align with the quadrupole of the incident 21 cm radiation. The presence of an external magnetic field leads to the precession of atoms in the $F = 1$ state, and the emitted 21 cm radiation is misaligned with the incident 21 cm quadrupole. Gluscevic et al. 2017 showed that this effect can be used to probe large scale magnetic fields during the Dark Ages; an array of dipole antennas in a compact grid configuration with a collecting area of approximately one square kilometer can achieve a $\sigma(B) \sim 10^{-21}$ Gauss (comoving, scaled to present day value), after 3 years of observation.

Beyond the Zeeman splitting due to an external magnetic field, the CMB anisotropy at high redshifts also leads to a splitting of the $F = 1$ level but the symmetry properties is different from the magnetic field case. In the case of an external

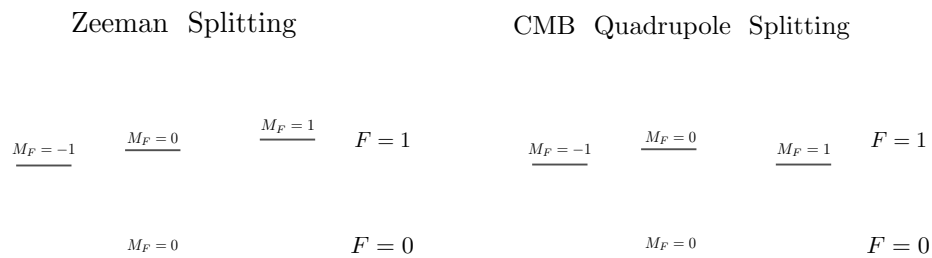


Figure 4.1: Energy Level Splitting

magnetic field (Zeeman effect), the energy levels of the $M_F = \pm 1$ levels shift in opposite directions, while the CMB anisotropy leads to a shift in the same direction (see Fig. 4.1). The emitted 21 cm photon in the latter case has small circular polarization.

In the remainder of this section we sketch the calculation described in detail in Hirata et. al. 2017. We are interested in calculating the relative change in the sub level energies $\mathcal{E}_{M_F=1} - \mathcal{E}_{M_F=0}$ due to an anisotropic external blackbody.

In second-order perturbation theory, an interaction can break the degeneracy between two otherwise degenerate states. Consider the three $M_F = \pm 1, 0$ for the $F = 1$ hyperfine level. In the case of Zeeman effect it is a DC magnetic field that leads to this breaking of degeneracy; in our case we consider the AC magnetic field from a *non-resonant* radiation field Γ .

The interaction leads to a change in the Hamiltonian matrix element between two degenerate states:

$$\Delta\mathcal{E}_{ji} = \left\langle \langle j | H_{int} | i \rangle + \sum_{n,\Gamma} \frac{\langle j | H_{int} | n, \Gamma \rangle \langle n, \Gamma | H_{int} | i \rangle}{\mathcal{E}_j - \mathcal{E}_{n,\Gamma}} \right\rangle_{rad}, \quad (4.3)$$

where H_{int} is the Hamiltonian of the interaction, $|n\rangle$ denotes an intermediate state of the hydrogen atom, and $\mathcal{E}_{n,\Gamma}$ is the energy of $|n\rangle$ plus the additional energy due to all photons present or absent in the intermediate state $|\Gamma\rangle$ relative to the initial photon state. The expectation value is taken over statistical realizations of the radiation field.

Hirata et. al. (2017) compute both electric dipole and magnetic dipole interactions and show that the magnetic dipole interaction dominates. For the case of a magnetic dipole interaction, the interaction Hamiltonian for the atom and the incident can be written as $H_{int} = \boldsymbol{\mu} \cdot \mathbf{B}$. Consider, an incident radiation field at frequency ω and

with a quadrupolar anisotropy of the form $T(\mathbf{n}) = T_\gamma[1 + a_{20}Y_{20}(\mathbf{n})]$. Here we chose a quadrupole that is symmetric around the z-axis for simplicity. We can use this symmetry to determine the contribution of the other a_{2m} 's. We can show that the energy splitting of the degenerate levels due to the quadrupolar anisotropy a_{20} is given by,

$$\begin{aligned} \frac{\Delta\mathcal{E}_{11}^{\text{mag.dip.}} - \Delta\mathcal{E}_{10}^{\text{mag.dip.}}}{\hbar} &= -\sqrt{\frac{5}{\pi^3}} \frac{\mu_B^2 \omega_{hf} a_{\text{rad}} T_\gamma^2}{k_B^2} a_{20} \\ &= -4.4 \times 10^{-10} \text{ s}^{-1} \left(\frac{T_\gamma}{60 \text{ K}} \right)^2 a_{20}. \end{aligned} \quad (4.4)$$

where μ_B is the Bohr magneton, a_{rad} is the radiation energy density constant, and T_γ is the blackbody temperature. For typical CMB quadrupole anisotropies of order 2×10^{-5} , and temperatures of order 60 K ($z \sim 20$), the energy splitting and hence the precession rate is of order 10^{-14} s^{-1} . This result can be generalized to other components of the quadrupole (see Equation (17) in Hirata et. al. (2017)).

The atomic density matrix evolves due to the energy shift $\Delta\mathcal{E}_{m,m'}$ and the evolution equation is given by,

$$\dot{\rho}_{mm'}^{\text{shift}} = i[\rho, \Delta\mathcal{E}]_{mm'} = i\rho_{mm_1} \Delta\mathcal{E}_{m_1 m'} - i\Delta\mathcal{E}_{mm_1} \rho_{m_1 m'}. \quad (4.5)$$

By using the expression for the energy shift due to a quadrupolar field $\Delta\mathcal{E}_{m,m'}$ in the evolution equation above, we can solve for the time-evolution of the components of the atomic density matrix. The calculation is rather involved and beyond the scope of this chapter. Here we provide a simple argument for why a CMB quadrupole leads to a circular polarization of the re-scattered 21 cm photons.

Neutral hydrogen atoms in the excited triplet ($F = 1$) state have a magnetic dipole moment and preferentially emit perpendicular to the magnetic moment. In an isotropic bath of 21 cm photons the magnetic dipole moments do not have any preferred direction or alignment. However, the 21 cm photon field in the early universe has a quadrupole due to density fluctuations. The 21 cm quadrupole leads to the magnetic moments being aligned perpendicular to the direction of the quadrupole.

Now consider the effect of the CMB quadrupole moment along the z-axis on spin polarized hydrogen atoms aligned along the z-axis, in a coordinate system where

the observer is along the x -axis. The quadrupolar anisotropy of the incident CMB radiation along the z -axis, leads to an energy level splitting of the atoms aligned along the z -axis (as shown in Fig. 4.1). Meanwhile, atoms aligned along x and y axis remain unaffected.

The energy level splitting for atoms aligned along the z -axis leads to a energy difference in the re-scattered photons along the x -axis (the line-of-sight); re-scattering from atoms along the x and y axis does not lead to an energy shift. Quantum mechanically, the energy difference in the re-scattered photons corresponds to a phase shift, and this phase shift leads to a *circular polarization* of the re-scattered photons from the atoms aligned along the z -axis.

Note that if the quadrupole is aligned along the line-of-sight (x -axis), the re-scattered photons reaching the observer are from atoms aligned along z and y axis (since re-scattering is preferentially perpendicular to the magnetic moment), and do not have a quadrupole-induced phase shift. Hence the CMB quadrupole that is symmetric along the line-of-sight does not lead to a circularly polarized 21 cm photon.

Hirata et. al. (2017) solve the detailed radiative transfer equations using the components of the atomic density matrix obtained using the prescription described earlier. The final result of the calculation is a circular polarization amplitude due to transition from $F = 1$ to the $F = 0$ state and is related to the CMB quadrupole by,

$$V_{obs} = -\frac{\sqrt{2\pi}}{25\sqrt{3}} \frac{T_s T_\star K_{mag} f \tau^2 \delta}{T_{\gamma 0} A (1 + 0.75 \tilde{x}_\alpha)(1 + \tilde{x}_c + \tilde{x}_\alpha)} \times \left(1 - \frac{T_\gamma}{T_s}\right) \Im[a_{21} Y_{21}(\hat{\mathbf{k}}) + 2a_{22} Y_{22}(\hat{\mathbf{k}})]. \quad (4.6)$$

where $\hat{\mathbf{k}}$ is the direction of the wavenumber; \tilde{x}_α and \tilde{x}_c parametrize the rates of depolarization of the ground state by optical pumping and atomic collisions respectively; T_s and T_γ are the spin temperature and the CMB temperature at redshift z ; f is the rate of growth of structure, and is ≈ 1 in the matter-dominated era; δ is the density contrast; τ is the 21 cm optical depth, a_{2m} is the CMB quadrupole at the redshift z ; and K_{mag} is a combination of constants given by,

$$K_{mag} \equiv \sqrt{\frac{50}{3\pi^3}} \frac{\mu_B^2 \omega_{hf} a_{rad} T_{\gamma,0}^2}{k_B^2} = 1.65 \times 10^{-12} \text{ s}^{-1}, \quad (4.7)$$

The spin-zero spherical harmonics Y_{2m} are defined in the usual way.

Note that the circular polarization signal in Eq. 4.6 depends on $\hat{\mathbf{k}}$ - the 3D orientation of the wave vector. Hence by measuring the circular polarization in a tomographic survey we can, in principle, extract the CMB multipoles a_{21} and a_{22} .

4.3 Outline of the Method

The measurement of the new circular polarization power-spectra can allow us to measure the *remote quadrupole* of the CMB, in a given volume-pixel in the sky, at a high redshift ($z > 10$). For a wide-angle, tomographic 21 cm survey, we can measure the remote quadrupole of the CMB in many voxels in the sky, allowing us to construct a 3D remote quadrupole field at high redshifts. The 3D remote CMB quadrupole field in turn can be decomposed into E and B modes in analogy with the decomposition of the CMB polarization field Kamionkowski et al. 1997a; Kamionkowski et al. 1997b; Seljak & Zaldarriaga 1997; Zaldarriaga & Seljak 1997; Seljak 1997. We show that the power-spectra of the "B-modes" of the remote quadrupole field can be used to measure the tensor-to-scalar ratio r . A schematic of our method is shown in Fig. 4.2.

One way of thinking about our method is to imagine neutral hydrogen in all the voxels in Fig. 4.2 to be independent CMB-quadrupole detectors. The construction of the new remote quadrupole field during the dark ages allows for the statistical measurement of the E and B modes which in turn contains information about primordial tensor modes (i.e. gravitational waves). Our method is similar to the one proposed in Ref. Kamionkowski & Loeb 1997, but the authors suggest the use of discrete clusters to reconstruct the CMB quadrupole moments at their locations. Our method, in principle, allows for construction of a continuous field of remote quadrupole moments, and probes higher redshifts than those accessible to the cluster method (see also Refs. Cooray & Baumann 2003; Doré et al. 2004; Skordis & Silk 2004; Portsmouth 2004; Bunn 2006; Alizadeh & Hirata 2012).

4.4 Measuring the Remote Quadrupole of the CMB

In this section we compute the sensitivity of future tomographic 21 cm surveys to measure the remote quadrupole of the CMB at high redshifts. We begin by reviewing some basic notation relevant to remote CMB quadrupole measurements. The experimental setup ideal for this measurement is the Fast Fourier Transform Telescope (FFTT) setup, due to its excellent surface brightness sensitivity compared to sparsely sampled arrays Tegmark & Zaldarriaga 2009. We review the FFTT setup and make Fisher matrix forecasts for the measurement of the remote quadrupole for

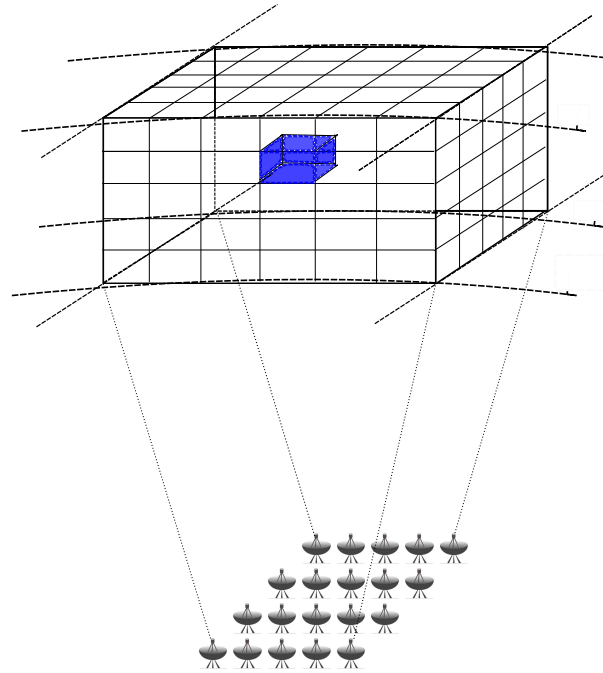


Figure 4.2: Tomographic measurements by Fast Fourier Transform Telescopes (FFTTs) would allow us to measure the remote quadrupole of the CMB $a_{2m}(z)$ ($m = 1, 2$) in volume pixels ("voxels") of volume \mathcal{V}_c in narrow slice of redshift space. Creating a map of remote quadrupole moments across many voxels allows us to construct a spin-weight m field, which can be decomposed into E and B modes. Measurement of the B -modes of this field allows us to put bounds on the tensor-to-scalar ratio r .

different FFTT configurations. In this section, the CMB quadrupole is simply taken as an input; we will compute its statistical properties and the role of scalar and tensor perturbations in Sec. 4.5.

Relation of the 21 cm power spectrum to the remote quadrupole of the CMB

The central idea of our technique is that the circular polarization of the emitted 21 cm radiation from the high-redshift hydrogen cloud depends on the remote quadrupole of the CMB at that redshift depends on through Eq. (4.6). Specifically, the existence of a CMB quadrupole at some position results in the creation of new power spectra involving the circular polarization that would otherwise be zero. We focus on the temperature-circular polarization cross-power spectrum TV , since its signal-to-noise ratio scales with the amplitude of the CMB quadrupole effect ($\text{SNR} \propto a_{2m}$) instead

of the case of the circular polarization auto-power spectrum VV ($\text{SNR} \propto a_{2m}^2$):

$$P_{TV}(k) = \frac{\partial T_{obs}}{\partial \delta}(k) \frac{\partial V_{obs}}{\partial \delta}(k) P_{\delta}(k). \quad (4.8)$$

The temperature perturbation is given by the usual relation,

$$\frac{\partial T_{obs}}{\partial \delta} = 37.3 \text{ mK} \left(\frac{1+z}{20} \right)^{1/2} \left(1 - \frac{T_{\gamma}}{T_s} \right) [1 + (\hat{\mathbf{k}} \cdot \hat{\mathbf{n}})^2]. \quad (4.9)$$

From Eq. (4.6) we can see that the circular polarization transfer function $\partial V_{obs}/\partial \delta$ is given by,

$$\begin{aligned} \frac{\partial V_{obs}}{\partial \delta} &= -8.6 \text{ mK} \left(\frac{1+z}{20} \right)^2 \frac{T_{\gamma}}{T_s} \left(1 - \frac{T_{\gamma}}{T_s} \right) \\ &\quad \times \frac{1}{(1 + 0.75\tilde{x}_{\alpha})(1 + \tilde{x}_c + \tilde{x}_{\alpha})} \\ &\quad \times \Im[a_{21}Y_{21}(\hat{\mathbf{k}}) + 2a_{22}Y_{22}(\hat{\mathbf{k}})]. \end{aligned} \quad (4.10)$$

The circular polarization transfer function depends on the direction of the wavenumber $\hat{\mathbf{k}}$.

The power spectrum $P_{TV}(k)$ is thus sensitive to 4 of the 5 types of quadrupole moments of the CMB. Each of these 4 quadrupole moments leads to a quadrupole dependence of the TV spectrum:

- An xz CMB quadrupole ($\Re a_{21} < 0$) leads to a positive TV spectrum for $k_y k_z < 0$ and negative for $k_y k_z > 0$.
- A yz CMB quadrupole ($\Im a_{21} > 0$) leads to a positive TV spectrum for $k_x k_z > 0$ and negative for $k_x k_z < 0$.
- An $x^2 - y^2$ CMB quadrupole ($\Re a_{22} > 0$) leads to a positive TV spectrum for $k_x k_y < 0$ and negative for $k_x k_y > 0$.
- An xy CMB quadrupole ($\Im a_{22} < 0$) leads to a positive TV spectrum for $k_x^2 - k_y^2 > 0$ and negative for $k_x^2 - k_y^2 < 0$.
- The observable $P_{TV}(k)$ is not sensitive to the $m = 0$ CMB quadrupole mode that is symmetric around the line of sight.

Local power spectrum and detectability

In this section we evaluate sensitivity of future tomographic 21 cm surveys to the remote quadrupole of the CMB. The ability to measure the remote CMB quadrupole can be determined using the Fisher formalism: in a region of comoving volume \mathcal{V}_c , we have

$$F_{\mu\nu} = \int \frac{d^3\mathbf{k}}{(2\pi)^3} \frac{\mathcal{V}_c [\partial P_{TV}(\mathbf{k})/\partial p_\mu][\partial P_{TV}(\mathbf{k})/\partial p_\nu]}{[P_{TT}(\mathbf{k}) + N_{TT}(\mathbf{k})][P_{VV}(\mathbf{k}) + N_{VV}(\mathbf{k})]}, \quad (4.11)$$

where \mathcal{V}_c is the comoving volume and p_μ are the parameters – in this case the 4 measurable quadrupole components: $\mathfrak{K}_{a_{21}}$, $\mathfrak{I}_{a_{21}}$, $\mathfrak{K}_{a_{22}}$, and $\mathfrak{I}_{a_{22}}$. Here $N_{TT}(\mathbf{k})$ is the temperature noise power spectrum, and $N_{VV}(\mathbf{k})$ is the circular polarization noise power spectrum. For a dual-polarization interferometer with the same noise temperature in both polarizations, $N_{VV}(\mathbf{k}) = N_{TT}(\mathbf{k})$. We discuss the noise power spectrum in Sec. 4.4. Under the further assumption of noise power spectra that are symmetric around the line of sight (which occurs when the distribution of baselines is nearly circularly symmetric), the Fisher matrix reduces to

$$F_{\mu\nu} = \mathcal{V}_c \begin{pmatrix} w_1 & 0 & 0 & 0 \\ 0 & w_1 & 0 & 0 \\ 0 & 0 & w_2 & 0 \\ 0 & 0 & 0 & w_2 \end{pmatrix}. \quad (4.12)$$

That is, there is an inverse variance per component of w_m (units: Mpc^{-3}) per unit comoving volume, which may be different for the $m = 1$ and $m = 2$ quadrupole components. The Fisher estimate of the variance in $\mathfrak{K}_{a_{2m}}$ or $\mathfrak{I}_{a_{2m}}$ is $1/(w_m \mathcal{V}_c)$. Two diagonal elements of Eq. (4.11) suffice to determine w_1 and w_2 .

Fast Fourier Transform Telescopes

The ideal experimental setup for measuring the remote quadrupole of the CMB using the circular polarization of 21 cm is the proposed Fast Fourier Transform Telescope (FFTT) as described in Tegmark & Zaldarriaga 2009. The FFTT consists of a tightly packed array of simple dipole antennas in a regular rectangular grid. The electric field is digitized at the antennae and subsequent correlations and Fourier transforms are done digitally. The FFTT is based on the simple idea that if the antennae are arranged on a rectangular grid, Fast Fourier Transforms can be used to scale the cost as $N \log_2 N$ instead of N^2 (where N is the number of antennae). The FFTT concept allows for mapping of a very wide field of view with very high sensitivity, making it ideal for 21 cm tomography experiments.

A schematic of the FFTT design we consider for the forecasts in this paper is shown in Fig. 4.2. We consider a square array design with a compact grid of dipole antennas with side length L , effective area L^2 , that observes for a time τ with a bandwidth $\delta\nu$ around some frequency ν . In principle the array can observe the entire visible sky at any given time. The figure shows how we split the 3D volume of the universe at high redshifts observed by the array into smaller volume pixels ("voxels"). Our goal is to estimate the detectability of the remote CMB quadrupole in each of these voxels.

The experiment is characterized by three key parameters: the length of the array L , the time of observation τ and the system temperature T_{sys} . The noise power spectrum per mode \mathbf{k} (in intensity units) is given by

$$N_{TT}(\mathbf{k}) = \frac{\lambda^4 c(1+z)^2 D_M^2(z)}{\Omega_{\text{beam}} \tau H(z) \nu_{21}} \frac{T_{\text{sys}}^2}{A_e^2 n_{\text{base}}(\mathbf{k})}, \quad (4.13)$$

where $D_M(z)$ is the comoving distance to the redshift z , A_e is the collecting area, and $n_{\text{base}}(\mathbf{k})$ is the number density of baselines that observe a given mode \mathbf{k} at a given time. Here noise is reported in temperature units, T in K and $N_{TT}(\mathbf{k})$ in $\text{K}^2 \text{Mpc}^3$ (Gluscevic et al. 2017).

A given mode in the sky \mathbf{k} , will be observed by many baselines of the FFTT during an observation campaign. Hence the noise power spectrum needs to be weighed by the number of baselines observing a given mode \mathbf{k} . The number of baselines observing a mode \vec{k} is given by

$$\langle n_{\text{base}}(\mathbf{k}) \rangle = \left(\frac{L}{\lambda} \right)^2 - \frac{4 L D_M(z)}{\pi \lambda} \frac{k \sin \theta_k}{2\pi} + \frac{1}{\pi} \left[\frac{D_M(z)}{2\pi} k \sin \theta_k \right]^2, \quad (4.14)$$

where θ_k is the polar angle and ϕ_k the longitude in a coordinate system where the line of sight is along the z axis. The number of baselines is averaged over ϕ_k , which is appropriate if at least $\sim 90^\circ$ of Earth rotation occurs over the course of an observing window.

Results for reference experiments

We now proceed to evaluate the sensitivity of a tomographic 21 cm survey to measure the remote quadrupole of the CMB during the pre-reionization epoch, at a given redshift z and for a "voxel" of volume \mathcal{V} . Specifically, we compute the elements

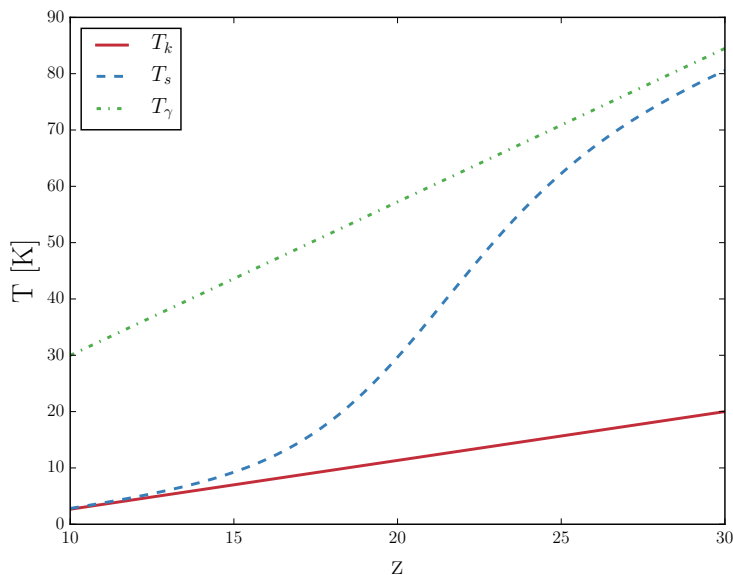


Figure 4.3: Inputs used for the sensitivity calculation, computed for standard cosmology using the 21CMFAST code. The plot shows the fiducial models for spin, kinetic, and CMB temperatures.

of the Fisher matrix (Eq. 4.11), for different FFTT configurations and observation times.

We consider a square-grid configuration for the FFTT with a length L and collecting area $A_e = L^2$. The time τ for computing the noise spectra in Eq. (4.13) is the *observing time*, which is smaller than the wall-clock time since a given portion of the sky is visible for only part of the day. We assume a system temperature of $T_{\text{sys}} = 1000\text{K}$.

Other inputs to the sensitivity calculation include: the spin and kinetic temperatures of the IGM, along with the CMB temperature (Fig. 4.3); the quantities that parametrize the rate of depolarization of the ground state by optical pumping and atomic collisions (Fig. 4.4). These quantities are calculated using the 21CMFAST code (Mesinger et al. 2011), and the matter power spectra from the CAMB code (Lewis et al. 2000). As inputs to 21CMFAST and CAMB, we use standard cosmological parameters ($H_0 = 67 \text{ km s}^{-1} \text{ Mpc}^{-1}$, $\Omega_m = 0.32$, $\Omega_K = 0$, $n_s = 0.96$, $\sigma_8 = 0.83$, $w = -1$) consistent with Planck measurements (Planck Collaboration et al. 2016c). For the 21CMFAST runs, we set the sources responsible for early heating to Population III stars by setting Pop= 3, and keep all other input parameters at their default values, with the exception of the star formation efficiency, F_STAR. For our fiducial

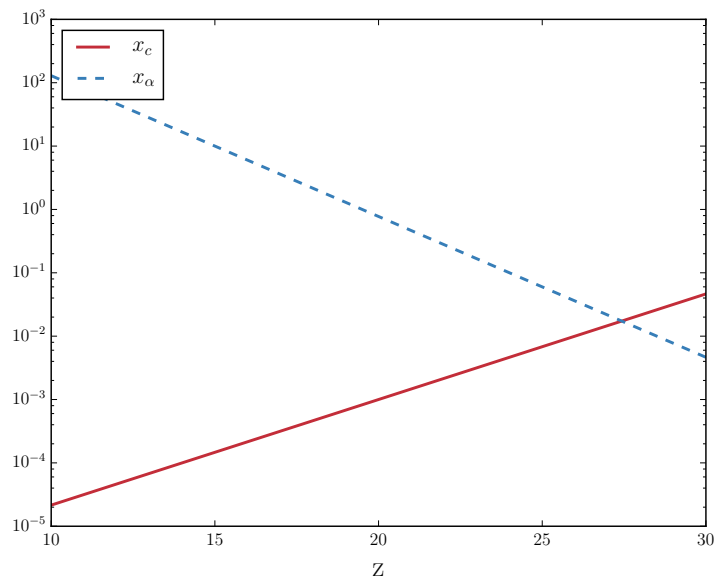


Figure 4.4: Inputs used for the sensitivity calculation, computed for standard cosmology using the 21CMFAST code. The plot shows the fiducial models for quantities that parametrize the rate of depolarization of the ground state by optical pumping and atomic collisions as discussed in the text and in Gluscevic et al. 2017

calculation we choose $F_{\text{STAR}}=0.0075$. The fiducial model is chosen to match the models from Haardt & Madau 2012 at $z = 15$ which were computed by extrapolation of the flux measurements from observations at much lower redshifts. As reported by Gluscevic et al. 2017 this model is physically reasonable, since it produces a sufficient number of ionizing photons to reionize the universe at lower redshifts.

A FFTT can in principle observe the entire sky above the horizon. However, the image degrades rapidly near the horizon and the useful field of view is about half $\Omega \sim \pi$. The angular resolution of a FFTT is $\theta_{\text{res}} \sim \lambda/\sqrt{A}$. The angular scale of the "voxel" in which the CMB quadrupole is measured to be approximately ten times the angular resolution of the telescope. The maximum comoving wavenumber probed by the FFTT (k_{max}) is given by

$$k_{\text{max}} = \frac{2\pi}{d_A(z) \theta_{\text{res}}}. \quad (4.15)$$

Note that every super-pixel can be observed simultaneously and so τ for a super-pixel is the total time that the FFTT observes a given patch of the sky. The Fisher integral takes place over a super-pixel and we take k_{max} corresponding to the angular resolution of the survey. The minimum wavenumber probed is taken to be several

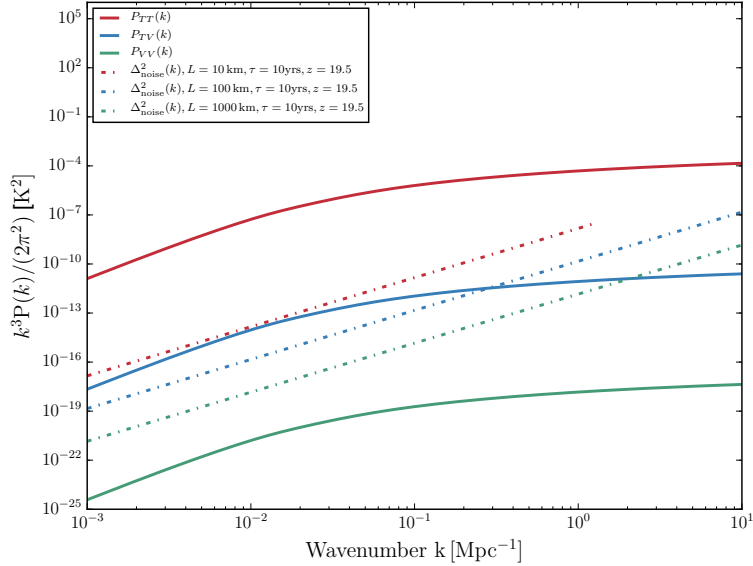


Figure 4.5: Temperature, circular polarization, and noise power spectra relevant to the Fisher calculation. We compute the power-spectra for observations corresponding to $z = 19.5$. Noise power-spectra for two different configurations of FFTTs are shown.

orders of magnitude smaller than k_{max} (the Fisher integral is not sensitive to the choice of k_{min}).

To estimate the Fisher integral we plot the relevant power spectra in Eq. (4.11), including the noise power spectrum for different configurations of the FFTT in Fig. 4.5. From the figure we note that $P_{TT}(k) \gg N_{TT}(k)$ and $N_{VV}(k) \gg P_{VV}(k)$. The Fisher integral in Eq. (4.11) can then be approximated to give

$$w_1 = \frac{1}{(2\pi)^3} \frac{\left(8.6 \text{ mK} \left(\frac{1+z}{20}\right)^2 \left(1 - \frac{T_y}{T_s}\right) \left(\frac{T_y}{T_s}\right)\right)^2}{N_{VV}(1 + 0.75\tilde{x}_\alpha)^2(1 + \tilde{x}_c + \tilde{x}_\alpha)^2} \times \int_{k_{min}}^{k_{max}} d^3k (\Im(Y_{21}(\theta, \phi)))^2 P_\delta(k) \quad (4.16)$$

and

$$w_2 = \frac{2}{(2\pi)^3} \frac{\left(8.6 \text{ mK} \left(\frac{1+z}{20}\right)^2 \left(1 - \frac{T_y}{T_s}\right) \left(\frac{T_y}{T_s}\right)\right)^2}{N_{VV}(1 + 0.75\tilde{x}_\alpha)^2(1 + \tilde{x}_c + \tilde{x}_\alpha)^2} \times \int_{k_{min}}^{k_{max}} d^3k (\Im(Y_{22}(\theta, \phi)))^2 P_\delta(k). \quad (4.17)$$

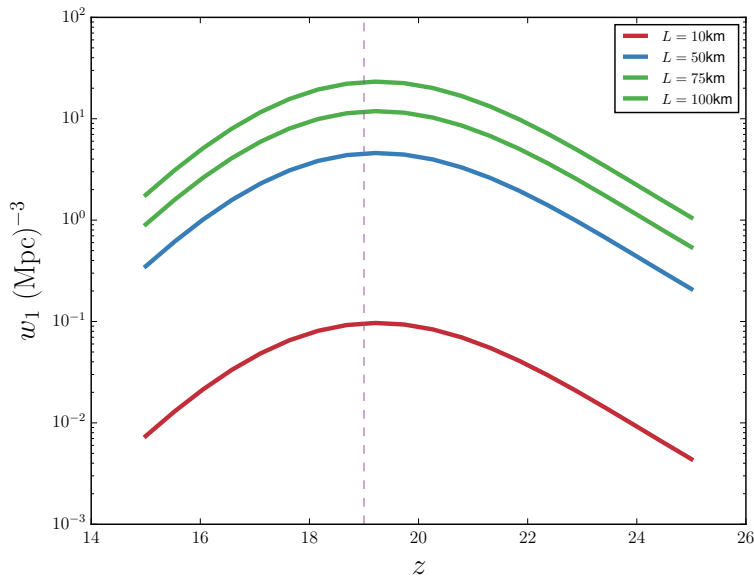


Figure 4.6: Elements of the Fisher matrix w_1 as a function of redshift z , computed for a model of reionization described in the text. For our fiducial model, both w_1 and w_2 peak at $z = 19.5$, i.e. the redshift where the Lyman-alpha coupling becomes efficient ($\tilde{\chi}_\alpha \sim 1$).

The value of w_1 and w_2 is a function of redshift and depends on the reionization and spin-excitation history of the universe during the pre-reionization era. In particular it is sensitive to the Lyman- α flux during this epoch which is unconstrained by observations. We use the fiducial model shown in Fig. 4.4 and described in Ref. Gluscevic et al. 2017. As seen from the figure, for our fiducial model, w_1 and w_2 peak around $z = 19.5$ and our technique is most sensitive in this redshift range. Note that this is likely to change when the Lyman- α flux in the pre-reionization era becomes better constrained.

4.5 Power spectrum of the remote CMB quadrupole and sensitivity to the tensor-to-scalar ratio

We now consider how well we can measure the tensor-to-scalar ratio using remote quadrupole measurements. This requires us to consider the remote quadrupole moments as a statistical field, compute their power spectrum, compare this to the noise computed in §4.4, and finally perform the Fisher matrix sum over modes.

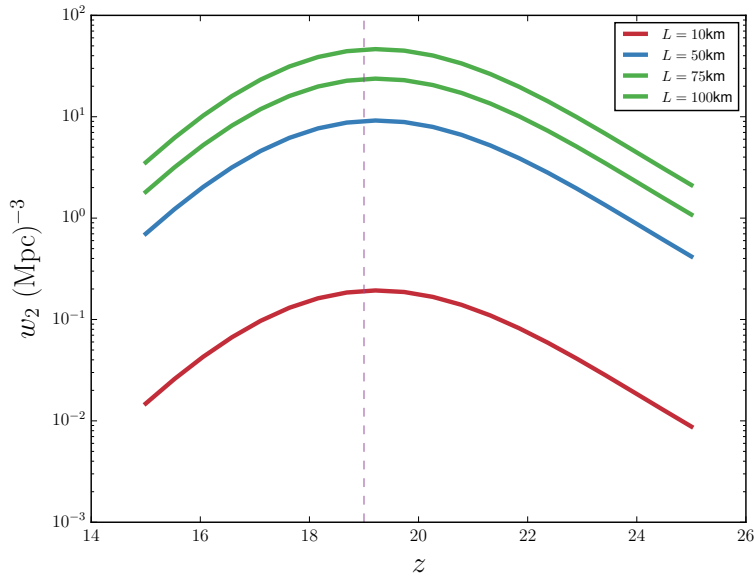


Figure 4.7: Elements of the Fisher matrix w_2 as a function of redshift z , computed for a model of reionization described in the text. For our fiducial model, both w_1 and w_2 peak at $z = 19.5$, i.e. the redshift where the Lyman-alpha coupling becomes efficient ($\tilde{\chi}_\alpha \sim 1$).

***E*- and *B*-mode decomposition of remote CMB quadrupoles**

The “derived data product” from the analysis of §4.4 is a map of the CMB quadrupole moments a_{2q} ($q \neq 0$: we use q here instead of m to avoid confusion below) in each super-pixel of comoving volume \mathcal{V}_c . These moments are measured with respect to the local coordinate basis vectors $\{\hat{e}_\theta, \hat{e}_\phi, \hat{\mathbf{n}} = \hat{e}_r\}$. This quadrupole is derived from the local power spectrum $P_{TV}(\mathbf{k})$ in each super-pixel. Viewed from the perspective of the observer, a_{2q}^* is a spin-weight q field. In analogy to the decomposition of the CMB polarization field Zaldarriaga & Seljak 1997, we may perform a spin-weighted spherical harmonic transformation:

$$a_{2q}^*(\chi, \hat{\mathbf{n}}) = \sum_{\ell=|q|}^{\infty} \sum_{m=-\ell}^{\ell} b_{q\ell m}(\chi) {}_q Y_{\ell m}(\hat{\mathbf{n}}). \quad (4.18)$$

The dependence on comoving distance χ is retained since we do not decompose the radial direction into eigenmodes. The symmetry property $a_{2,-q}(\chi, \hat{\mathbf{n}}) = (-1)^q a_{2q}^*(\chi, \hat{\mathbf{n}})$ implies that

$$b_{q\ell m}^*(\chi) = (-1)^m b_{-q,\ell,-m}(\chi). \quad (4.19)$$

Furthermore, parity inversion results in the transformation $a_{2q}(\chi, \hat{n}) \rightarrow a_{2,-q}(\chi, -\hat{n})$, or equivalently $b_{qlm}(\chi) \rightarrow (-1)^l b_{-q,lm}(\chi)$. We now define the electric and magnetic-parity versions of these quadrupole moments: for $q > 0$,

$$\begin{aligned} b_{\ell m}^{E,q}(\chi) &= \frac{1}{2}[b_{qlm}(\chi) + b_{-q,lm}(\chi)] \quad \text{and} \\ b_{\ell m}^{B,q}(\chi) &= \frac{1}{2i}[b_{qlm}(\chi) - b_{-q,lm}(\chi)]. \end{aligned} \quad (4.20)$$

These moments obey the same complex conjugation properties as usual electric and magnetic moments, i.e. $b_{\ell m}^{E,q*}(\chi) = (-1)^m b_{\ell,-m}^{E,q}(\chi)$ and $b_{\ell m}^{B,q*}(\chi) = (-1)^m b_{\ell,-m}^{B,q}(\chi)$. Under parity inversion, $b_{\ell m}^{E,q}(\chi)$ picks up a factor of $(-1)^\ell$, whereas $b_{\ell m}^{B,q}(\chi)$ picks up a factor of $-(-1)^\ell$.

The statistics of the CMB quadrupole moment fields can thus be described in terms of the cross-power spectra of these fields at the various comoving distances, e.g.

$$C_\ell^{B1,B2}(\chi, \chi') = \langle b_{\ell m}^{B1*}(\chi) b_{\ell m}^{B2}(\chi') \rangle. \quad (4.21)$$

Parity considerations imply a vanishing cross-spectrum between the E, q and B, q' moments. Furthermore, there is no primordial scalar contribution to the $B1$ or $B2$ moments.

***B*-mode power spectrum of the remote CMB quadrupole**

We compute the power spectrum of the remote CMB quadrupole by the standard method – that is, we consider first a single Fourier mode (a plane primordial gravitational wave) with wave vector along the z -axis, then rotate it to an arbitrary angle, and finally perform a stochastic average using the power spectrum in the initial conditions.

Consider a gravitational wave with wave number K and strain h_R propagating in the z -direction and with right-circular polarization, i.e. with metric

$$g_{\mu\nu} = a^2 \begin{pmatrix} -1 & 0 & 0 & 0 \\ 0 & 1 + \frac{1}{\sqrt{2}} h_R e^{iKx^3} & \frac{1}{\sqrt{2}} i h_R e^{iKx^3} & 0 \\ 0 & \frac{1}{\sqrt{2}} i h_R e^{iKx^3} & 1 - \frac{1}{\sqrt{2}} h_R e^{iKx^3} & 0 \\ 0 & 0 & 0 & 1 \end{pmatrix}. \quad (4.22)$$

The normalization is chosen to coincide with the common normalization of tensor perturbations (e.g. Baumann 2009) with $r = \Delta_h^2(k)/\Delta_\zeta^2(k) = 16\epsilon$ in slow-roll single-field inflation. This plane gravitational wave leads to a tensor $\ell = 2$ CMB multipole

moment

$$\frac{\Delta T(\mathbf{r}, \hat{\mathbf{p}}, \eta)}{\bar{T}} = h_{\text{R}0} e^{iKx^3} \sum_{\ell=2}^{\infty} (-i)^\ell \sqrt{\frac{4\pi}{2\ell+1}} \Theta_\ell^{\text{T}}(\eta) Y_{\ell 2}(\hat{\mathbf{p}}), \quad (4.23)$$

at position \mathbf{r} , for photons traveling in direction $\hat{\mathbf{p}}$, and at conformal time η defined as,

$$\eta(z) = \int_0^{t(z)} \frac{dt}{a} \quad (4.24)$$

Θ_ℓ^{T} are the tensor multipole moments generated by a unit-amplitude gravitational wave and $h_{\text{R}0}$ is the initial amplitude. Rotational symmetry guarantees that only $m = 2$ terms exist in the sum over spherical harmonics. The $\ell = 2$ multipole moments measured at some position on the sky and some comoving distance $\chi(z)$ are then

$$a_{2m}(\chi, \hat{\mathbf{n}}) = -\sqrt{\frac{4\pi}{5}} h_{\text{R}0} e^{iK\chi \cos \theta} \Theta_2^{\text{T}}(\eta_0 - \chi) \times [\mathcal{D}_2(\phi, \theta, 0)]_{m,2}, \quad (4.25)$$

where $\mathcal{D}_2(\phi, \theta, 0)$ is the passive rotation matrix associated with rotating the reference frame for the multipoles from $\{\hat{\mathbf{e}}_1, \hat{\mathbf{e}}_2, \hat{\mathbf{e}}_3\}$ to $\{\hat{\mathbf{e}}_\theta, \hat{\mathbf{e}}_\phi, \hat{\mathbf{n}}\}$.

The $\ell = 2$ multipole moments from Eqn.(4.25) can be re-written in terms of the spin-weighted spherical harmonics,

$$a_{2q}^*(\chi, \hat{\mathbf{n}}) = -\frac{4\pi}{5} h_{\text{R}0} e^{-iK\chi \cos \theta} \Theta_2^{\text{T}*}(\eta_0 - \chi) {}_q Y_{2,-2}(\hat{\mathbf{n}}). \quad (4.26)$$

The solution for $b_{q\ell m}(\chi)$ can then be written as

$$\begin{aligned} b_{q\ell m}(\chi) &= \int a_{2q}^*(\chi, \hat{\mathbf{n}}) {}_q Y_{\ell m}^*(\hat{\mathbf{n}}) d^2 \hat{\mathbf{n}} \\ &= -\frac{4\pi}{5} h_{\text{R}0} \Theta_2^{\text{T}*}(\eta_0 - \chi) \int e^{-iK\chi \cos \theta} {}_q Y_{2,-2}(\hat{\mathbf{n}}) {}_q Y_{\ell m}^*(\hat{\mathbf{n}}) d^2 \hat{\mathbf{n}} \\ &= -\frac{(4\pi)^{3/2}}{5} h_{\text{R}0} \Theta_2^{\text{T}*}(\eta_0 - \chi) \delta_{m,-2} \sum_{\ell'=0}^{\infty} \sqrt{2\ell'+1} (-i)^{\ell'} j_{\ell'}(K\chi) \\ &\quad \int {}_0 Y_{\ell' 0}(\hat{\mathbf{n}}) {}_q Y_{2,-2}(\hat{\mathbf{n}}) {}_q Y_{\ell,-2}^*(\hat{\mathbf{n}}) d^2 \hat{\mathbf{n}} \\ &= -4\pi \sqrt{\frac{2\ell+1}{5}} (-1)^q h_{\text{R}0} \Theta_2^{\text{T}*}(\eta_0 - \chi) \delta_{m,-2} \\ &\quad \sum_{\ell'=0}^{\infty} (2\ell'+1) (-i)^{\ell'} j_{\ell'}(K\chi) \begin{pmatrix} \ell' & 2 & \ell \\ 0 & q & -q \end{pmatrix} \begin{pmatrix} \ell' & 2 & \ell \\ 0 & -2 & 2 \end{pmatrix}. \quad (4.27) \end{aligned}$$

Under the transformation $q \leftrightarrow -q$, this changes sign if $\ell' - \ell$ is odd and remains the same if $\ell' - \ell$ is even; thus for the B -mode, only the $\ell' - \ell$ odd terms contribute (see

Eq. 4.20). The triangle inequality restricts $|\ell' - \ell| \leq 2$, so the sum then reduces to $\ell' = \ell \pm 1$. Substituting in the Wigner $3j$ symbols yields for $q > 0$:

$$b_{q\ell m}^B(\chi) = -\frac{2\pi (-i)^\ell \delta_{m,-2}}{\sqrt{5(2\ell+1)}} h_{\text{R0}} \Theta_2^{\text{T}*}(\eta_0 - \chi) \left[(-1)^q \sqrt{(\ell+2)(\ell+\bar{q})} j_{\ell-1}(K\chi) - \sqrt{(\ell-1)(\ell+1-\bar{q})} j_{\ell+1}(K\chi) \right] \quad (4.28)$$

where we have defined $\bar{q} \equiv (-1)^q q$. Use of the rules for combining spherical Bessel functions Abramowitz & Stegun 1972 allows the further simplifications:

$$b_{q\ell m}^B(\chi) = -2\pi \frac{\delta_{m,-2}}{i^\ell} \sqrt{\frac{2\ell+1}{5}} h_{\text{R0}} \Theta_2^{\text{T}*}(\eta_0 - \chi) f_{q\ell}(K\chi), \quad (4.29)$$

where we have defined the functions

$$f_{1\ell}(x) = \sqrt{(\ell-1)(\ell+2)} \frac{j_\ell(x)}{x} \quad (4.30)$$

and

$$f_{2\ell}(x) = j'_\ell(x) + 2 \frac{j_\ell(x)}{x}. \quad (4.31)$$

These functions are always real, and we have $f_{11}(x) = 0$.

It remains to express the B -mode power spectrum of the remote quadrupole components. This requires us to obtain the product of two $b_{q\ell m}^B(\chi)$ s and average over the direction of the plane wave; this is equivalent to summing over m and dividing by $2\ell+1$. Thus for a plane wave in a random direction, we find

$$\begin{aligned} C_\ell^{Bq,Bq'}(\chi, \chi') &= \frac{1}{2\ell+1} \sum_{m=-\ell}^{\ell} \langle b_{q\ell m}^{B*}(\chi) b_{q'\ell m}^B(\chi') \rangle \\ &= \frac{4\pi^2}{5} |h_{\text{R0}}|^2 \Theta_2^{\text{T}}(\eta_0 - \chi) \Theta_2^{\text{T}*}(\eta_0 - \chi') \\ &\quad \times f_{q\ell}(K\chi) f_{q'\ell}(K\chi'). \end{aligned} \quad (4.32)$$

If we finally replace the plane wave with a statistical distribution of gravitational waves, we find

$$\begin{aligned} C_\ell^{Bq,Bq'}(\chi, \chi') &= \frac{8\pi^2}{5} \int_0^\infty \Theta_2^{\text{T}}(\eta_0 - \chi) \Theta_2^{\text{T}*}(\eta_0 - \chi') \\ &\quad \times f_{q\ell}(K\chi) f_{q'\ell}(K\chi') \Delta_h^2(K) \frac{dK}{K}, \end{aligned} \quad (4.33)$$

where $\Delta_h^2(K)$ is the contribution to the variance of the strain per logarithmic range of K (i.e. $d\text{Var}h/d\ln K$) per gravitational wave polarization (right or left). A

factor of 2 has been inserted to account for the existence of two gravitational wave polarizations.

Note that although the spherical harmonic decomposition of a spin-1 field admits an $\ell = 1$ component, the $q = 1$ B -mode of the remote quadrupole vanishes – i.e. $C_\ell^{B1,B1}(\chi, \chi') = 0$ – because $f_{11}(x) = 0$. This is mathematically expected because there is no $\ell = 1$ gravitational wave mode.

Incorporation of the tensor transfer function

We now also need the tensor transfer function $\Theta_2^T(\eta)$. Fortunately, in the matter-dominated era, well after recombination, there is an analytic solution for this. The strain amplitude has the simple time dependence

$$h_R(\eta) = h_{R0} \frac{3j_1(K\eta)}{K\eta}. \quad (4.34)$$

The tensor transfer function is then given by evaluating the temperature quadrupole at the origin at time η using the line-of-sight expression for the photon temperature perturbation Seljak & Zaldarriaga 1996; Hu & White 1997; in what follows, we assume the temperature perturbation due to the gravitational wave is built up from the time of recombination η_* to the time η in question. We work in terms of the real-space temperature perturbation $\Theta(\mu', \phi')$, where $\mu' = \cos \theta'$ is the direction cosine of the photon's trajectory:

$$\begin{aligned} \Theta_2^T(\eta) &= -\frac{5\sqrt{6}}{16\pi h_{R0}} \int (1 - \mu'^2) e^{-2i\phi'} \Theta(\mu', \phi') d\mu' d\phi' \\ &= -\frac{5\sqrt{6}}{16\pi h_{R0}} \int (1 - \mu'^2) e^{-2i\phi'} \left[\int_{\eta_*}^{\eta} (1 - \mu'^2) e^{2i\phi'} \right. \\ &\quad \left. \times \frac{-\dot{h}_R(\eta')}{2\sqrt{2}} e^{iK\mu'(\eta' - \eta)} d\eta' \right] d\mu' d\phi' \\ &= \frac{5\sqrt{3}}{16h_{R0}} \int_{\eta_*}^{\eta} \left[\int_{-1}^1 (1 - \mu'^2)^2 e^{iK\mu'(\eta' - \eta)} d\mu' \right] \dot{h}_R(\eta') d\eta' \\ &= \frac{5\sqrt{3}}{16h_{R0}} \int_{\eta_*}^{\eta} \frac{16j_2(K(\eta - \eta'))}{[K(\eta - \eta')]^2} \dot{h}_R(\eta') d\eta' \\ &= \frac{5\sqrt{3}}{16h_{R0}} \int_{\eta_*}^{\eta} \frac{16j_2(K(\eta - \eta'))}{[K(\eta - \eta')]^2} h_{R0} \frac{-3j_2(K\eta')}{\eta'} d\eta' \\ &= -15\sqrt{3} \int_{\eta_*}^{\eta} \frac{j_2(K(\eta - \eta')) j_2(K\eta')}{K^2(\eta - \eta')^2 \eta'} d\eta'. \end{aligned} \quad (4.35)$$

Equation (4.35) is an integral form for the tensor transfer function; it is straightforward to compute. With the help of Eq. (4.33), the general remote quadrupole B -mode power spectrum for tensors can be obtained.

Sensitivity to tensor-to-scalar ratio

The uncertainty in the tensor-to-scalar ratio can be forecast using Fisher matrix techniques. In general, if there is a Gaussian-distributed data vector \mathbf{d} with covariance \mathbf{C} , then the Fisher approximation for the uncertainty in the tensor-to-scalar ratio r is

$$\sigma_r^{-2} = \frac{1}{2} \text{Tr} \left(\mathbf{C}^{-1} \frac{\partial \mathbf{C}}{\partial r} \mathbf{C}^{-1} \frac{\partial \mathbf{C}}{\partial r} \right). \quad (4.36)$$

In our case, we will write as the data vector \mathbf{d} the sequence of B -mode moments $b_{\ell m}^{Bq}(\chi)$: up to some ℓ_{\max} , the number of such moments is $N_d = 2N_z(\ell_{\max}^2 - 4)$, where N_z is the number of redshift slices and $\ell_{\max}^2 - 4 = \sum_{\ell=2}^{\ell_{\max}} (2\ell + 1)$ is the number of multipoles. In harmonic space, for uniform full-sky coverage, \mathbf{C} is thus an $N_d \times N_d$ matrix that is block-diagonal with $2N_z \times 2N_z$ blocks; the block corresponding to multipole ℓ will be denoted $\mathbf{C}_{(\ell)}$ and is repeated $2\ell + 1$ times. We may thus write Eq. (4.36) as

$$\sigma_r^{-2} = \frac{f_{\text{deg}}^2}{2} \sum_{\ell=2}^{\ell_{\max}} (2\ell + 1) \text{Tr} \left[\mathbf{C}_{(\ell)}^{-1} \frac{\partial \mathbf{C}_{(\ell)}}{\partial r} \mathbf{C}_{(\ell)}^{-1} \frac{\partial \mathbf{C}_{(\ell)}}{\partial r} \right]. \quad (4.37)$$

Here f_{deg} is a degradation factor due to reduced sky coverage. In CMB forecasts, it is often assumed that the information content scales with the sky coverage f_{sky} , in which case $f_{\text{deg}} = f_{\text{sky}}^{1/2}$. This is only an approximation however Knox 1997 and is generally valid only for sky coverage $\Delta\theta \geq 2\pi/\Delta\ell$, where $\Delta\ell$ is the width of the features in ℓ -space under consideration. Since the B -mode spectrum peaks at the largest scales, this is only marginally true; forecasts for the reionization B -mode that evaluate the cut-sky matrix inversion have shown a factor $f_{\text{deg}} \sim f_{\text{sky}}^2$ for Galactic Plane cuts with $f_{\text{sky}} > 0.7$ Amarie et al. 2005. In this paper, we consider only observations of the full sky minus the Galactic Plane with an assumed $f_{\text{deg}} = 0.5$, and stress that Eq. (4.37) for σ_r is uncertain at the factor of ~ 2 level even for this case.

The matrix $\mathbf{C}_{(\ell)}$ can be broken up into signal $\mathbf{S}_{(\ell)}$ and noise $\mathbf{N}_{(\ell)}$. The noise power spectrum is diagonal in z -space:

$$N_{(\ell)qz,q'z'} = \frac{1}{w_q [\chi(z)]^2 \Delta\chi} \delta_{qq'} \delta_{zz'}, \quad (4.38)$$

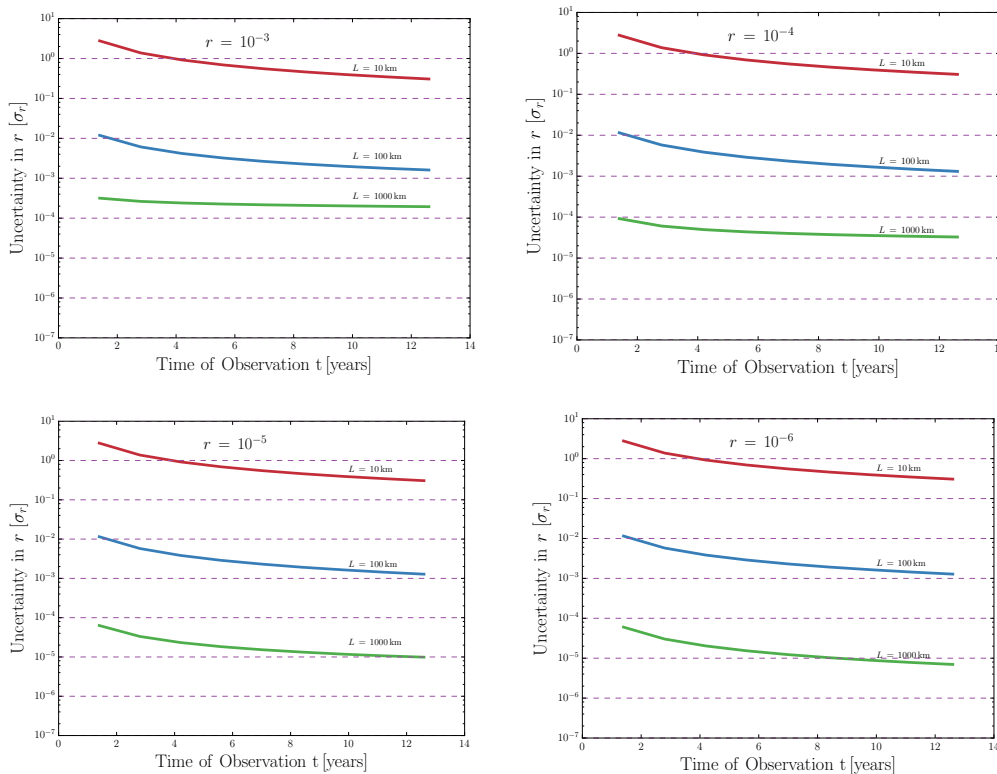


Figure 4.8: Forecasts for σ_r for different FFTT telescope configurations. The parameters used to make these forecasts are described in Fig. 4.4 & 4.3 and in Section 4.4. For the given Lyman- α flux model the values of weights w_1 and w_2 peak around $z \sim 19.5$ as shown in Fig. 4.7. For our forecasts we consider a shell with $z_{min} = 18$ and $z_{max} = 23$. Note that the live observation time quoted here will be shorter than the wall-clock time of the survey.

where $\Delta\chi = c\Delta z/H(z)$ is the width of the redshift slice and $\chi(z)$ is the comoving distance. (The denominator is the conversion from sr on the sky to Mpc^3 of comoving volume). The signal matrix is

$$S_{(\ell)qz,q'z'} = C_\ell^{Bq,Bq'} [\chi(z), \chi(z')], \quad (4.39)$$

which is proportional to the tensor-to-scalar ratio r . We thus have $\partial C_{(\ell)}/\partial r = S_{(\ell)}/r$, which is independent of r .

Finally, we need the relation between $\Delta_h^2(k)$ and r . This is

$$\Delta_h^2(k) = r\Delta_\zeta^2(k) = 2.4 \times 10^{-9}r. \quad (4.40)$$

In Fig. 4.8, we plot the forecasts for σ_r for different fiducial values of r , for different FFTT configurations. We choose the pre-reionization Lyman- α flux model

described in Sec. 4.4; for this fiducial model the values of w_1 and w_2 peak around $z \sim 19.5$. The observation time τ entering the expression for noise in Eq. (4.13) is the time for observing a given portion of the sky that is above the horizon of a given location. We note that this is different from the *total live observation time* t_{obs} which is longer than τ . Here t_{obs} is longer by a factor equal to the fraction of the day that a given survey region is above the horizon and is related to τ via

$$t_{\text{obs}} = \tau \frac{\Omega_{\text{total}}}{\Omega_{\text{instant}}}. \quad (4.41)$$

A FFTT can in principle observe the entire sky above the horizon at a given instant, corresponding to $\Omega_{\text{instant}} = 2\pi \text{sr}$. However, the image quality degrades near the horizon and the effective $\Omega_{\text{instant}} = \pi \text{sr}$. For $f_{\text{sky}} \sim 0.7$ the corresponding $\Omega_{\text{total}} = 2.8\pi \text{sr}$ (note that achieving this f_{sky} will need two experiments – one in the northern and one in the southern hemisphere). Fig. 4.8 shows our forecasts in terms of the observation time t_{obs} . We note that there is a third time-scale in our experiments which is the wall-clock time. Practically, an experiment is unlikely to be on-line for the entirety of a survey, and wall-clock time will thus be longer than t_{obs} . The wall-clock time determines the total duration of a survey.

4.6 Foregrounds

Foreground contamination by Galactic and extragalactic sources poses the most serious challenge to detecting the cosmological 21 cm temperature and circular polarization signals. Broadband Galactic and extragalactic foregrounds at low-frequencies are expected to be approximately four orders of magnitude larger than the cosmological temperature signal, and their removal has been the subject of extensive study. Broadly, the approaches for foreground removal involve using both the angular structure of foregrounds, and the spectral smoothness of synchrotron and free-free radiation (as compared to the highly structured cosmological signal) to distinguish them from the cosmological signal (Di Matteo et al. 2002; Di Matteo et al. 2004; Zaldarriaga et al. 2004; Oh & Mack 2003; Liu & Tegmark 2012).

Linear polarization of the redshifted 21cm radiation has been examined by Babich & Loeb 2005. They considered the intrinsic polarization of the 21 cm line due to Thomson scattering during reionization, leading to a 21 cm E -mode signal. This signal is expected to be completely scrambled up by Faraday rotation, although De & Tashiro 2014 concluded that extremely accurate Galactic rotation measure maps might allow one to reconstruct the intrinsic linear polarization signal.

Circularly polarized foregrounds at low-frequencies, relevant for our technique, are not as well-understood. King & Lubin 2016 created foreground maps of circular polarization induced by Galactic magnetic fields in the GHz frequency range (relevant for CMB observations) and more recently (Enßlin et al. 2017) have created predicted Galactic circular polarization maps based on synchrotron templates at 408 MHz (see also Oppermann et al. 2012). In this section we examine potential foregrounds that could contaminate the measurement of the cosmological 21 cm circular polarization signal relevant to our method.

There are two broad mechanisms that can contaminate the cosmological circular polarization signal: the intrinsic circular polarization of galactic or extragalactic foreground sources, and that generated during propagation through the interstellar/intergalactic medium. The former is expected to be spectrally smooth and could potentially be removed using spectral smoothness arguments described earlier. The circular polarization induced due to propagation effects can lead of confusion with the cosmic signal, since it depends on the spatial structure of the ISM/IGM, and may have a complicated frequency dependence due to Faraday rotation. As such, it is important to estimate the amplitude and approximate angular structure of these foregrounds in order to assess the feasibility of our technique.

Circularly polarized foregrounds could in principle spoil our measurement in one of two ways. One would be if the circularly polarized foregrounds were correlated with the total intensity with a quadrupolar spatial/spectral pattern such as to mimic a cosmological signal. We discuss in each case whether we expect this to be an issue. The other would be if the circularly polarized foregrounds did not have such a pattern, but were so bright as to effectively add noise to the measured TV correlation and prevent the remote CMB quadrupole estimator from reaching the theoretical thermal noise limit. We can understand this “foreground noise” problem if we consider the TV cross spectrum as a function of wavenumber,

$$\Delta_{TV}^2(k) \equiv \frac{k^3}{2\pi^2} P_{TV}(k), \quad (4.42)$$

and recall its uncertainty:

$$\sigma[\Delta_{TV}^2(k)] = \sqrt{\frac{1}{N_{\text{modes}}} \Delta_{TT,\text{tot}}^2(k) \Delta_{VV,\text{tot}}^2(k)}, \quad (4.43)$$

where N_{modes} is the number of modes probed, and $\Delta_{VV,\text{tot}}^2(k)$ is the sum of the intrinsic cosmological signal $\Delta_{VV,\text{cosmo}}^2(k)$, the instrument noise $\Delta_{VV,\text{noise}}^2(k)$, and

the foregrounds $\Delta_{\text{fore}}^2(k)$. We have assumed here that the foregrounds for 21 cm temperature have been successfully removed using techniques described in the literature. As discussed in Section 4.4, $\Delta_{VV,\text{noise}}^2(k) \approx \Delta_{TT,\text{noise}}^2(k)$ and from Figure 4.5 we see that $\Delta_{VV,\text{noise}}^2(k) \gg \Delta_{VV}^2(k)$. Hence the “foreground noise” contribution to $\sigma[\Delta_{TV}^2(k)]$ depends on the relative magnitude of $\Delta_{VV,\text{fore}}^2(k)$ and $\Delta_{VV,\text{noise}}^2(k)$.

In this section we make order-of-magnitude estimates of $\Delta_{VV,\text{fore}}^2(k)$ due to the synchrotron emission from the galaxy and extragalactic point sources. These foregrounds turn out to be the dominant foregrounds but we argue that they can be removed because of their spectral smoothness in frequency space. We also estimate $\Delta_{VV,\text{fore}}^2(k)$ due to propagation effects through the ISM. These foregrounds are expected to have features correlated to structures in the ISM and are not spectrally smooth. However, we show that these foregrounds are not likely to be important for our proposed method.

Spectrally Smooth Circular Polarization from Synchrotron

The synchrotron radiation from ultra-relativistic electrons in the interstellar medium is the strongest source of foregrounds at low-frequencies (Haslam et al. 1982). It is strongly linearly polarized. At low frequencies in *linear* polarization, even a spatially smooth signal is mixed to small angular scales by Faraday rotation, leading to typical fluctuating signals of a few Kelvin. This signal has been constrained or observed with many instruments at frequencies < 200 MHz (Bernardi et al. 2009; Pen et al. 2009; Bernardi et al. 2013; Jelić et al. 2014; Moore et al. 2015; Jelić et al. 2015). In both cases the limits on the Stokes I parameter were $\Delta_I \lesssim 10$ K over the range of angular scales probed. (The spatially smooth component can be much brighter.)

Synchrotron radiation is expected to have a small fraction of circularly polarization. The circular polarization in synchrotron radio emission has been observed in quasars (Roberts et al. 1975), AGNs (Wardle et al. 1998; Homan & Wardle 1999), and the galactic center (Sault & Macquart 1999). While the degree of circular polarization in these sources is not completely well-understood, it is believed to arise from a combination of intrinsic circular polarization of synchrotron radiation and propagation effects in a plasma (Macquart & Melrose 2000).

The degree of circular polarization of Galactic synchrotron has not yet been measured, but we can make rough estimates of the strength of this foreground using measured limits on the Stokes I parameter. For an electron with Lorentz factor γ

gyrating around a field line at an angle θ to the line of sight, the degree of circular polarization observed, to the first order in γ (Legg & Westfold 1968; de Búrca & Shearer 2015),

$$\frac{V}{I} \approx \cot \theta \left(\frac{\nu_g}{\nu} \right)^{1/2} \approx \gamma^{-1} \cot \theta \quad (4.44)$$

where $\nu_g = (eB)/(2\pi\gamma m_e c)$ is the gyromagnetic frequency.

The typical Lorentz factor of relativistic electrons that lead to synchrotron radiation in the frequency range $\nu_{\text{radio}} \sim 50 - 150\text{MHz}$ is

$$\gamma = \sqrt{\frac{2\pi m_e c \nu_{\text{radio}}}{e B_{\text{gal}}}} \sim 1000, \quad (4.45)$$

where we take the typical magnetic field in the ISM to be $B_{\text{gal}} \sim 1\mu\text{G}$.

Since $\Delta_I \lesssim 10\text{K}$, the typical circular polarization signal from relativistic electrons in the galaxy is expected to be $\Delta_V \approx 0.01\text{K}$ in temperature units, and the typical value of $\Delta_{VV,\text{sync}}^2(k) \approx 10^{-4}\text{K}^2$.

As seen in Fig. 4.9, $\Delta_{VV,\text{sync}}^2(k)$ is many orders of magnitude larger than $\Delta_{VV,\text{noise}}^2(k)$, and is the most dominant foreground for our method. Moreover, since the sign of the TV correlation depends on the direction of the magnetic field (toward or away from the observer), and the Galactic magnetic field has a large-scale coherent component, we expect significant TV correlations even averaged over a patch of many tens of degrees. However, this synchrotron circular polarization signal is spectrally smooth and hence the same foreground removal techniques applied to total intensity should be applicable Liu & Tegmark 2012. In particular, it is confined to modes with $k_{\parallel} \approx 0$.

Circular Polarization Foregrounds from Faraday Rotation

Faraday rotation of linearly polarized light through a closed plasma interconverts Q and U Stokes parameters but does not lead to generation of Stokes V , to the first order in the galactic magnetic field B_{gal} . However, in the next order in B_{gal} , Faraday rotation can lead to an "leaking" of Stokes Q and U to produce Stokes V .

The Galactic synchrotron radiation is expected to have a high degree of linear polarization and the leakage of power from Stokes Q and U to V , due to propagation through the cold plasma in the ISM can result in a CP foreground. Unlike the intrinsic CP signal discussed in Section 4.6, this signal is not smooth in frequency space. The signal is expected to trace structures in the ISM and, if it has significant amplitude,

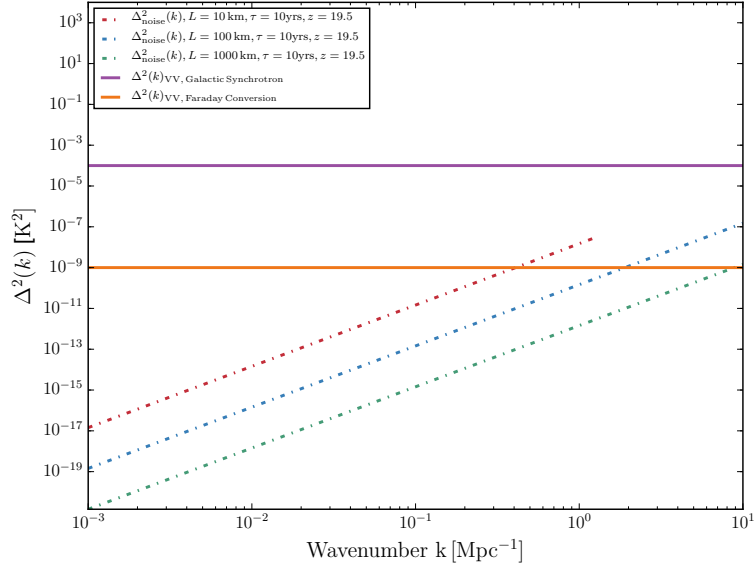


Figure 4.9: Order of magnitude of expected foregrounds for the circular polarization signal from Galactic synchrotron (purple line) and due to Faraday rotation through the ISM (orange line) compared against the noise power spectra expected for for three different configurations of FFTTs.

can potentially mimic the cosmological signal. In this section we estimate the angular power spectrum of the CP signal due to propagation effects in the Galaxy.

Consider the polarization of radiation that is propagating through a cold plasma. The transfer equation for the radiation propagating along the z direction is given by

$$\begin{aligned}
 \frac{dQ}{dz} &= -2\frac{\omega}{c}[n_U V - n_V U], \\
 \frac{dU}{dz} &= -2\frac{\omega}{c}[n_V Q - n_Q V], \quad \text{and} \\
 \frac{dV}{dz} &= 2\frac{\omega}{c}[n_U Q - n_Q U],
 \end{aligned} \tag{4.46}$$

where n_U , n_Q , and n_V are the real anti-symmetric components of the refractive index tensor n_{ij} and are given by

$$\begin{aligned}
 n_U &= -\frac{\pi n_e e^2}{m_e \omega^2} \left(\frac{e}{m_e \omega c} \right)^2 2B_x B_y, \\
 n_Q &= -\frac{\pi n_e e^2}{m_e \omega^2} \left(\frac{e}{m_e \omega c} \right)^2 (B_y^2 - B_x^2), \quad \text{and} \\
 n_V &= \frac{\pi n_e e^2}{m_e \omega^2} \frac{e}{m_e \omega c} B_z.
 \end{aligned} \tag{4.47}$$

The circular polarization produced by propagation through a medium is then the integral

$$V = \int \frac{2\omega}{c}(n_Q U - n_U Q) dz. \quad (4.48)$$

To estimate the order of magnitude of V , we need estimates of the birefringence coefficients (n_Q, n_U); the linear polarization (Q, U); the path length through the ISM; and the coherence length z_{coh} over which the integrand retains the same sign. The birefringence coefficients are from Eq. (4.47); this implies

$$\Delta_{VV, \text{Faraday}}^2 \sim \left(\frac{4\pi e^4}{m_e^3 \omega^3 c^3} \right)^2 n_e^2 L_{\text{gal}} B^4 z_{\text{coh}} \Delta_{QQ, \text{sync}}^2. \quad (4.49)$$

The coherence length z_{coh} could be set by either de-correlation of (n_Q, n_U) or of (Q, U); the latter occurs on a distance scale of order a Faraday rotation cycle,

$$z_{coh} \sim \frac{c}{2\omega |n_V|} \sim \frac{m_e^2 c^2 \omega^2}{2\pi n_e e^3 B}. \quad (4.50)$$

Plugging this into Eq. (4.49) gives

$$\Delta_{VV, \text{Faraday}}^2 \sim \frac{8\pi e^5 B^3 n_e}{m_e^4 \omega^4 c^4} L_{\text{gal}} \Delta_{QQ, \text{sync}}^2. \quad (4.51)$$

For order-of-magnitude purposes, we take $\Delta_{QQ, \text{sync}}^2 \sim 10 \text{ K}^2$ (the order of magnitude of recent detections or upper limits), a path length of 30 parsecs, a Galactic magnetic field of $B \sim 10^{-5} \text{ G}$, and an electron density $n_e \sim 0.03 \text{ cm}^{-3}$.

This leads us to an estimate of $\Delta_{VV, \text{Faraday}}^2 \approx 10^{-9} \text{ K}^2$. As seen in Fig. 4.9 the circular polarization foreground due to Faraday rotation is much lower than the noise power spectra of the proposed experimental setups. Note that we have not determined the peak angular scale for this foreground; since the Galactic magnetic field and hence (n_Q, n_U) exhibit large-scale coherence, we expect the circular polarization induced by $Q, U \rightarrow V$ conversion to trace the same angular scales as linear polarization.

Since at low frequencies the linear polarization has been rotated through many cycles, we expect a very weak correlation of (Q, U) (and hence V) with the total synchrotron intensity.

Extragalactic Point Sources

After Galactic synchrotron, unresolved, extragalactic point sources are expected to be one of the most challenging foregrounds for 21 cm tomography (Liu et al. 2009; Di Matteo et al. 2004). An interferometer is usually characterized by a

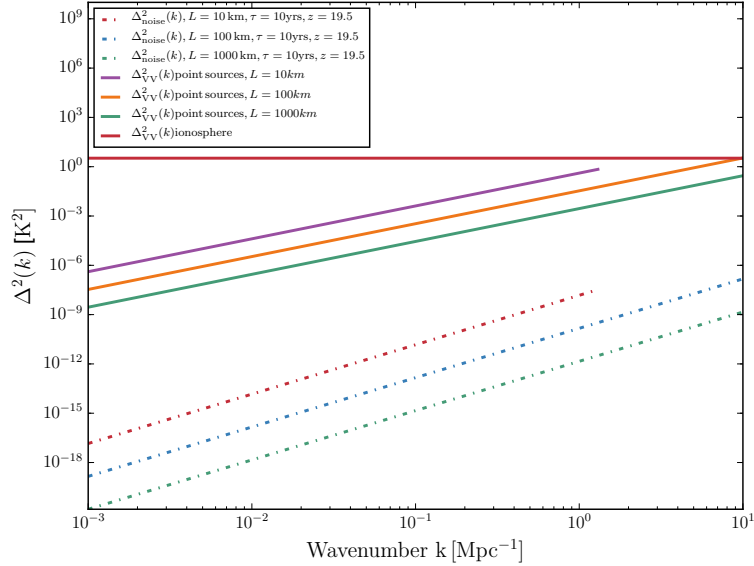


Figure 4.10: Order of magnitude of expected foregrounds for the circular polarization signal from unresolved point sources (blue, green, and purple line) and Faraday rotation due to the ionosphere (orange line) compared against the noise power spectra expected for three different configurations of FFTs.

classical confusion limit, defined as having one source above the threshold flux S_c per m synthesized beams. Then the threshold flux density S_c is defined such that $m \times 1.13 \theta^2 N(S_c) = 1$. Here $N(s)$ is the number density of sources above flux density s and θ is the FWHM of each synthesized beam. Here we assume that $N(s) = As^\beta$ which implies,

$$S_c = (1.13mA)^{-1/\beta} \theta^{-2/\beta} \quad (4.52)$$

Here we consider the classical confusion limit calculated at 74MHz for the VLSS survey which gives $A = 1.14$, $\beta = -1.3$, and $m = 12.9$ as calculated by Cohen (Cohen 2004), and the units of flux are in Jansky and beam size is in degrees.

We can detect and remove point sources of flux S from a survey if the thermal noise of the survey is much less than S and if the source has a flux density much greater than S_c . Sources with flux density less than S_c will lead to a confusion noise even in the limit of infinite integration time. In this section we assume that the resolved point sources have been removed using standard techniques and estimate the noise contribution to $\Delta_{VV,fore}^2(k)$ due to unresolved point sources, for different configurations of FFTs. To estimate the foreground contribution due

to unresolved point sources we need the classical confusion for low-frequency radio experiments. Here we consider the confusion limit calculation based on the VLSS sky survey at 75 MHz Cohen 2004 given by Eq.(4.52). For a FFTT the beam size is $\theta \sim \lambda/L$ where L is the side length. For observations around 68 MHz and for FFTT side lengths of 10, 100, 1000km the beam size corresponds to $\theta = 0.025$, 0.0025 & 0.00025 degrees respectively. The corresponding confusion limits are $S_c = 3 \times 10^{-2}$, 8.6×10^{-4} & 2.5×10^{-5} respectively. The contribution to the temperature power spectrum due to unresolved point sources (flux less than S_c per beam) is

$$\Delta_{\text{TT}}^2 = \frac{l^2}{2\pi} C_l^{\text{TT}} \approx \frac{l^2}{2\pi} \left(\frac{\lambda^2}{2k_{\text{B}}} \right)^2 \int_0^{S_c} S^2 \frac{dN}{dS} dS, \quad (4.53)$$

where Δ_{TT}^2 is the total power per $\log k$, $N(S)$ is the number density of sources above a flux S and $l = k(1+z)D_A(z)$. We use a power law source count function, $N(S) = AS^\alpha$ where $A = 1.14$ and $\alpha = -1.3$ Cohen 2004. The point source foreground at low frequencies is dominated by synchrotron emission from radio-loud galaxies and AGNs Ghosh et al. 2012; Di Matteo et al. 2004; the circular polarization foreground due to the confused background of point sources is given by

$$\Delta_{V\text{V,fore}}^2 \approx \left(\frac{V}{I} \right)^2 \Delta_{\text{TT,fore}}^2. \quad (4.54)$$

The measured circular polarization fraction for typical radio-loud AGNs is $V/I \sim 10^{-4}$ at 4.9 GHz (Rayner et al. 2000). Note that these measurements are dominated by the brightest radio-galaxies while the point sources dominating the foregrounds we are interested in are likely to be much fainter. The fractional circular polarization for blazars are expected to be much higher (e.g. Rayner et al. 2000) but these blazars are not likely to dominate the unresolved point source background.

Assuming the circular polarization of radio galaxies is dominated by synchrotron, the degree of circular polarization at low frequencies (relevant to our estimates) can be determined by scaling $V/I \propto \gamma^{-1} \propto \nu^{-1/2}$, so at 68 MHz V/I is a factor of 8.5 larger than at 4.9 GHz. We plot $\Delta_{V\text{V,fore}}^2$ for different configurations of the FFTT in Fig. 5.3. The synchrotron emission from point sources is expected to vary smoothly in frequency space, whereas the redshifted 21 cm signal varies rapidly in frequency space (similar to the galactic synchrotron signal). This is a similar situation to 21 cm temperature, and similar techniques should be applicable (Wang et al. 2006; Liu & Tegmark 2012).

We note that the sign of the circular polarization of a point source is determined by its internal magnetic field structure, so our result for $\Delta_{VV,fore}^2$ is not affected by source clustering so long as the sign of V is independent for each source. Furthermore, under these circumstances, there is no systematic contribution to TV , only a source of excess noise in VV .

Atmospheric Effects

Radio propagation through the Earth’s atmosphere is one of the key calibration challenges in low-frequency radio astronomy. At low frequencies ($\nu \leq 200$ MHz), propagation effects through the ionosphere become dominant. The physics of the propagation of the radio waves through a magnetized ionosphere is well understood. There are two primary effects at play after the polarization-dependent geometrical refraction by the ionosphere is removed. First, propagation through a turbulent ionosphere leads to stochastic interferometric visibilities, which contribute to an additional “scintillation noise” to the measurement of the power spectrum (e.g. Vedantham & Koopmans 2016). This scintillation noise can be larger than the thermal noise associated with low-frequency radio experiments.

Second, and most directly relevant here, is the inter-conversion of the polarization Stokes parameters (Q , U , V) and hence the generation of additional circular polarization signal due to Faraday rotation as discussed in Section 4.6. This mechanism for generating Stokes V is much more significant in the Earth’s ionosphere than in the ISM since the magnetic field B is much larger (generation of V depends on B^2 times column density, unlike regular Faraday rotation that depends on B times column density). Since again at low frequencies the ionosphere can result in $\gtrsim 1$ cycle of Faraday rotation, we use Eq. (4.51), with low-frequency linear polarization of order $\Delta_{QQ,gal} \sim 10$ K (see discussion in Section 4.6). The typical electron density in the F-layer of the ionosphere is $n_e \sim 10^5 \text{ cm}^{-3}$, the magnetic field is $B \sim 0.5$ G, and the typical path length is $L \sim 500$ km. At $1+z \sim 20$ this leads to an expected circular polarization signal of $\Delta_{VV,atm}^2 \approx 1$ K. We plot the expected order of magnitude of $\Delta_{VV,atm}^2$ due to atmospheric Faraday rotation against the noise power spectra in Fig. 5.3. As evident from the figure, this is likely to be the most challenging foreground for low-frequency circular polarization studies.

Calibration and correction of Faraday rotation distorted low-frequency measurements has been extensively studied in the literature, particularly in the context of ongoing 21 cm experiments. Similar techniques could potentially be applied to

remove the ionospheric circular polarization signal, but obviously they would have to be pushed many orders of magnitude beyond the present state of the art. Nevertheless, it is clear that the ionosphere represents perhaps the greatest foreground challenge to cosmological circular polarization studies.

4.7 Discussion

In Paper I of this series, we showed that the remote CMB quadrupole during the pre-reionization epoch leads to a small circular polarization of the emitted 21 cm radiation. In this paper we showed that measurement of the temperature-circular polarization cross-spectrum $P_{TV}(k)$ allows us to measure the remote quadrupole of the CMB. The remote quadrupole field at high redshifts can then be decomposed into E and B modes, and we showed that measurement of the B modes of this field can help us measure the tensor-to-scalar ratio r . We showed that, given the fiducial model for pre-reionization physics, a Fast Fourier Transform Telescope (FFTT) with side length 100 km can achieve $\sigma(r) \sim 4 \times 10^{-3}$ after ten years of observation while a FFTT of side length 1000 km can achieve $\sigma(r) \sim 10^{-5}$ after ten years of observation time.

One of the key results of this paper is that the sensitivity to measuring the remote CMB quadrupole is sensitive to the measurement of the modes with largest wavenumber (corresponding to the longest baselines in an interferometric experiment). For the fiducial model of pre-reionization physics considered in our paper, Fig. 4.7 implies that the method is most sensitive around $z \approx 19.5$, i.e. the time at which Lyman- α coupling becomes efficient in the fiducial model. Fig. 4.8 shows the sensitivity to measuring the tensor-to-scalar ratio r as a function of the side length of a FFTT, and for different observation times.

Our forecasts depend on assumptions made about the pre-reionization history of the universe, in particular on the rate of depolarization of the ground state of hydrogen through Lyman- α pumping, which is proportional to the mean Lyman- α flux. The parameters for the fiducial model that we consider for our sensitivity calculation are shown in Fig. 4.4. We note however that the Lyman- α flux at the redshifts of interest is completely unconstrained observationally; the “optimal” window in redshift, when $x_\alpha \sim O(1)$, would be earlier (later) if the Lyman- α flux is higher (lower). We note that lower Lyman- α flux would be advantageous for our method, since it places the transition at higher observed frequency where the foregrounds are less severe.

Another assumption in our technique is that the magnetic fields during the Dark Ages are below the "saturation limit" as described in Gluscevic et al. 2017. A saturated magnetic field has a strength such that the precession of hydrogen atoms in the hyperfine excited state is much faster than the decay (natural or stimulated) of the excited state. If the magnetic field is above the saturation limit, then the circular polarization signal will be suppressed. However most conventional models for magnetic fields during the Dark Ages predict unsaturated magnetic fields. A constraint on magnetic field strength during the Dark Ages as described in Refs. Venumadhav et al. 2014; Gluscevic et al. 2017 will thus be crucial before embarking on an experiment that uses the technique described in this paper.

To contrast our results to existing bounds on the tensor-to-scalar ratio, we note that the current upper bounds on r from the combination of the CMB B -mode and other observables are $r < 0.07$ (95% CL) (BICEP2 Collaboration et al. 2016). Next generation "Stage-4" CMB experiments have a goal of probing $r \leq 0.002$ (Abazajian et al. 2016), although several challenges remain in dealing with systematic effects.

Other authors have proposed techniques to detect inflationary gravitational waves that, while futuristic, have the potential to confirm a CMB detection, probe another range of scales, and/or improve sensitivity to r . Some of these techniques are based on conventional large-scale structure observables (Dodelson et al. 2003; Alizadeh & Hirata 2012; Schmidt & Jeong 2012; Schmidt et al. 2014; Chisari et al. 2014), although the surveys required even to detect $r \sim 0.07$ are very futuristic and many run up against cosmic variance limitations. Direct detection of the high-wavenumber gravitational waves with a network of space-based laser interferometers has been studied (Corbin & Cornish 2006; Kawamura et al. 2011).

The techniques most comparable to this work are other proposals using the enormous number of modes in redshifted 21 cm radiation. While the foreground-to-signal ratio is much higher for 21 cm experiments than for the CMB, the 21 cm measurement is a line measurement against a continuum foreground (as opposed to the continuum CMB signal) and so the ultimate factor by which foregrounds can be suppressed in analysis could be much larger. Masui & Pen 2010 proposed using the large number of Fourier modes available in a 21 cm survey to measure the intrinsic distortion of large scale structure due to inflationary gravitational waves. For a FFTT with $L = 100$ km their technique can detect $r \sim 10^{-3}$ which is similar to our forecasts. Book et al. 2012 proposed using the weak lensing of the 21 cm intensity fluctuations by gravitational waves to put bounds on r . This involves the measurement of the 21

cm power spectrum up to very small angular scales; to reach $r \sim 10^{-3}$, they would need to probe to $l_{\max} \sim 10^5$, requiring an array size of $L \gtrsim 100$ km.

The method proposed in this series is the first to make use of the 21 cm circular polarization signal (in cross-correlation with temperature: TV). It is also very futuristic, in the sense of requiring $L \sim 100$ km radio arrays (or $\sim 5 \times 10^8$ antennas). However, the foregrounds in circular polarization are much fainter than in brightness temperature, so our method for measuring r may turn out to be less problematic than methods based on the local anisotropy of the temperature power spectrum. In any case, the radio arrays that could implement the TT methods (Masui & Pen 2010; Book et al. 2012) are likely similar to what one would need for TV , so the techniques could be used to cross-check each other.

While the experimental setup required for the circular polarization method is very futuristic, it illustrates the rich array of physical processes and diagnostics that are in principle available in 21 cm surveys. Given the long-term interest in detecting inflationary gravitational waves, we hope that this idea will serve both to further motivate the goal of the ultimate 21 cm cosmology experiment, and inspire additional work on novel applications.

References

- Abazajian, K. N., Adshead, P., Ahmed, Z., et al., 2016, ArXiv e-prints
- Abbott, L. F., & Wise, M. B., 1984, Nuclear Physics B, 244, 541
- Abramowitz, M., & Stegun, I. A. 1972, Handbook of Mathematical Functions
- Alizadeh, E., & Hirata, C. M., 2012, PhRvD, 85.12, 123540, 123540
- Amarie, M., Hirata, C., & Seljak, U., 2005, PhRvD, 72.12, 123006, 123006
- Arnold, K., Stebor, N., Ade, P. A. R., et al., 2014, in Proc. SPIE, Millimeter, Submillimeter, and Far-Infrared Detectors and Instrumentation for Astronomy VII, Vol. 9153, 91531F
- Babich, D., & Loeb, A., 2005, ApJ, 635, 1
- Bardeen, J. M., Steinhardt, P. J., & Turner, M. S., 1983, PhRvD, 28, 679
- Baumann, D., 2009, ArXiv e-prints
- Bernardi, G., de Bruyn, A. G., Brentjens, M. A., et al., 2009, A&A, 500, 965
- Bernardi, G., Greenhill, L. J., Mitchell, D. A., et al., 2013, ApJ, 771, 105, 105
- BICEP2 and Keck Array Collaborations, Ade, P. A. R., Ahmed, Z., et al., 2015, ApJ, 811, 126, 126

- BICEP2 Collaboration, Ade, P. A. R., Aikin, R. W., et al., 2014, *ApJ*, 792, 62, 62
- BICEP2 Collaboration, Keck Array Collaboration, Ade, P. A. R., et al., 2016, *Physical Review Letters*, 116.3, 031302, 031302
- Book, L., Kamionkowski, M., & Schmidt, F., 2012, *Physical Review Letters*, 108.21, 211301, 211301
- Bunn, E. F., 2006, *PhRvD*, 73.12, 123517, 123517
- Chisari, N. E., Dvorkin, C., & Schmidt, F., 2014, *PhRvD*, 90.4, 043527, 043527
- Cohen, A. 2004, Estimates of the Classical Confusion Limit for the LWA, <http://www.faculty.ece.vt.edu/swe/lwa/memo/lwa0017.pdf>
- Cooray, A., & Baumann, D., 2003, *PhRvD*, 67.6, 063505, 063505
- Corbin, V., & Cornish, N. J., 2006, *Classical and Quantum Gravity*, 23, 2435
- de Búrca, D., & Shearer, A., 2015, *MNRAS*, 450, 533
- De, S., & Tashiro, H., 2014, *PhRvD*, 89.12, 123002, 123002
- Di Matteo, T., Perna, R., Abel, T., & Rees, M. J., 2002, *ApJ*, 564, 576
- Di Matteo, T., Ciardi, B., & Miniati, F., 2004, *MNRAS*, 355, 1053
- Dodelson, S., Rozo, E., & Stebbins, A., 2003, *Physical Review Letters*, 91.2, 021301, 021301
- Doré, O., Holder, G. P., & Loeb, A., 2004, *ApJ*, 612, 81
- Enßlin, T. A., Hutschenreuter, S., Vacca, V., & Oppermann, N., 2017, *ArXiv e-prints*
- Essinger-Hileman, T., Appel, J. W., Beall, J. A., et al., 2010, *ArXiv e-prints*
- Fabbri, R., & Pollock, M. D., 1983, *Physics Letters B*, 125, 445
- Furlanetto, S. R., Oh, S. P., & Briggs, F. H., 2006, *PhR*, 433, 181
- Ghosh, A., Prasad, J., Bharadwaj, S., Ali, S. S., & Chengalur, J. N., 2012, *MNRAS*, 426, 3295
- Gluscevic, V., Venumadhav, T., Fang, X., et al., 2017, *PhRvD*, 95.8, 083011, 083011
- Guth, A. H., 1981, *PhRvD*, 23, 347
- Guth, A. H., & Pi, S.-Y., 1982, *Physical Review Letters*, 49, 1110
- Haardt, F., & Madau, P., 2012, *ApJ*, 746, 125, 125
- Haslam, C. G. T., Salter, C. J., Stoffel, H., & Wilson, W. E., 1982, *A&AS*, 47, 1
- Hawking, S. W., 1982, *Physics Letters B*, 115, 295
- Homan, D. C., & Wardle, J. F. C., 1999, *AJ*, 118, 1942
- Hu, W., & White, M., 1997, *PhRvD*, 56, 596

- Jelić, V., de Bruyn, A. G., Mevius, M., et al., 2014, *A&A*, 568, A101, A101
- Jelić, V., de Bruyn, A. G., Pandey, V. N., et al., 2015, *A&A*, 583, A137, A137
- Kamionkowski, M., Kosowsky, A., & Stebbins, A., 1997a, *PhRvD*, 55, 7368
- , 1997b, *Physical Review Letters*, 78, 2058
- Kamionkowski, M., & Loeb, A., 1997, *PhRvD*, 56, 4511
- Kawamura, S., Ando, M., Seto, N., et al., 2011, *Classical and Quantum Gravity*, 28.9, 094011, 094011
- King, S., & Lubin, P., 2016, *PhRvD*, 94.2, 023501, 023501
- Knox, L., 1997, *ApJ*, 480, 72
- Legg, M. P. C., & Westfold, K. C., 1968, *ApJ*, 154, 499
- Lewis, A., Challinor, A., & Lasenby, A., 2000, *ApJ*, 538, 473
- Linde, A. D., 1982, *Physics Letters B*, 108, 389
- Liu, A., Tegmark, M., & Zaldarriaga, M., 2009, *MNRAS*, 394, 1575
- Liu, A., & Tegmark, M., 2012, *MNRAS*, 419, 3491
- Macquart, J.-P., & Melrose, D. B., 2000, *ApJ*, 545, 798
- Martin, J., 2016, *Astrophysics and Space Science Proceedings*, 45, 41
- Masui, K. W., & Pen, U.-L., 2010, *Physical Review Letters*, 105.16, 161302, 161302
- Mesinger, A., Furlanetto, S., & Cen, R., 2011, *MNRAS*, 411, 955
- Moore, D., Aguirre, J. E., Kohn, S., et al., 2015, *ArXiv e-prints*
- Mukhanov, V. F., & Chibisov, G. V., 1981, *ZhETF Pisma Redaktsiiu*, 33, 549
- Naess, S., Hasselfield, M., McMahon, J., et al., 2014, *JCAP*, 10, 007, 007
- Oh, S. P., & Mack, K. J., 2003, *MNRAS*, 346, 871
- Oppermann, N., Junklewitz, H., Robbers, G., et al., 2012, *A&A*, 542, A93, A93
- Pen, U.-L., Chang, T.-C., Hirata, C. M., et al., 2009, *MNRAS*, 399, 181
- Planck Collaboration, Ade, P. A. R., Aghanim, N., et al., 2016a, *A&A*, 594, A20, A20
- , 2016b, *A&A*, 594, A17, A17
- Planck Collaboration, Ade, P. A. R., Aghanim, N., et al., 2016c, *A&A*, 594, A13, A13
- Portsmouth, J., 2004, *PhRvD*, 70.6, 063504, 063504
- Rayner, D. P., Norris, R. P., & Sault, R. J., 2000, *MNRAS*, 319, 484

- Roberts, J. A., Cooke, D. J., Murray, J. D., et al., 1975, *Australian Journal of Physics*, 28, 325
- Rubakov, V. A., Sazhin, M. V., & Veryaskin, A. V., 1982, *Physics Letters B*, 115, 189
- Sault, R. J., & Macquart, J.-P., 1999, *ApJL*, 526, L85
- Schmidt, F., & Jeong, D., 2012, *PhRvD*, 86.8, 083513, 083513
- Schmidt, F., Pajer, E., & Zaldarriaga, M., 2014, *PhRvD*, 89.8, 083507, 083507
- Seljak, U., 1997, *ApJ*, 482, 6
- Seljak, U., & Zaldarriaga, M., 1996, *ApJ*, 469, 437
- , 1997, *Physical Review Letters*, 78, 2054
- Skordis, C., & Silk, J., 2004, *ArXiv Astrophysics e-prints*
- Starobinskiĭ, A. A., 1979, *Soviet Journal of Experimental and Theoretical Physics Letters*, 30, 682
- Tegmark, M., & Zaldarriaga, M., 2009, *PhRvD*, 79.8, 083530, 083530
- Vedantham, H. K., & Koopmans, L. V. E., 2016, *MNRAS*, 458, 3099
- Venumadhav, T., Oklopcic, A., Gluscevic, V., Mishra, A., & Hirata, C. M., 2014, *ArXiv e-prints*
- Wang, X., Tegmark, M., Santos, M. G., & Knox, L., 2006, *ApJ*, 650, 529
- Wardle, J. F. C., Homan, D. C., Ojha, R., & Roberts, D. H., 1998, *Nature*, 395, 457
- Zaldarriaga, M., & Seljak, U., 1997, *PhRvD*, 55, 1830
- Zaldarriaga, M., Furlanetto, S. R., & Hernquist, L., 2004, *ApJ*, 608, 622

*Chapter 5***CHARACTERIZING FOREGROUNDS FOR REDSHIFTED 21cm
RADIATION USING THE LONG WAVELENGTH ARRAY:
CROSS-CORRELATION WITH TRACERS OF ISM****ABSTRACT**

Broadband foreground sources pose the greatest challenge to 21cm tomography and need to be characterized carefully before the technique becomes a sensitive probe of the dark ages and the epoch of reionization. The foregrounds are expected to be predominantly galactic and approximately four orders of magnitude larger than the cosmological signal. In this paper, we investigate the nature of the diffuse Galactic radio emission in the 20 – 80MHz frequency range using data from the Owens Valley Radio Observatory Long Wavelength Array (OVRO LWA). We cross-correlate LWA maps with tracers of ISM from a number of surveys, to investigate galactic foregrounds relevant to detection of 21cm signal from the Dark Ages. We compute the cross-power spectra between LWA maps at different frequencies with dust, $H\alpha$, and HI tracers. Our results are consistent with no correlation between tracers of the gas and dust in the ISM at high Galactic latitudes ($b > 55^\circ$) and low-frequency maps from the LWA, at scales $\ell \sim 10 - 600$ at a 99.9% confidence level.

5.1 Introduction

The detection of the redshifted 21cm radiation from neutral hydrogen at high redshifts is expected to revolutionize our understanding of cosmology and astrophysics in the coming decades. Detection of the signal will provide valuable information about the post-recombination history of the universe, including the Dark Ages as well as information about formation of the first ionizing sources and the subsequent re-ionization of the Intergalactic Medium (IGM) due to these sources (Hogan & Rees 1979; Madau et al. 1997; Tozzi et al. 2000; Iliev et al. 2002; Furlanetto et al. 2004a; Furlanetto et al. 2004b; Loeb & Zaldarriaga 2004; Barkana & Loeb 2005; for a comprehensive review see Furlanetto et al. 2006). 21cm tomography is expected to produce 3D maps of the matter distribution dramatically larger than current large scale probes, enabling precision tests of inflation and potentially placing extremely strong constraints on cosmological parameters such as the dark energy equation of state), spatial curvature and neutrino mass (McQuinn et al. 2006; Mao et al. 2008 and references therein).

In practice, 21 cm tomography involves imaging the radio sky with low-frequency radio interferometers at different frequencies (corresponding to different redshift slices) and collating them to a 3D map. These images however are expected to be dominated by galactic foregrounds, particularly synchrotron emission from the Milky Way. These foregrounds are in fact expected to be around four orders of magnitude brighter than the cosmological signal, making the detection of the latter extremely challenging (de Oliveira-Costa et al. 2008; Bernardi et al. 2011).

One of the key observational challenges in detecting the cosmological 21cm signal is modeling and characterizing the Galactic radio emission at low frequencies. This has generated a lot of interest in modeling and removing Galactic foregrounds at low frequencies. Two broad strategies have emerged: early ideas involved using the spatial structure of foregrounds to separate them from the cosmological signal (Di Matteo et al. 2002; Oh & Mack 2003; Santos et al. 2005; Zaldarriaga et al. 2004). More recent proposals make use of the spectral structure in the intrinsic cosmological signal, which varies rapidly in frequency space since a small difference in frequency corresponds to mega-parsecs of cosmological distance, over the foreground signal that is spectrally smooth (Liu & Tegmark 2012 and references therein).

Beyond understanding low-frequency foregrounds, understanding diffuse radio emission from the Galaxy is interesting in its own right. de Oliveira-Costa et al. 2008 modeled the diffuse galactic radio emission across the 10MHz-100GHz range. Their

Global Sky Model (GSM), implemented a Principal Component Analysis (PCA) on the 11 highest quality radio maps across the 10MHz-100GHz frequency range. The GSM is extensively used in the astrophysics community, including putting limits on the power spectrum from the Epoch of Reionization (EoR) (see Ali et al. 2015).

One of the key limitations of the GSM is the lack of all sky maps in the low-frequency range, relevant to 21cm tomography experiments. For the high resolution GSM, crucial for 21cm studies, the model hinges on the 408 MHz Haslam maps (Haslam et al. 1981, Haslam et al. 1982). . More recently Zheng et al. 2017 have extended the original GSM by using 29 maps in the 10 MHz to 5 THz range, including the Parkes maps at 85 MHz and 150 MHz (Landecker & Wielebinski 1970). The GSM in the 10 MHz-100 MHz range, still remains largely an extrapolation, and direct observational characterization of galactic emission at these frequencies, with large sky and frequency coverage, and high resolution, has been missing.

In this paper we investigate the spatial structure of radio emission from the galaxy using data from the Owens Valley Radio Observatory Long Wavelength Array (OVRO-LWA) in the 20 – 80MHz frequency range. We cross-correlate low-frequency LWA maps with known tracers of the Milky Way Interstellar Medium (ISM). Our motivation is twofold: we wish to detect if known ISM tracers emit at the radio frequencies relevant to 21cm tomography studies. Secondly, since there have been no all-sky observations at these frequencies, we wish to detect any anomalous radiative processes at these low-frequencies.

For our analysis, we cross-correlate the LWA maps with full-sky maps of known tracers of the ISM: dust, $H\alpha$ and HI. We compute auto and cross-spectra for different cuts in the sky off the plane of the galaxy that are relevant to current and future 21cm experiments. The techniques used are similar to the methods to detect weak-lensing (Hirata et al. 2004; Hirata et al. 2008) or the ISW effect (Ho et al. 2008) using cross-correlation of Large Scale Structure (LSS) and CMB maps.

This chapter is organized as follows: we provide some historical context for the search for unknown radio foregrounds in Section 5.2. Section 5.3 describes the OVRO LWA experiment and in Section 5.4 we provide an overview of the data processing required to generate low-frequency maps. The ISM datasets used in our cross-correlation analysis are described in Section 5.5; the methodology and results of cross-correlation different maps are in Section 5.6 and 5.7.

5.2 Motivation: Characterizing Low-Frequency Radio Foregrounds

While the radio foregrounds at 10-100 MHz range are relatively unexplored, the explosion of CMB experiments over the past two decades have led to an exhaustive treatment of radio foregrounds at higher frequencies. While the radiative processes expected to dominate the radio skies in the 10 – 100MHz regime are expected to be different from the CMB sky, the CMB studies provide an important historical context for this work.

The continuum emission mechanisms from the diffuse ISM in the 10-100 GHz range were expected to be dominated by two radiative processes:

1. Free-free emission (thermal bremsstrahlung)
2. Synchrotron emission due to relativistic electrons in the galaxy

However, radio emission below 40GHz, with hints of anomalous spectral properties, was first reported in the analysis of COBE DMR data by Kogut et al. 1996 who initially identified it as free-free emission but this was ruled out on energetic grounds (Draine & Lazarian 1998). The observations were confirmed by ground-based measurements at smaller angular scales (de Oliveira-Costa et al. 1997; Leitch et al. 1997), and it was established that the emission was dust-correlated (de Oliveira-Costa et al. 1999; de Oliveira-Costa et al. 2002) The thermal dust emission (due to vibrational modes) at these frequencies is expected to be negligible. It was eventually proposed that the dust-correlated Anomalous Microwave Emission (AME) is electric dipole radiation from tiny, rapidly spinning dust grains (Draine & Lazarian 1998). The spinning dust model provides an excellent fit to the data (Planck Collaboration XX 2011). However, there remains high-latitude diffuse emission that has not been definitely associated with a known radiative processes. Potential explanations for this unexplained emission include magneto-dipole radiation from thermal fluctuations of magnetized grains (Draine & Lazarian 1999; Liu et al. 2014).

At 10 – 100MHz frequencies, the sky is expected to be dominated by three radiative processes:

1. Synchrotron emission from relativistic emission in the galaxy
2. Free-free emission (thermal bremsstrahlung),
3. Hydrogen recombination

The thermal dust emission (from vibrational modes) and the spinning dust emission at these frequencies are not expected to be observationally significant.

The LWA maps are the first high-resolution radio maps (reaching up to $l \sim 1000$), with a large frequency and sky coverage in the 20 – 800MHz frequency regime. Given the importance of this frequency window for 21cm tomography studies, it is important to investigate unexpected foreground sources in these maps. Our goal in this paper is to search for spatial/morphological correlations between known tracers of the ISM and radio maps from the LWA. Our work is similar in spirit to the hunt for "foreground X" during the post-WMAP era (Finkbeiner 2004; Finkbeiner et al. 2002; de Oliveira-Costa et al. 2004).

Beyond search for any anomalous low-frequency emission, it is also important to characterize known foregrounds to extract meaningful cosmological information from 21cm experiments. Recent analysis of the BICEP2/Keck Array data showed that extrapolating foreground templates, especially those derived from small regions in the sky, to low-frequencies can be misleading. For instance, extrapolating the all-sky observations of Planck at 353 GHz to 150 GHz (the BICEP2 frequency) led to an estimate of the B -mode angular power spectrum that was consistent with dust (Planck Collaboration et al. 2016), refuting an earlier claim that the B -mode was due to inflationary gravitational waves. Thus instead of relying on the GSM to make extrapolated templates of the foregrounds at low-frequencies, it is crucial to compare the low-frequency maps to known ISM tracers as a "sanity check".

There has also been a growing interest in using cross-correlations of future 21cm maps with CMB maps to extract cosmological information (see for example Tashiro et al. 2010). The foreground contamination in such cross-correlation studies depends on any cross-correlation between low-frequency maps and ISM structure traced by dust or $H\alpha$ maps. It is thus timely to investigate whether any such correlation exists.

5.3 The Long Wavelength Array

The Owens Valley Long Wavelength Array (OVRO LWA) is a full cross-correlation interferometer designed for all-sky imaging from Owens Valley. The LWA is an array of 288 dual polarization antennas, with each antenna consists of two perpendicular dipoles (see figure). It has an instantaneous bandwidth covering 24 MHz to 82 MHz. It has the largest number of correlated baselines operational: 33,000 baselines with 60 MHz bandwidth. The OVRO-LWA hosts the 512-input correlator, a "large-N"

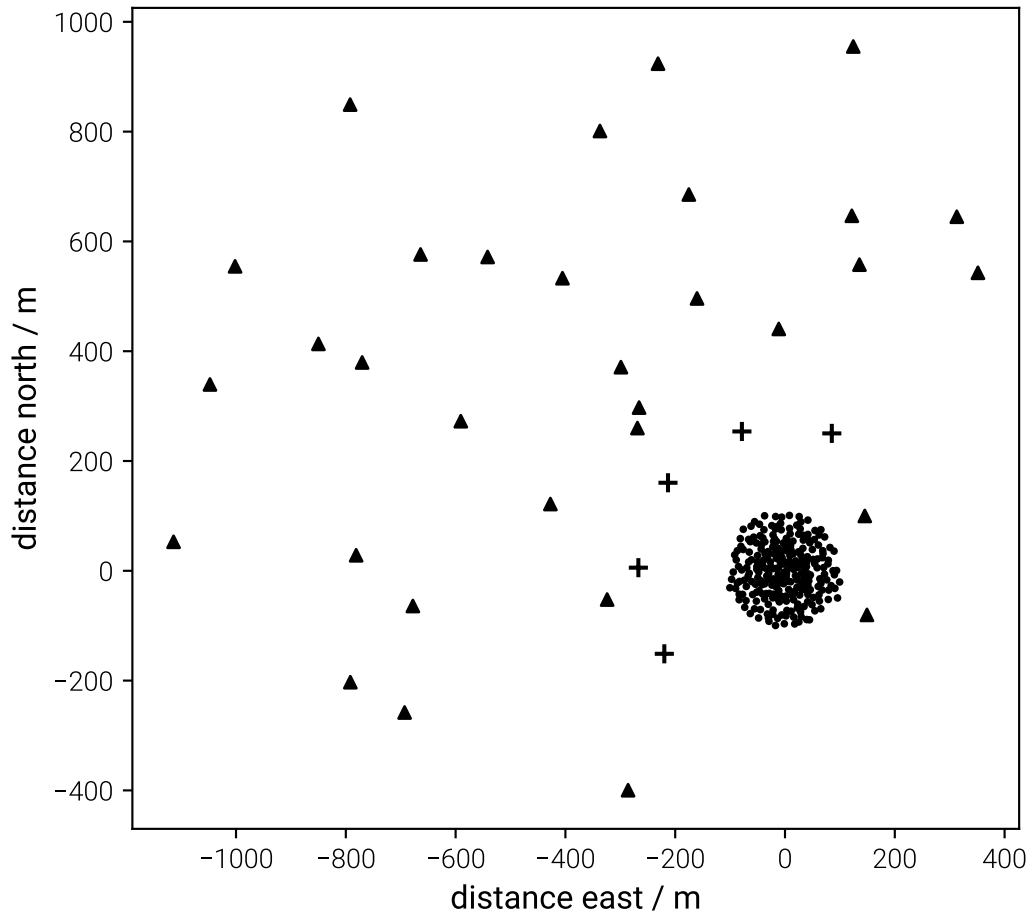


Figure 5.1: Map of the antenna layout for OVRO LWA. Black circles correspond to the 251 core antennas. The black triangles correspond to the 32 expansion antennas that extend the maximum baseline of the array. The 5 crosses are antennas equipped with noise-switched front ends for calibrated total power measurements. This figure was provided courtesy of Michael Eastwood and to be published in Eastwood et. al. (in prep)

correlator developed by the Large-Aperture Experiment to Detect the Dark Ages (LEDA, Kocz et al. 2015). The instrument is described in detail in Hallinan et al. (in prep) and the data processing for making all-sky maps are described in Eastwood et. al. (in prep).

The relative faintness of the 21cm signal and the presence of strong foregrounds implies that, to make a detection, an ideal 21cm experiment needs to measure a large number of cosmological modes, with long integration times, and careful calibration. The large field-of-view of the OVRO-LWA, and its frequency range thus makes it an ideal experiment for 21cm cosmology, focused on the dark ages.

Of the the 288 antennas, 251 are arranged within a 200 meter diameter "core" that enables very high thermal sensitivity. An additional 32 "expansion" antennas are placed up to 2 kilometers away from the central core of the interferometer. These antennas are used to image the entire sky with 10 arcminute resolution in a single snapshot. Finally, there are 5 antennas equipped with noise-switched receivers that allow for calibrated total power measurements of the sky. For the maps analyzed in this paper we just use the core and the expansion antennas.

Both the core and the expansion antennas use the same broadband dipole. The first stage of amplification occurs at the antenna (in a white box at the top of the post holding the dipole antennas- see figure). The first-stage amplifier is uncooled since the additional noise due to an uncooled first-stage amplifier is negligible compared to the sky brightness. For the core antennas, the signal is then transported via a coaxial cable to an electronics shelter, while for the expansion antennas the analog signal is sent to the electronics shelter via a fiber optic cable.

In the electronics shelter, the signal enters into a shielded analog signal processing rack where the signal is further amplified and passes through a configurable bandpass filter that filters out FM radio (at the top of the band) and RFI at the bottom of the band. After this the signal is digitized with a sampling rate of 196.602 MHz. There is a coarse-delay correction but no fine-delay correction on the signal. The signal is then correlated by the 512-input LEDA correlator Kocz et al. 2015. There are 13 second integrations in the correlator (chosen so that the integrations evenly divide a sidereal day). There are 2398 frequency channels (24 kHz wide). The channel width is determined by bandwidth smearing constraints (wider channels wash out the signal) and computational limits (narrower channels are more computationally expensive). The correlator delivers full polarization information, however at this stage the data processing does not use this information to make full polarization maps.

5.4 Observations and Data Processing

In this section, we briefly describe the data processing and imaging algorithm used to obtain the maps that we use for our cross-correlation analysis. Details of the algorithm and data processing can be found in Eastwood et. al. (in prep).

The low-frequency radio maps used in this chapter were produced using data from the OVRO-LWA that was collected over 28 consecutive hours starting at on 2017-02-17 12:00:00 UTC time. This observation run was chosen since it coincided

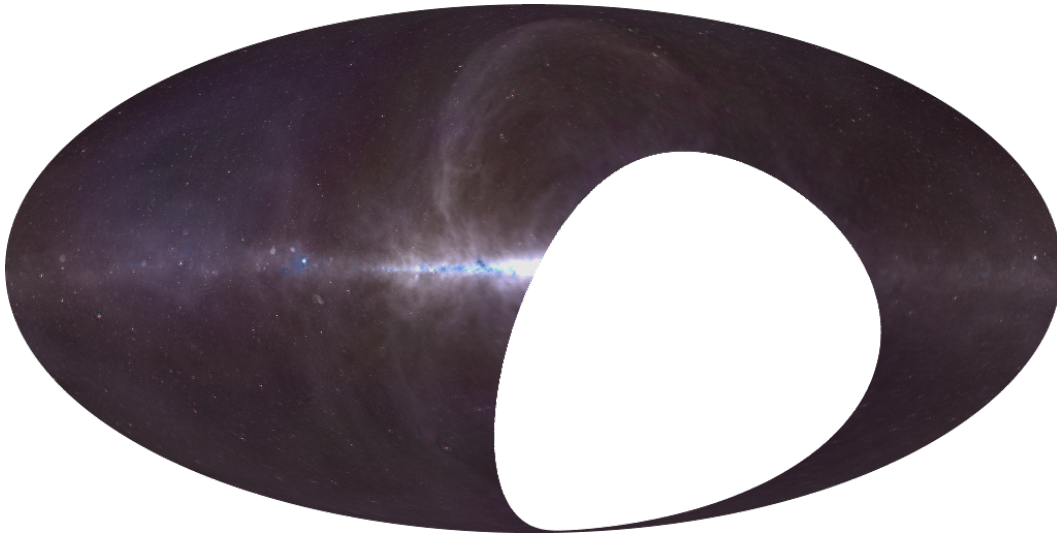


Figure 5.2: 3-color all-sky map generated with m-mode analysis imaging techniques. This figure was provided courtesy of Michael Eastwood and to be published in Eastwood et. al. (in prep)

with rains in OVRO, which improve the RFI environment on the site. During the observations, the LWA operated as a zenith-pointing drift scanning interferometer (Eastwood et. al. (in prep)).

The antenna gains are measured and calibrated against Cyg A and Cas A: the brightest radio point sources in the northern hemisphere. This is done using a data track when both Cyg A and Cas A are at high elevations. Since, the OVRO LWA is a drift scanning interferometer, the primary beam is measured by making a set of symmetry assumptions (eg: assuming that the primary beam is invariant under north-south and east-west flips) and then measuring the flux of several bright sources (Cyg A, Cas A etc.) as they pass through the field of view and fitting a beam model composed of Zernike polynomials to the measurements. There is radio frequency interference (RFI) from badly insulated power line poles that arc and produce pulsed, broadband RFI. These sources can be identified and removed by noting that averaged over a 24 hour period, true sky components are smeared along tracks of constant declination, while the power lines are not. The removal of RFI is made challenging by the fact that the sources are at low elevation, and the antenna response is practically unknown; Eastwood et. al. (in prep) describe a method called “peeling” that peels RFI sources from the averaged visibilities, obtained after smearing the visibilities over > 24 hours.

Imaging the sky involves estimation of the sky brightness $I_\nu(\hat{r})$ in the direction \hat{r}

and frequency ν . However, as discussed in Chapter 3, an interferometer measures *visibilities*, $V_{ij,\nu}$ between pairs of antennas. For antennas separated by a baseline \vec{b}_{ij} , and with a beam function $A_\nu(\hat{r})$ we have,

$$V_\nu^{ij} = \int_{\text{sky}} A_\nu(\hat{r}) I_\nu(\hat{r}) \exp\left(2\pi i \hat{r} \cdot \vec{b}_{ij} / \lambda\right) d\Omega. \quad (5.1)$$

Imaging thus involves estimating $I_\nu(\hat{r})$ given the available measurements V_ν^{ij} from an interferometer.

Solving the matrix equation that results from discretization of the above equation is however computationally very expensive. For an interferometer with N_{base} baselines, measuring N_{freq} frequency channels over N_{time} discrete integrations, and a sky that is discretized into N_{pix} pixels, the total dataset can be represented through a matrix of complex numbers with dimensions of $(N_{\text{base}} N_{\text{freq}} N_{\text{time}}) \times (N_{\text{pix}})$. For a single-channel LWA measurement this is a 5 petabyte array, and the simple solution of the matrix equation needs prohibitive computation power.

***m*-Mode Analysis**

Eastwood et. al. (in prep), have implemented a novel method that exploits the drift-scan strategy of the OVRO-LWA. This method, called *m*-mode analysis, uses a *temporal symmetry* in equation 5.1 that greatly reduces the amount of computing time, by allowing us to write down a block-diagonal matrix relationship between an observed quantity (the *m*-modes) and the spherical harmonic coefficients of the sky (Shaw et al. 2014; Shaw et al. 2015). We briefly outline the method below.

For a drift-scan telescope like the OVRO-LWA, the visibilities are a periodic function of the sidereal time. The Fourier transform of the visibilities with respect to the sidereal time $\phi \in [0, 2\pi)$ is,

$$V_{m,\nu}^{ij} = \int_0^{2\pi} V_\nu^{ij}(\phi) \exp\left(-im\phi\right) d\phi \quad (5.2)$$

This Fourier transform gives us a set of *m*-modes $V_{m,\nu}^{ij}$ where $m = 0, \pm 1, \pm 2, \dots$ is the Fourier conjugate of ϕ , with higher values of *m* corresponding to variability of the visibility on shorter timescales.

It can be shown that the *m*-modes $V_{m,\nu}^{ij}$ can be written as a linear combination of interferometer response on the sky $B_{lm,\nu}^{ij}$ (which encodes information about the baselines and the antenna beams) and the spherical harmonic coefficients of the sky

brightness $a_{lm,v}$.

$$V_{m,v}^{ij} = \sum_l B_{lm,v}^{ij} a_{lm,v}, \quad (5.3)$$

This equation is a matrix equation with a block-diagonal matrix \mathbf{B} ,

$$\mathbf{B} = \begin{pmatrix} m = 0 & & & \\ & m = \pm 1 & & \\ & & m = \pm 2 & \\ & & & \ddots \end{pmatrix}. \quad (5.4)$$

Consider a vector \mathbf{v} whose components are the list of m -modes and the vector \mathbf{a} containing the list of spherical harmonic coefficients. In order to take advantage of the block-diagonal structure in \mathbf{B} , we sort the values of \mathbf{v} and \mathbf{a} by the value of m , grouping positive and negative values of m together. The matrix equation can then be written as,

$$\overbrace{\begin{pmatrix} \vdots \\ m\text{-modes} \\ \vdots \end{pmatrix}}^{\mathbf{v}} = \overbrace{\begin{pmatrix} \ddots & & \\ & \text{transfer matrix} & \\ & & \ddots \end{pmatrix}}^{\mathbf{B}} \overbrace{\begin{pmatrix} \vdots \\ a_{lm} \\ \vdots \end{pmatrix}}^{\mathbf{a}}. \quad (5.5)$$

To proceed we choose the spherical harmonics on the sky for all $\ell < \ell_{\max}$, where ℓ_{\max} corresponds to the longest baselines in the array. For the maps generated for this chapter we use $\ell_{\max} = 1000$. This construction reduces the size of the transfer matrix to 500 MB. This also reduces computational complexity by breaking up the matrix inversion problem into independent blocks. For the case of the LWA the m -mode analysis breaks up the matrix equation into $\sim 10^3$ independent blocks, saving a factor $\sim 10^9$ in processing time.

The inversion problem is however only one of the challenges confronting imaging using drift-scan interferometers like the LWA. The removal of bright point sources, terrestrial RFI at low-frequencies, and characterizing ionospheric effects that break the assumptions of Equation 5.2 make map-making particularly challenging. Eastwood et. al (in prep) describe the map making process in detail and the methods are beyond the scope of this thesis.

In the remainder of this chapter we use low-frequency maps from the LWA that have been generated using methods described above and cleaned for RFI and point sources as our primary data input.

5.5 External Data Sets

We describe the dust, H α , HI and LWA radio maps used in our analysis below; the data sets are summarized in Table I. All maps were converted to ITRF coordinates, pixelized using HEALPix RING scheme (Górski et al. 2005) with a resolution $n_{\text{side}} = 512$ for the LWA and dust maps, $n_{\text{side}} = 1024$ for HI maps and $n_{\text{side}} = 256$ for the H α maps (corresponding to $12 \times n_{\text{side}}^2$ equal area pixels across the sky).

IRAS + DIRBE/COBE Maps

We use the extrapolated full-sky maps by Finkbeiner et al. 1999 (FDS99) of sub-millimeter and microwave emission from diffuse interstellar dust in the Galaxy. These maps are constructed by extrapolating from the $100\mu\text{m}$ emission and the $100/240\mu\text{m}$ flux ratio maps generated by Schlegel et al. 1998 (SFD98) from the Infrared Astronomy Satellite (IRAS) and Diffuse Infrared Background Experiment on COBE (DIRBE/COBE). These maps were made by combining high resolution (but relatively poorly calibrated) data from IRAS and the lower angular resolution (0.7°) maps from DIRBE which exquisitely calibrated. This map is a good predictor of the microwave emission from Galactic dust.

The extrapolation of $100\text{-}240\mu\text{m}$ SFD98 maps to microwave frequencies is complicated by the details of the composition and emissivity properties of interstellar dust. FDS99 use a two-component dust model to extrapolate the dust emissivity across the sky at GHz frequencies. The maps have the zodiacal light and point sources removed.

For the cross-correlation power spectrum analysis cut out the galactic plane by removing pixels with $-30^\circ \leq l \leq 30^\circ$. We also make a cut for the southern hemisphere "blindspot" for LWA (see Fig. 1). We then cut the sky into five regions described in Section III. A.

H α Maps

We use the full-sky template map of the Galactic free-free emission component at 30 GHz created by Dickinson et al. 2003. Their template is based on H α data from the Wisconsin H-Alpha Mapper (WHAM) survey Haffner et al. 2003 at 1° resolution for the Northern Hemisphere, and the Southern H-Alpha Sky Survey Atlas (SHASSA) for the Southern hemisphere.

Dickinson et al. 2003 correct the H α maps for dust absorption using the $100 - \mu\text{m}$ dust maps of Schlegel et al. 1998 and convert the dust-corrected H α data into

a radio surface brightness. The template provides an accurate map of the radio emission in the frequency range of 100 MHz–100 GHz, and electron temperature range 3000–20,000 K. We note that another $H\alpha$ template map by Finkbeiner 2003 is frequently used in the CMB community. However, the resolution of their map is not same across the sky and is thus not suitable for the kind of cross-correlation analysis that is our goal in this chapter.

HI Maps

For galactic HI emission, we use data from the full-sky HI4PI Survey (HI4PI Collaboration et al. 2016) which combines data from the Effelsberg-Bonn HI Survey (Winkel et al. 2016) and the Galactic All-Sky Survey (McClure-Griffiths et al. 2009). The map traces HI emission over the full sky with radial velocities $|v_{LSR}| < 600 \text{ km s}^{-1}$ (470 km s^{-1} for the southern hemisphere, with a spectral resolution of 1.45 km s^{-1}). The survey has an angular resolution $16.1'$ and a sensitivity of 43 mK. The survey corrects for stray radiation that is reliable even in low-column density regions of the sky. For the cross-correlation analysis we use the HI4PI maps with a HEALPix resolution of $n_{\text{side}} = 1024$.

5.6 Cross-Correlation Power Spectrum Analysis

Sky Cuts

We are interested in investigating cross-correlations between LWA maps and ISM tracers in parts of the sky that are most interesting to 21cm cosmology. This involves cutting out the galactic plane and looking at parts of the sky at relatively high galactic latitudes in the northern hemisphere (or low galactic latitude in the southern hemisphere). For the analysis reported in this chapter we consider a patch in the northern hemisphere at high galactic latitudes $b > 55^\circ$. Note that the LWA blindspot restricts us to use only very low galactic latitudes in the southern hemisphere.

Methodology

The methodology we adopt is similar to CMB×LSS cross-correlation measurements to measure the ISW effect (Padmanabhan et al. 2005 and Ho et al. 2008) as well as weak gravitational lensing (Hirata et al. 2004 Ho et al. 2008). We outline the method here for completeness. To compute the cross-spectra, we begin by arranging temperature fluctuations in different maps into a single data vector,

$$\mathbf{x} = (x_\nu, x_I), \quad (5.6)$$

where \mathbf{x}_ν is a vector with radio temperature fluctuations (with the monopole subtracted), in a frequency band centered at ν , at every HEALPix pixel; similarly, \mathbf{x}_I is the effective temperature fluctuation of the ISM tracer under consideration (i.e. I = dust or H α or H I). The total length of \mathbf{x} is $N_{\text{pix},\nu} + N_{\text{pix},I}$ where $N_{\text{pix},\nu}$ is the number of pixels in the LWA map and $N_{\text{pix},I}$ is the number of pixels in the ISM tracer map.

The covariance matrix of \mathbf{x} is,

$$\mathbf{C} = \mathbf{C}_{\text{diag}} + \begin{pmatrix} 0 & \mathbf{C}^{\nu I\dagger} \\ \mathbf{C}^{\nu I} & 0 \end{pmatrix}, \quad (5.7)$$

where \mathbf{C}_{diag} is,

$$\mathbf{C}_{\text{diag}} = \begin{pmatrix} \mathbf{C}^{\nu\nu} + \mathbf{N}^{\nu\nu} & 0 \\ 0 & \mathbf{C}^{II} + \mathbf{N}^{II} \end{pmatrix}, \quad (5.8)$$

where \mathbf{N}^{XX} is the noise matrix. The submatrices \mathbf{C}^{XY} are defined by,

$$C_{ij}^{XY} = \sum_{lm} C_l^{XY} Y_{lm}^*(\hat{n}_i^X) Y_{lm}(\hat{n}_j^Y), \quad (5.9)$$

where \hat{n}_i^X is the direction of the i^{th} pixel of the vector \mathbf{x}_X .

In order to construct an optimal estimator for the radio-ISM cross-spectrum, we need the auto-correlation matrix for the LWA radio and the ISM maps. We estimate the power spectra first using the HEALPy package. HEALPy uses the HEALPix package developed by Górski et al. 2005. We use the anafast routine to calculate the initial auto-correlation matrix. Anafast performs a harmonic analysis of the HEALPix maps up to maximum spherical harmonic order ℓ_{max} by computing integrals on the whole sphere. The package is not optimally suited to make accurate power-spectra estimates for cut maps and accounting for pixel-level noise. Instead it provides a rough initial estimate for the auto-spectra that can be fed into our routine.

We then parametrize $C_l^{\nu I}$ as a sum of bandpowers $\tilde{P}_{i,l}$, with amplitudes c_i that need to be estimated,

$$C_l^{\nu I} = \sum_i c_i \tilde{P}_{i,l}. \quad (5.10)$$

We estimate c_i by constructing quadratic combinations of the data (Tegmark 1997; Seljak 1998),

$$Q_i = \frac{1}{2} \mathbf{x}^T \mathbf{C}_{\text{diag}}^{-1} \frac{\partial \mathbf{C}}{\partial c_i} \mathbf{C}_{\text{diag}}^{-1} \mathbf{x}. \quad (5.11)$$

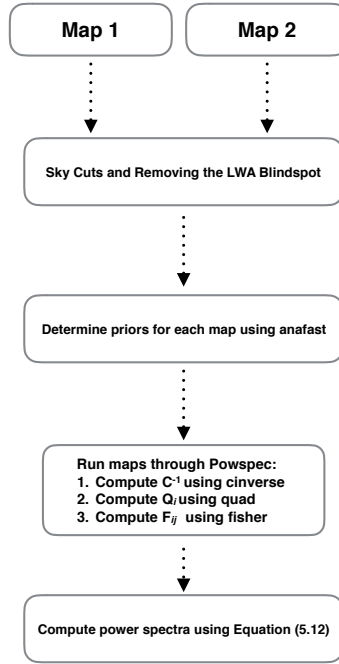


Figure 5.3: Outline for powspec

Q_i is related to the estimate \hat{c}_i by the response matrix \mathbf{F} ,

$$\hat{c}_i = \sum_j (\mathbf{F}^{-1})_{ij} Q_j, \quad (5.12)$$

where,

$$\mathbf{F}_{ij} = \frac{1}{2} \text{tr} \left[\mathbf{C}_{\text{diag}}^{-1} \frac{\partial \mathbf{C}}{\partial c_i} \mathbf{C}_{\text{diag}}^{-1} \frac{\partial \mathbf{C}}{\partial c_j} \right], \quad (5.13)$$

\hat{c}_i is a good approximation to the maximum likelihood estimates of c_i if $C_i^{vI} \ll \sqrt{C_i^{vv} C_i^{II}}$. If the fiducial power spectra and noise used to compute $\mathbf{C}_{\text{diag}}^{-1}$ correctly describe the data then covariance matrix of \hat{c}_i is inverse of the response matrix (in this case the response matrix \mathbf{F} is the Fisher matrix). The matrix \mathbf{C}_{diag} is known as a "prior" in quadratic estimation theory (not to be confused with Bayesian priors). Equation (7) is unbiased regardless of the choice of prior (though it is no longer a minimum variance estimator for a bad choice of prior). Details about the implementation of this algorithm can be found in Padmanabhan et al. 2005 and Hirata et al. 2008.

Errors

We estimate the errors on the power spectra by splitting each region into eight jackknives. The error-bars are computed by using the standard deviation of the power-spectra computed on each independent jackknife using,

$$\sigma_{P(k)}^2 = (N - 1) \sum_{i=1}^N (P_i(k) - \tilde{P}(k))^2 / N. \quad (5.14)$$

One of the key assumptions while using jackknife errors is that the correlation length is smaller than the length scale associated with one jackknife region. The angular scales at which we estimate the cross-correlations are in the multipole range $\ell \sim 10 - 550$ corresponding to angular scales $\leq 18^\circ$ while the typical angular scale of the jackknife regions in our analysis is $\sim 45^\circ$. Hence this assumption holds for our error estimates.

A second, more subtle, assumption in computing our error bars is that each jackknife region is an independent realization of the foreground sky. However, we obviously have access to one sky, and the foregrounds in different parts of the sky can have (and do have) different morphologies. Hence, the jackknife error bars should be interpreted as the uncertainty on our measurements given a very morphologically inhomogeneous sample, instead of an uncertainty derived from “independent” measurements of the same sky.

Priors

To compute the priors \mathbf{C}_{diag} required for the cross-correlation power spectrum analysis, we need an estimate the auto-correlation of each LWA map and the ISM tracer maps. We do this by using the anafast routine included in the HEALPix package (Górski et al. 2005). Anafast performs a harmonic analysis of the HEALPix maps up to maximum spherical harmonic order ℓ_{max} by computing integrals on the whole sphere. Anafast is not optimally suited for measuring power-spectra on cut maps (unlike the algorithm outlined above). However, it provides a rough estimate of the auto-spectra in the maps that can then be used in our analysis. While setting the priors we set $C_l \gg C_{l \geq 2}$ for $l = 0, 1$ to reject the monopole and dipole modes from the cross-correlation analysis.

m-Mode suppression

The construction of LWA maps using *m*-mode analysis leads to spurious power at low-*m*'s, seen as horizontal stripes in the raw maps. For our analysis, we artificially

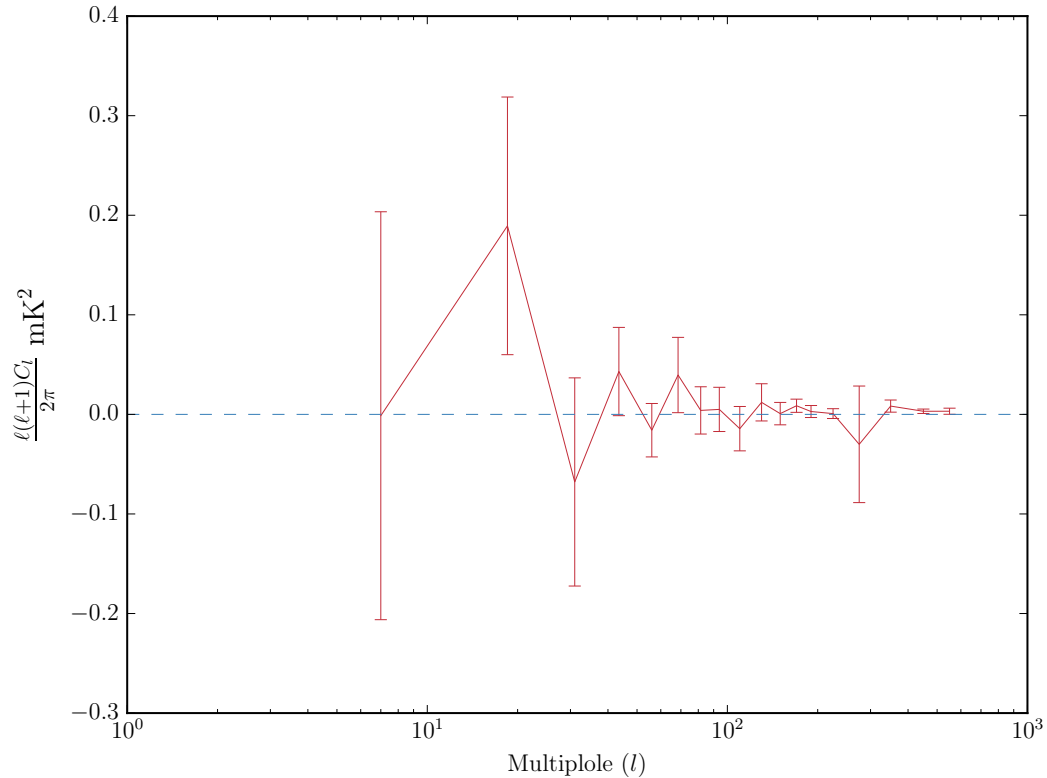


Figure 5.4: Cross-spectra between LWA map and Dust map with power injected in the $l = 250 - 300$ band

inject power that is comparable to $C_l \gg C_{l \geq 2}$ for $m = 0, 1$ to reject the low- m modes from the cross-correlation analysis.

Simulations and Tests

To test the powspec routine, we injected power in the $l = 250 - 300$ band in the dust map and estimated the cross-spectra with the LWA1 map as well as the auto-power spectrum of the dust map with the injected power. The recovered Dust-LWA1 cross-spectra is shown in Figure 5.4 while Figure 5.5 shows the auto-power spectrum of the dust map. The powspec routine recovers the correct power in the relevant band.

5.7 Results

Figs. 5.6, 5.7 and 5.8 plot the cross-correlations between the LWA and the Dust, $\text{H}\alpha$, and HI maps respectively, for the Northern Sky cut. We report on the northern hemisphere here since this is an interesting window for 21cm observations and

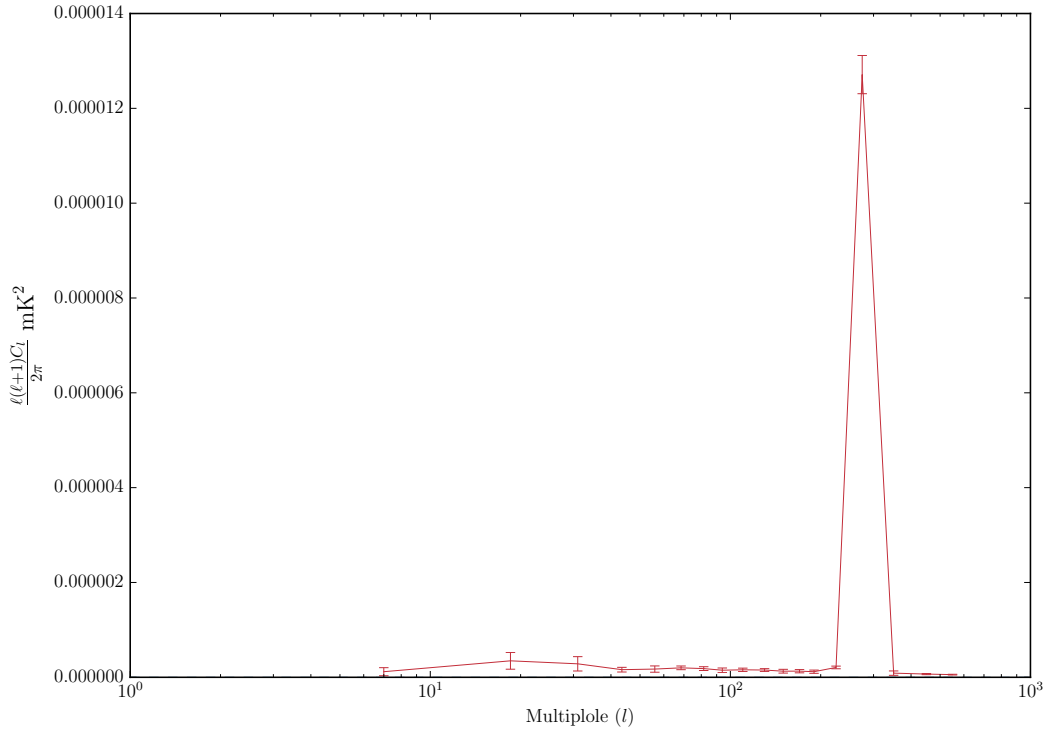


Figure 5.5: Recovered auto-power spectrum of the dust map with power injected in the $l = 250 - 300$ band

Table 5.1: Summary of LWA maps used for cross-correlations

Map	ν / MHz	$\Delta\nu$ / MHz
LWA1	41.760	0.024
LWA2	46.992	0.024
LWA3	52.224	0.024
LWA4	57.456	0.024
LWA5	62.688	0.024
LWA6	67.920	0.024

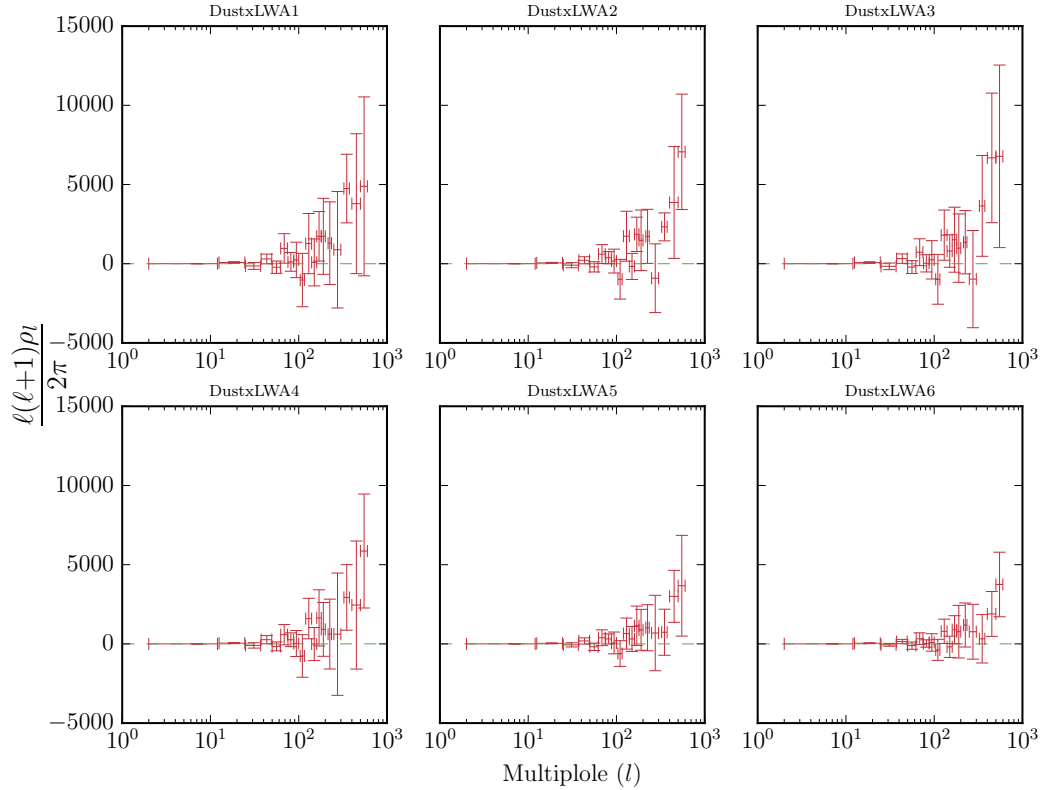


Figure 5.6: Dust map correlations with the six LWA maps for the northern sky-cut. The correlations are normalized with the auto-spectra as described in the text

because the LWA blind-spot, and galactic contamination allow for only a small window in the southern hemisphere.

We report the cross-correlations normalized with the corresponding auto-spectra such that,

$$\rho_\ell = \frac{C_\ell^{X \times Y}}{\sqrt{C_\ell^{X \times X} C_\ell^{Y \times Y}}} \quad (5.15)$$

such that ρ_ℓ is dimensionless. The errors reported are the jackknife errors on the cross-correlations described in Sec. 5.6.

From Fig. 5.6 we see that the cross-correlations of the dust map with low-frequency LWA maps is consistent with zero at the largest scales. We calculate the t -statistic for each ℓ bin under a null hypothesis that there is zero cross-correlation in a given ℓ bin, with 7 d.o.f. (since there are 8 jackknife regions). Table 5.2 reports the t -statistic for each ℓ bin (first row for a given ℓ band) and the corresponding p -value

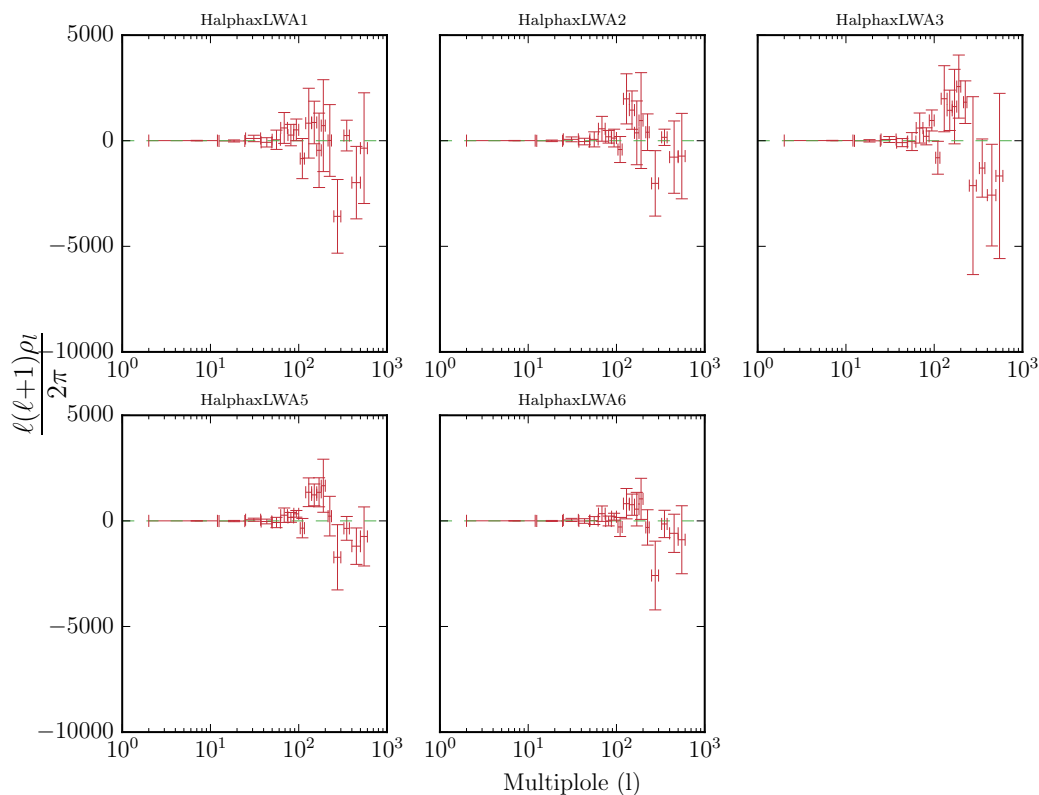


Figure 5.7: $H\alpha$ map correlations with the five LWA maps for the northern sky-cut. The correlations are normalized with the auto-spectra as described in the text

(second row for a given ℓ band). As seen from the table, we cannot rule out the null-hypothesis of zero cross-correlation at the $p < 0.001$ level.

We plot the cross-correlations of the $H\alpha$ map with low-frequency LWA maps in Fig. 5.7 and the results of a t-test under the null-hypothesis of zero cross-correlation are reported in Table 5.3. As seen from the table, we cannot reject the null-hypothesis of zero cross-correlation at the $p < 0.001$ level. The only exception is the cross-correlation of the LWA5 map with the $H\alpha$ map in the $\ell = 140 - 160$ band. However, we believe this is likely related to systematics in the LWA5 map since the maps in other frequency bands are consistent with zero cross-correlation.

Finally, Fig. 5.8 shows results of the cross-correlation of the HI map with low-frequency LWA maps and Table 5.4 reports the results of a t-test under the null-hypothesis of zero cross-correlation. As seen from the table, we cannot rule out the null-hypothesis of zero cross-correlation at the $p < 0.001$ level.

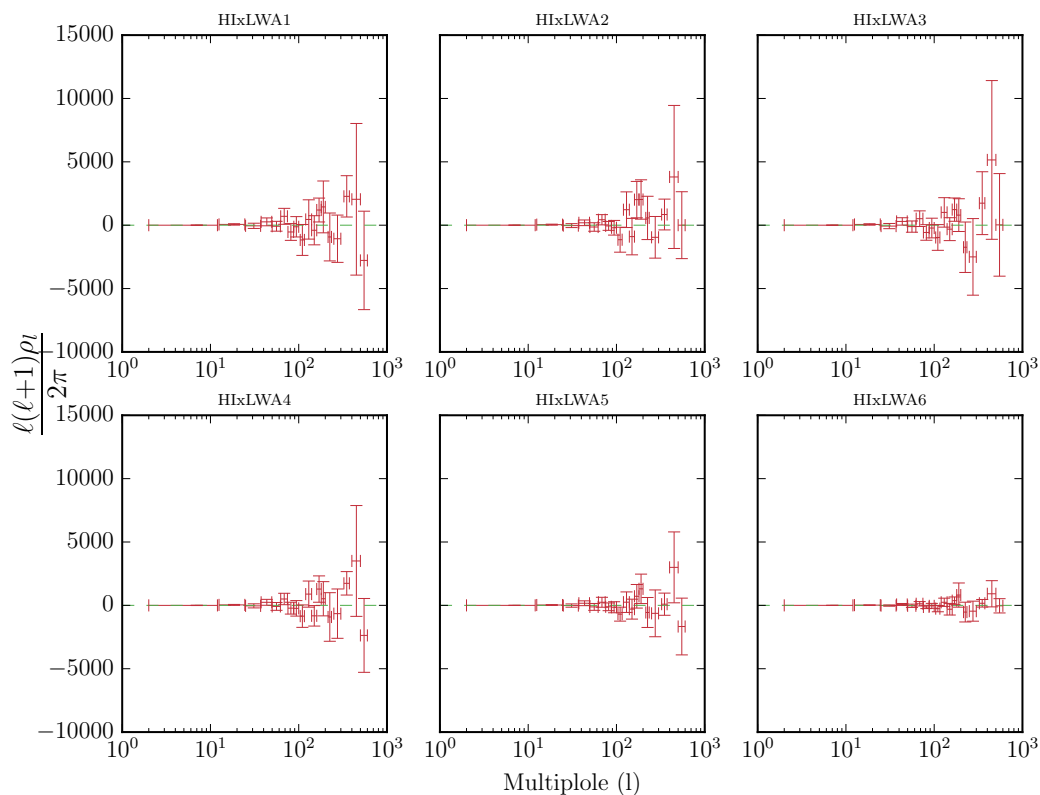


Figure 5.8: HI map correlations with the five LWA maps for the northern sky-cut. The correlations are normalized with the auto-spectra as described in the text

5.8 Implications for 21cm Foregrounds

In this section we discuss the implications of our cross-correlations on the emissions from different phases of the ISM at low-frequencies.

Dust

Dust traces density in the ISM and dust maps used in our analysis trace the thermal emission from dust at high frequencies. The cross-correlation between low-frequency LWA maps and the dust maps is sensitive to low-frequency emission from dust or any gas phase of the ISM that is traced by the (high-frequency) dust maps. There are no known mechanisms for dust emission at low-frequencies. The ionized gas phase of the ISM traced by the dust distribution could potentially be a source of free-free radiation and radio recombination lines. In any case, given the history of surprises in low-frequency foregrounds from the ISM, it is essential to check if there is any anomalous emission at low-frequencies.

If there is an unknown radiative mechanism for dust at low-frequencies, that occurs in high density regions, it will be reflected in the cross-correlation and we can put limits on the emissivity of the emission process. We can write,

$$T_{\text{low}}(\nu) = T_{\text{sync}}(\nu) + T_{\text{X,low}}(\nu) \quad (5.16)$$

Assuming that the synchrotron emission is not correlated with dust, the cross-correlation between LWA and high frequency dust maps can be used to put constraints on the emissivity of dust at low-frequencies (denoted by X).

Finkbeiner 2004 reports the emissivity per dust in terms of the optical depth at $100\mu\text{m}$, $\tau_{100\mu}$ and we use those units in our analysis to enable comparison to his results. Theorists typically quote emissivities in units of per Hydrogen atom ($\text{Jy cm}^2 \text{sr}^{-1}$ per H atom). However, the hydrogen column density is not well measured, and measurements using the gas-to-dust ratio can vary across regions. To avoid this, Finkbeiner 2004 reports dust emissivities in terms of optical depth at $100\mu\text{m}$ defined with respect to a blackbody at a reference temperature $T = 18.175\text{K}$. In these units the typical dust emissivities in the cold neutral, warm neutral, and warm ionized phase of the ISM is measured to be $\sim 10 \text{ MJysr}^{-1}$.

To put constraints on low-frequency emissivity, we note that,

$$j_\nu \propto T\nu^2 \quad (5.17)$$

where ν is the frequency associated with a given map and T is the antenna temperature in the Rayleigh-Jeans regime. We can thus write

$$C_\ell^{\text{LWA}\times\text{dust}} = \frac{j_\nu^{\text{X}}}{j_\nu^{\text{dust}}} \left(\frac{\nu_{\text{high}}}{\nu_{\text{low}}} \right)^2 C_\ell^{\text{dust}\times\text{dust}} \quad (5.18)$$

Choosing $\nu_{\text{low}} = 94\text{GHz}$ corresponding to the dust map we have,

$$j_{\nu=94\text{GHz}} = \tau_{94\text{GHz}} B(18\text{K}, 94\text{GHz}) \quad (5.19)$$

where $\tau_{94\text{GHz}}$ is the optical depth at 94GHz and B is the Planck function. Assuming $\tau \propto \nu^{1.7}$ (Finkbeiner 2004), we have,

$$\tau_{94\text{GHz}} = \tau_{100\mu\text{m}} \left(\frac{94 \text{ GHz}}{3000 \text{ GHz}} \right)^{1.7} \quad (5.20)$$

This allows us to write the emissivity of dust at low-frequencies in units of $\tau_{100\mu\text{m}}$. Using our measurements of $C_\ell^{\text{LWA}\times\text{dust}}$, $C_\ell^{\text{dust}\times\text{dust}}$ at $\nu = 94\text{GHz}$, and the measurements of j_ν in units of $\tau_{100\mu}$ (from Fig. 3 in Finkbeiner 2004), we plot the upper

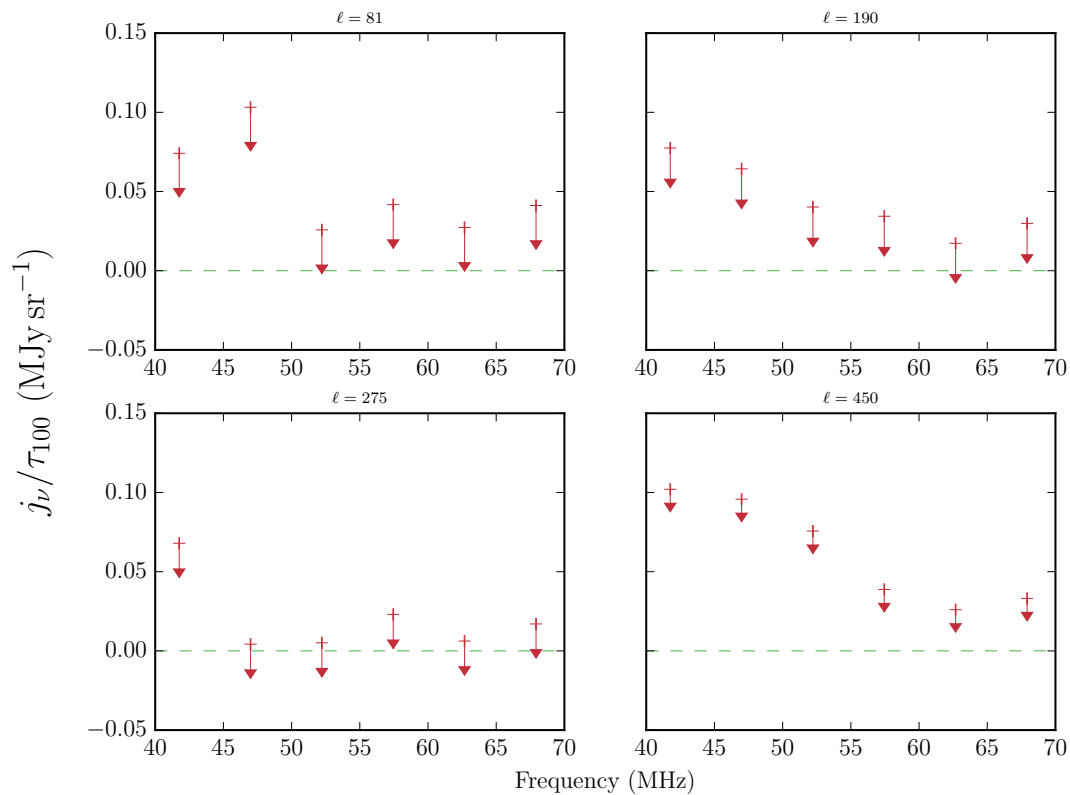


Figure 5.9: Upper limits on the dust emissivity at low-frequencies in terms of $\tau_{100\mu m}$, the optical depth at $100\mu m$.

limits on the emissivity of a potential X component in dust emission in Fig. 5.9 using LWA maps in four different frequency bands.

Note that extrapolating the free-free emissivity from high-frequencies (Fig. 2 in Finkbeiner 2004) leads to an emissivity per $\tau_{100\mu}$ of $\sim 1 \text{ MJy sr}^{-1}$ at low-frequencies (the extrapolated contribution due to thermal and spinning dust emission is expected to be negligible in comparison). The free-free emissivity depends on estimates of the free-free-to-dust ratio that can vary significantly between different regions of the sky. Hence, our estimated upper limits of $\sim 0.11 \text{ MJy sr}^{-1}$ for dust emissivity at low-frequencies as reported in Fig. 5.9, are reasonably consistent with extrapolated values from high-frequencies.

H α emission

The low-frequency temperature at low-frequencies observed by LWA can be modeled as,

$$T_{\text{low}}(\nu) = T_{\text{sync}}(\nu) + T_{ff}(\nu) - T_{\text{sync}}(\nu)\tau_{ff} \quad (5.21)$$

where $T_{\text{sync}}(\nu)$ is the synchrotron temperature at low-frequencies that is likely to dominate the LWA maps, $T_{ff}(\nu)$ is due to free-free emission, and τ_{ff} is the H α optical depth.

The free-free brightness temperature $T_{ff}(\nu)$ is a function of the electron temperature T_e ,

$$T_{ff}(\nu) = T_e\tau_{ff}(\nu) \quad (5.22)$$

and the free-free optical depth is given by,

$$\tau_{ff}(\nu) = 2.4 \times 10^{-4} \left(\frac{T_e}{10^4 \text{K}} \right)^{-0.45} \left(\frac{\nu}{50 \text{MHz}} \right)^{-2.1} \left(\frac{I_{H\alpha}}{0.5 \text{R}} \right) \quad (5.23)$$

Thus, if we assume the synchrotron temperature T_{sync} , in appropriate units, the cross-spectra of the LWA maps and the H α can be used to put constraints on the electron temperature T_e as a function of scale,

$$C_l^{\text{LWA} \times \text{H}\alpha} = 2.4 \times 10^{-4} (T_e - T_{\text{sync}}) \left(\frac{T_e}{10^4 \text{K}} \right)^{-0.45} \left(\frac{\nu}{50 \text{MHz}} \right)^{-2.1} C_l^{\text{H}\alpha \times \text{H}\alpha} \quad (5.24)$$

The ionized ISM is expected to have structures on all scales and the limits on the electron temperature as a function of angular scale ℓ are thus a proxy for structures in the electron density distribution of the ISM (with low- ℓ s corresponding to larger structures and vice-versa).

The synchrotron temperature of the sky at low-frequencies has been measured and is typically $T_{\text{sync}} \sim 800 \text{K}$ Rogers & Bowman 2008. From the measured $C_l^{\text{H}\alpha \times \text{H}\alpha}$ and the estimated cross-spectra we plot the upper limits on T_e as a function of scale, for a fiducial value of the synchrotron temperature in Fig. 5.10. Note that we get an upper limit of the order of 10^6K at most scales. The electron temperature is highest in HII regions (around 10^4K) and in the cold, diffuse ISM it is expected to be around $\sim 10^3 \text{K}$, which is consistent with our upper limits.

5.9 Conclusion

The primary goal of this chapter was to present a cross-correlation analysis between low-frequency maps produced by the OVRO LWA in the 20 – 80 MHz regime and

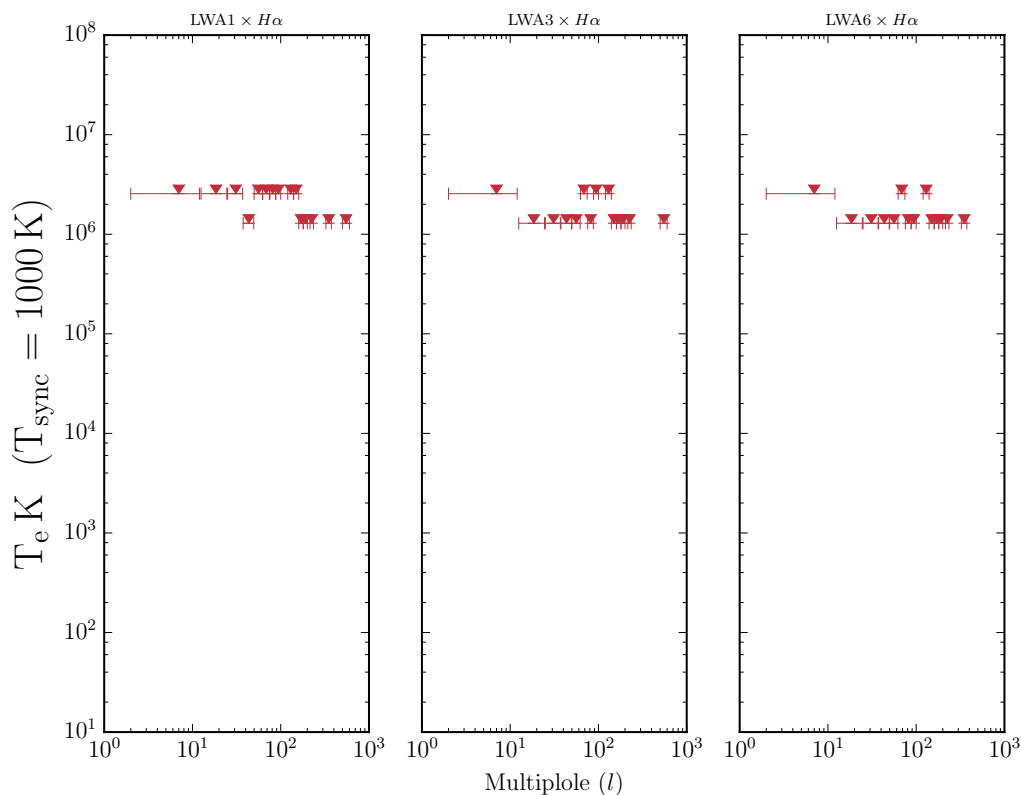


Figure 5.10: Upper limits on the electron temperature as a function of scale from cross-correlation of LWA maps with $H\alpha$ template, for a synchrotron temperature $T_{sync} = 1000\text{K}$

other known tracers of the ISM: dust, $H\alpha$, and HI. We described a formalism that can be used to determine optimal, unbiased error-bars on the cross-correlations. The primary results of this chapter are in Figures. 5.6, 5.7, & 5.8.

We also discussed the implications of our cross-correlation analysis on the determination of the electron temperature as a function of scale as well as the dust emissivity at low-frequencies. The cross-correlation of low-frequency maps with $H\alpha$ maps gives an upper bound of 10^6 K at the scales probed ($\ell \sim 10 - 600$). This is about 10^3 times higher than the expected electron temperature in the ISM.

The cross-correlation of the low-frequency maps with dust maps provides interesting new upper bounds on dust emissivity at low-frequencies. We put an upper bound on the dust emissivity per $\tau_{100\mu m}$ to be $j_\nu/\tau_{100\mu m} \sim 0.01\text{MJy sr}^{-1}$ at low-frequencies. This is an order of magnitude smaller than the extrapolated free-free emission from high frequencies; however, Finkbeiner 2004 used different regions of the sky to

obtain these constraints and the free-free-to-dust ratio can vary greatly between sky regions.

Accurate characterization of low-frequency foregrounds is critical if we intend to remove them and extract the cosmological 21cm signal. However, there are few direct constraints on foregrounds in the 10-100 MHz regime; most models rely on extrapolation of the Global Sky Model which hinges on high-frequency observations. In the event that there is an unknown, frequency dependent foreground at low-frequencies which is correlated with known tracers of the ISM, cross-correlation studies like the one reported in this chapter can potentially detect it.

In this chapter we embarked on a ‘fishing expedition’ for unknown low-frequency foregrounds. In the past, such efforts have been not only been instrumental in identifying new foregrounds for cosmology, but also added richly to our understanding of the ISM. As better low-frequency maps become available, with better controlled systematics and larger integration times, the cross-correlation methodology presented in this chapter can be used to search for anomalous emission in other regions of the sky that are of interest to 21 cm experiments (especially windows in the southern hemisphere). It would be particularly interesting to put upper bounds on dust emissivity in different regions of the sky, using cross-correlation results since (as discussed earlier), the free-free-to-dust ratio can differ significantly across regions. Finally, better low-frequency maps will provide an observational anchor at low-frequencies for the Global Sky Model that will be critical for 21 cm experiments.

The results in this chapter have been derived using the HEALPIX package developed by (Górski et al. 2005). We acknowledge the use of the Legacy Archive for Microwave Background Data Analysis (LAMBDA). Support for LAMBDA is provided by the NASA Office of Space Science.

5.10 Appendix A: Statistical Tests

Table 5.2: Summary statistics for t -tests on the LWA×Dust cross-correlation to check for zero correlation. The t -statistic is calculated for each ℓ bin under a null hypothesis that there is zero cross-correlation in the given ℓ bin, with 7 d.o.f. (since there are 8 jackknife regions). First row for a given ℓ band reports the t -statistic and the corresponding p -value is given in the second row for a given ℓ band.

ℓ band	LWA1×Dust	LWA2×Dust	LWA3×Dust	LWA4×Dust	LWA5×Dust	LWA6×Dust
2-12	-0.003 (0.997)	0.206 (0.843)	0.014 (0.989)	-1.068 (0.321)	-0.717 (0.497)	0.095 (0.927)
12-25	4.160 (0.004)	4.392 (0.003)	3.928 (0.006)	3.732 (0.007)	3.121 (0.017)	3.968 (0.005)
25-37	-1.853 (0.106)	-1.594 (0.155)	-2.230 (0.061)	-1.600 (0.154)	-1.321 (0.228)	-1.892 (0.100)
37-50	2.766 (0.028)	2.756 (0.028)	3.065 (0.018)	2.895 (0.023)	2.686 (0.031)	3.024 (0.019)
50-62	-1.590 (0.156)	-1.737 (0.126)	-1.469 (0.185)	-1.607 (0.152)	-2.233 (0.061)	-1.357 (0.217)
62-75	2.933 (0.022)	2.874 (0.024)	2.424 (0.046)	2.559 (0.038)	2.201 (0.064)	2.476 (0.042)
75-88	0.554 (0.597)	2.803 (0.026)	0.124 (0.905)	1.694 (0.134)	2.799 (0.027)	0.298 (0.775)
88-100	0.606 (0.563)	0.629 (0.549)	0.573 (0.584)	0.084 (0.935)	0.247 (0.812)	0.465 (0.656)
100-120	-1.733 (0.127)	-2.205 (0.063)	-1.769 (0.120)	-1.605 (0.153)	-2.126 (0.071)	-1.609 (0.152)
120-140	1.892 (0.100)	3.116 (0.017)	3.219 (0.015)	3.534 (0.010)	1.874 (0.103)	2.915 (0.023)
140-160	0.156 (0.881)	-0.594 (0.571)	2.209 (0.063)	-0.027 (0.979)	1.116 (0.301)	-0.786 (0.458)
160-180	3.133 (0.017)	4.840 (0.002)	2.090 (0.075)	2.623 (0.034)	2.606 (0.035)	2.848 (0.025)
180-200	2.037 (0.081)	2.185 (0.065)	1.292 (0.238)	1.524 (0.171)	1.945 (0.093)	1.311 (0.231)
200-250	1.403 (0.203)	2.860 (0.024)	1.921 (0.096)	0.795 (0.452)	1.983 (0.088)	2.425 (0.046)
250-300	0.679 (0.519)	-1.194 (0.271)	-0.896 (0.400)	0.448 (0.668)	0.814 (0.442)	1.252 (0.251)
300-400	6.197 (0.000)	7.453 (0.000)	3.244 (0.014)	4.009 (0.005)	1.428 (0.196)	0.593 (0.572)
400-500	2.427 (0.046)	3.097 (0.017)	4.617 (0.002)	1.716 (0.130)	5.172 (0.001)	3.779 (0.007)
500-600	2.447 (0.044)	5.485 (0.001)	3.328 (0.013)	4.609 (0.002)	3.266 (0.014)	5.203 (0.001)

Table 5.3: Summary statistics for t-tests on the LWA \times H α cross-correlation to check for zero correlation. The t -statistic is calculated for each ℓ bin under a null hypothesis that there is zero cross-correlation in the given ℓ bin, with 7 d.o.f. (since there are 8 jackknife regions). First row for a given ℓ band reports the t -statistic and the corresponding p-value is given in the second row for a given ℓ band.

ℓ band	LWA1 \times H α	LWA2 \times H α	LWA3 \times H α	LWA5 \times H α	LWA6 \times H α
2-12	1.236 (0.256)	1.565 (0.162)	2.133 (0.070)	1.599 (0.154)	2.450 (0.044)
12-25	-0.645 (0.540)	-0.418 (0.688)	-0.234 (0.821)	-0.766 (0.469)	-0.351 (0.736)
25-37	1.992 (0.087)	1.612 (0.151)	1.150 (0.288)	2.107 (0.073)	1.772 (0.120)
37-50	-0.986 (0.357)	-0.711 (0.500)	-1.317 (0.229)	-0.712 (0.499)	-0.132 (0.899)
50-62	0.280 (0.788)	0.507 (0.628)	-0.270 (0.795)	-0.885 (0.406)	0.247 (0.812)
62-75	2.338 (0.052)	2.717 (0.030)	2.387 (0.048)	2.227 (0.061)	2.650 (0.033)
75-88	1.491 (0.180)	1.770 (0.120)	1.461 (0.188)	2.022 (0.083)	-0.058 (0.955)
88-100	2.828 (0.025)	0.847 (0.425)	5.452 (0.001)	5.955 (0.001)	3.443 (0.011)
100-120	-2.518 (0.040)	-1.912 (0.097)	-2.930 (0.022)	-2.120 (0.072)	-1.803 (0.114)
120-140	1.422 (0.198)	4.726 (0.002)	3.594 (0.009)	5.644 (0.001)	3.211 (0.015)
140-160	2.424 (0.046)	4.515 (0.003)	4.262 (0.004)	6.750 (0.000)	4.319 (0.003)
160-180	-0.730 (0.489)	0.699 (0.507)	2.591 (0.036)	5.573 (0.001)	1.976 (0.089)
180-200	0.928 (0.384)	1.189 (0.273)	4.855 (0.002)	3.748 (0.007)	3.031 (0.019)
200-250	0.020 (0.985)	1.315 (0.230)	5.115 (0.001)	0.679 (0.519)	-1.046 (0.331)
250-300	-5.805 (0.001)	-3.687 (0.008)	-1.428 (0.196)	-3.157 (0.016)	-4.495 (0.003)
300-400	0.950 (0.374)	1.182 (0.276)	-2.658 (0.033)	-1.779 (0.118)	-0.633 (0.547)
400-500	-3.271 (0.014)	-1.283 (0.240)	-3.027 (0.019)	-3.927 (0.006)	-1.840 (0.108)
500-600	-0.380 (0.715)	-1.018 (0.343)	-1.207 (0.267)	-1.490 (0.180)	-1.569 (0.161)

Table 5.4: Summary statistics for t-tests on the LWA×HI cross-correlation to check for zero correlation. The t -statistic is calculated for each ℓ bin under a null hypothesis that there is zero cross-correlation in the given ℓ bin, with 7 d.o.f. (since there are 8 jackknife regions). First row for a given ℓ band reports the t-statistic and the corresponding p-value is given in the second row for a given ℓ band.

ℓ band	LWA1×HI	LWA2×HI	LWA3 ×HI	LWA4×HI	LWA5×HI	LWA6×HI
2-12	0.014 (0.989)	0.203 (0.845)	0.023 (0.982)	-0.492 (0.638)	-0.161 (0.876)	0.308 (0.767)
12-25	3.111 (0.017)	3.170 (0.016)	2.961 (0.021)	2.905 (0.023)	2.420 (0.046)	3.457 (0.011)
25-37	-0.687 (0.514)	-0.594 (0.571)	-0.963 (0.368)	-0.696 (0.509)	-0.346 (0.740)	-0.848 (0.424)
37-50	2.399 (0.048)	2.407 (0.047)	2.886 (0.023)	2.916 (0.022)	2.482 (0.042)	2.625 (0.034)
50-62	-0.610 (0.561)	-1.203 (0.268)	-0.703 (0.505)	-0.773 (0.465)	-1.274 (0.243)	-0.727 (0.491)
62-75	3.151 (0.016)	3.009 (0.020)	2.354 (0.051)	3.153 (0.016)	1.756 (0.122)	2.055 (0.079)
75-88	-2.279 (0.057)	-0.455 (0.663)	-2.635 (0.034)	-1.334 (0.224)	-1.055 (0.327)	-2.724 (0.030)
88-100	-0.441 (0.672)	-0.987 (0.357)	-0.817 (0.441)	-1.087 (0.313)	-0.969 (0.365)	-0.568 (0.588)
100-120	-2.697 (0.031)	-3.291 (0.013)	-2.698 (0.031)	-2.721 (0.030)	-3.566 (0.009)	-2.947 (0.021)
120-140	0.827 (0.436)	2.458 (0.044)	2.457 (0.044)	2.439 (0.045)	0.876 (0.410)	2.116 (0.072)
140-160	-0.985 (0.358)	-1.772 (0.120)	-0.977 (0.361)	-2.888 (0.023)	-1.072 (0.319)	-1.883 (0.102)
160-180	3.595 (0.009)	3.974 (0.005)	3.779 (0.007)	3.499 (0.010)	2.176 (0.066)	3.590 (0.009)
180-200	1.996 (0.086)	3.692 (0.008)	1.740 (0.125)	1.093 (0.311)	3.175 (0.016)	2.409 (0.047)
200-250	-1.389 (0.207)	0.950 (0.374)	-2.472 (0.043)	-1.352 (0.218)	-1.344 (0.221)	-1.923 (0.096)
250-300	-1.620 (0.149)	-1.646 (0.144)	-2.339 (0.052)	-0.950 (0.374)	-0.964 (0.367)	-1.641 (0.145)
300-400	3.950 (0.006)	1.961 (0.091)	1.982 (0.088)	5.315 (0.001)	0.297 (0.775)	1.559 (0.163)
400-500	0.966 (0.366)	1.907 (0.098)	2.326 (0.053)	2.266 (0.058)	3.032 (0.019)	2.500 (0.041)
500-600	-2.024 (0.083)	0.002 (0.999)	0.018 (0.986)	-2.301 (0.055)	-2.108 (0.073)	-0.177 (0.865)

References

- Ali, Z. S., Parsons, A. R., Zheng, H., et al., 2015, *ApJ*, 809, 61, 61
- Barkana, R., & Loeb, A., 2005, *ApJ*, 626, 1
- Bernardi, G., Mitchell, D. A., Ord, S. M., et al., 2011, *MNRAS*, 413, 411
- de Oliveira-Costa, A., Kogut, A., Devlin, M. J., et al., 1997, *ApJL*, 482, L17
- de Oliveira-Costa, A., Tegmark, M., Guti rrez, C. M., et al., 1999, *ApJL*, 527, L9
- de Oliveira-Costa, A., Tegmark, M., Finkbeiner, D. P., et al., 2002, *ApJ*, 567, 363
- de Oliveira-Costa, A., Tegmark, M., Davies, R. D., et al., 2004, *ApJL*, 606, L89
- de Oliveira-Costa, A., Tegmark, M., Gaensler, B. M., et al., 2008, *MNRAS*, 388, 247
- Di Matteo, T., Perna, R., Abel, T., & Rees, M. J., 2002, *ApJ*, 564, 576
- Dickinson, C., Davies, R. D., & Davis, R. J., 2003, *MNRAS*, 341, 369
- Draine, B. T., & Lazarian, A., 1998, *ApJL*, 494, L19
- , 1999, *ApJ*, 512, 740
- Finkbeiner, D. P., 2003, *ApJS*, 146, 407
- , 2004, *ApJ*, 614, 186
- Finkbeiner, D. P., Davis, M., & Schlegel, D. J., 1999, *ApJ*, 524, 867
- Finkbeiner, D. P., Schlegel, D. J., Frank, C., & Heiles, C., 2002, *ApJ*, 566, 898
- Furlanetto, S. R., Sokasian, A., & Hernquist, L., 2004a, *MNRAS*, 347, 187
- Furlanetto, S. R., Zaldarriaga, M., & Hernquist, L., 2004b, *ApJ*, 613, 16
- Furlanetto, S. R., Oh, S. P., & Briggs, F. H., 2006, *PhR*, 433, 181
- G rski, K. M., Hivon, E., Banday, A. J., et al., 2005, *ApJ*, 622, 759
- Haffner, L. M., Reynolds, R. J., Tufte, S. L., et al., 2003, *ApJS*, 149, 405
- Haslam, C. G. T., Klein, U., Salter, C. J., et al., 1981, *A&A*, 100, 209
- Haslam, C. G. T., Salter, C. J., Stoffel, H., & Wilson, W. E., 1982, *A&AS*, 47, 1
- HI4PI Collaboration, Ben Bekhti, N., Fl er, L., et al., 2016, *A&A*, 594, A116, A116
- Hirata, C. M., Padmanabhan, N., Seljak, U., Schlegel, D., & Brinkmann, J., 2004, *PhRvD*, 70.10, 103501, 103501
- Hirata, C. M., Ho, S., Padmanabhan, N., Seljak, U., & Bahcall, N. A., 2008, *PhRvD*, 78.4, 043520, 043520
- Ho, S., Hirata, C., Padmanabhan, N., Seljak, U., & Bahcall, N., 2008, *PhRvD*, 78.4, 043519, 043519

- Hogan, C. J., & Rees, M. J., 1979, MNRAS, 188, 791
- Iliev, I. T., Shapiro, P. R., Ferrara, A., & Martel, H., 2002, ApJL, 572, L123
- Kocz, J., Greenhill, L. J., Barsdell, B. R., et al., 2015, Journal of Astronomical Instrumentation, 4, 1550003, 1550003
- Kogut, A., Banday, A. J., Bennett, C. L., et al., 1996, ApJ, 460, 1
- Landecker, T. L., & Wielebinski, R., 1970, Australian Journal of Physics Astrophysical Supplement, 16, 1
- Leitch, E. M., Readhead, A. C. S., Pearson, T. J., & Myers, S. T., 1997, ApJL, 486, L23
- Liu, A., & Tegmark, M., 2012, MNRAS, 419, 3491
- Liu, H., Mertsch, P., & Sarkar, S., 2014, ApJL, 789, L29, L29
- Loeb, A., & Zaldarriaga, M., 2004, Physical Review Letters, 92.21, 211301, 211301
- Madau, P., Meiksin, A., & Rees, M. J., 1997, ApJ, 475, 429
- Mao, Y., Tegmark, M., McQuinn, M., Zaldarriaga, M., & Zahn, O., 2008, PhRvD, 78.2, 023529, 023529
- McClure-Griffiths, N. M., Pisano, D. J., Calabretta, M. R., et al., 2009, ApJS, 181, 398
- McQuinn, M., Zahn, O., Zaldarriaga, M., Hernquist, L., & Furlanetto, S. R., 2006, ApJ, 653, 815
- Oh, S. P., & Mack, K. J., 2003, MNRAS, 346, 871
- Padmanabhan, N., Hirata, C. M., Seljak, U., et al., 2005, PhRvD, 72.4, 043525, 043525
- Planck Collaboration, Adam, R., Ade, P. A. R., et al., 2016, A&A, 586, A133, A133
- Rogers, A. E. E., & Bowman, J. D., 2008, AJ, 136, 641
- Santos, M. G., Cooray, A., & Knox, L., 2005, ApJ, 625, 575
- Schlegel, D. J., Finkbeiner, D. P., & Davis, M., 1998, ApJ, 500, 525
- Seljak, U., 1998, ApJ, 506, 64
- Shaw, J. R., Sigurdson, K., Pen, U.-L., Stebbins, A., & Sitwell, M., 2014, ApJ, 781, 57, 57
- Shaw, J. R., Sigurdson, K., Sitwell, M., Stebbins, A., & Pen, U.-L., 2015, PhRvD, 91.8, 083514, 083514
- Tashiro, H., Aghanim, N., Langer, M., et al., 2010, MNRAS, 402, 2617
- Tegmark, M., 1997, PhRvD, 55, 5895

- Tozzi, P., Madau, P., Meiksin, A., & Rees, M. J., 2000, *ApJ*, 528, 597
- Winkel, B., Kerp, J., Flöer, L., et al., 2016, *A&A*, 585, A41, A41
- Zaldarriaga, M., Furlanetto, S. R., & Hernquist, L., 2004, *ApJ*, 608, 622
- Zheng, H., Tegmark, M., Dillon, J. S., et al., 2017, *MNRAS*, 464, 3486